NUMERICAL SIMULATION OF TURBINE INTERNAL COOLING AND CONJUGATE HEAT TRANSFER PROBLEMS WITH RANS BASED TURBULENCE MODELS

A THESIS SUBMITTED TO
THE GRADUATE SCHOOL OF NATURAL AND APPLIED SCIENCES
OF
MIDDLE EAST TECHNICAL UNIVERSITY

BY

İLHAN GÖRGÜLÜ

IN PARTIAL FULFILLMENT OF THE REQUIREMENTS
FOR
THE DEGREE OF MASTER OF SCIENCE
IN
AEROSPACE ENGINEERING

SEPTEMBER 2012

Approval of the thesis:

NUMERICAL SIMULATION OF TURBINE INTERNAL COOLING AND CONJUGATE HEAT TRANSFER PROBLEMS WITH RANS BASED TURBULENCE MODELS

Submitted to **İLHAN GÖRGÜLÜ** in partial fulfillment of the requirements for the degree of **Master of Science in Aerospace Engineering, Middle East Technical University** by,

Prof. Dr. Canan ÖZGEN   _____
Dean, Graduate School of **Natural and Applied Sciences**

Prof. Dr. Ozan TEKİNALP   _____
Head of Department, **Aerospace Engineering**

Prof. Dr. İ. Sinan AKMANDOR   _____
Supervisor, **Aerospace Engineering Dept., METU**

Examining Committee Members

Prof. Dr. Cevdet ÇELENLİGİL   _____
Aerospace Engineering Dept., METU

Prof. Dr. İ. Sinan AKMANDOR   _____
Aerospace Engineering Dept., METU

Assoc. Prof. Dr. Sinan EYİ   _____
Aerospace Engineering Dept., METU

Assoc. Prof. Dr. Oğuz UZOL   _____
Aerospace Engineering Dept., METU

Dr. Barış GÜMÜŞEL   _____
Compressor Component Leader, TEI

Date: 14/09/2012

I hereby declare that all information in this document has been obtained and presented in accordance with academic rules and ethical conduct. I also declare that, as required by these rules and conduct, I have fully cited and referenced all material and results that are not original to this work.

Name, Last name : İlhan Görgülü

Signature :

ABSTRACT

NUMERICAL SIMULATION OF TURBINE INTERNAL COOLING AND CONJUGATE HEAT TRANSFER PROBLEMS WITH RANS-BASED TURBULANCE MODELS

Görgülü, İlhan

M.Sc., Department of Aerospace Engineering

Supervisor: Prof. Dr. İ Sinan Akmandor

September 2012, 120 Pages

The present study considers the numerical simulation of the different flow characteristics involved in the conjugate heat transfer analysis of an internally cooled gas turbine blade. Conjugate simulations require full coupling of convective heat transfer in fluid regions to the heat diffusion in solid regions. Therefore, accurate prediction of heat transfer quantities on both external and internal surfaces has the uppermost importance and highly connected with the performance of the employed turbulence models. The complex flow on both surfaces of the internally cooled turbine blades is caused from the boundary layer laminar-to-turbulence transition, shock wave interaction with boundary layer, high streamline curvature and sequential flow separation. In order to discover the performances of different turbulence models on these flow types, analyses have been conducted on five different experimental studies each concerned with different flow and heat transfer characteristics. Each experimental study has been examined with four different turbulence models available in the commercial software (ANSYS FLUENT13.0) to decide most suitable RANS-based turbulence

model. The Realizable k-ε model, Shear Stress Transport k-ω model, Reynolds Stress Model and V2-f model, which became increasingly popular during the last few years, have been used at the numerical simulations. According to conducted analyses, despite a few unreasonable predictions, in the majority of the numerical simulations, V2-f model outperforms other first-order turbulence models (Realizable k-ε and Shear Stress Transport k-ω) in terms of accuracy and Reynolds Stress Model in terms of convergence.

Keywords: Conjugate Heat Transfer, Turbine Internal Cooling, V2-f Turbulence Model, Reynolds Stress Model, RANS, Computational Fluid Dynamics

ÖZ

RANS TEMELLİ TÜRBÜLANS MODELLERİ KULLANARAK TÜRBİN İÇ SOĞUTMA VE KONJUGE ISI TRANSFERİ PROBLEMLERİNİN SAYISAL BENZEŞİMİ

Görgülü, İlhan

Yüksek Lisans, Havacılık ve Uzay Mühendisliği Bölümü

Tez Yöneticisi: Prof. Dr. İ. Sinan Akmandor

Eylül 2012, 120 Sayfa

Mevcut çalışma, iç soğutmalı bir gaz türbin palesinin konjuge ısı transferi analizinin içerdiği farklı akış tiplerinin sayısal benzeşimini kapsamaktadır. Konjuge benzeşmeler, akışkan alanlarlardaki konvektif ısı transferi ile katı alanlara nüfus eden ısının tam eşleşmesini gerektirmektedir. Bu nedenle, hem dış hem de iç yüzeylerdeki ısı transferi değerlerinin doğru tahmin edilmesi öncelikli öneme sahiptir ve büyük ölçüde kullanılan türbülans modelinin performansına bağlıdır. İç soğutmalı türbin palelerinin her iki yüzeyindeki karmaşık akışa, sınır tabakanın laminerden türbülanslı akışa geçişi, sınır tabaka ile şok dalgasının etkileşimi, yüksek akış çizgisi eğilimi ve birbirini izleyen akış ayrılması sebep olmaktadır. Farklı türbülans modellerinin bu akış tiplerindeki performansını bulmak amacıyla, her biri farklı akış ve ısı transferi özellikleriyle ilgili beş farklı deneysel çalışma üzerinde analizler yapılmıştır. En uygun RANS temelli türbülans modeline karar vermek için her deneysel çalışma ticari kodda (ANSYS FLUENT13.0) mevcut olan dört farklı türbülans modeli ile incelenmiştir. Sayısal benzeşimlerde Realizable k-ε modeli, Shear Stress Transport k-ω modeli, Reynolds Stress Model ve son bir kaç

yılda giderek popüler olan V2-f modeli kullanılmıştır. Yürütülen analizlere göre, bir kaç makul olmayan tahmine rağmen, sayısal benzeşimlerin genelinde V2-f modeli diğer birinci derece türbülans modellerine (Realizable k-ε ve Shear Stress Transport k-ω) doğrulukta ve Reynolds Stress Modeli'ne yakınsamada üstün gelmiştir.

Anahtar Kelimeler: Konjuge Isı Transferi, Türbin İç Soğutma, V2-f Türbülans Modeli, Reynols Stress Model, RANS, Hesaplamalı Akışkanlar Dinamiği

To my young padavan Berk-Görgülü ...

ACKNOWLEDGEMENTS

TABLE OF CONTENTS

LIST OF TABLES

LIST OF FIGURES

CHAPTER 1

INTRODUCTION

1.1   Gas Turbines

Gas turbines have a wide application area from commercial and military aircraft engines to naval propulsion and power generation. These entire aerial, marine or land based application areas are growing day by day with greater need of power output. Increasing power output demands made thermal efficiency one of the most important issues about the gas turbine engines due to environmental and economical concerns. Gas turbine engine applications, aircraft engines to industrial utilizations, can be idealized as a Brayton cycle. In an ideal Brayton cycle, under the assumptions of isentropic compression and expansion with no friction losses and constant Cp, main controlling factor of thermal efficiency is turbine inlet temperature. Through the decades engineers increased the turbine inlet temperatures of gas turbines to receive greater thermal efficiency as well as greater power output and interest in elevating the temperatures to higher values still remains. The turbine component of the gas turbine engines mainly deals with the highest temperature values of which are well beyond the allowable material limit. Although, more durable alloys have been developed and coating technologies have made important progress, material endurance and operational live under intense temperatures are still the limiting factor to increase turbine inlet temperatures. A plot of approximate turbine inlet temperatures of large aircraft engines throughout last half century is shown at Figure 1.1.
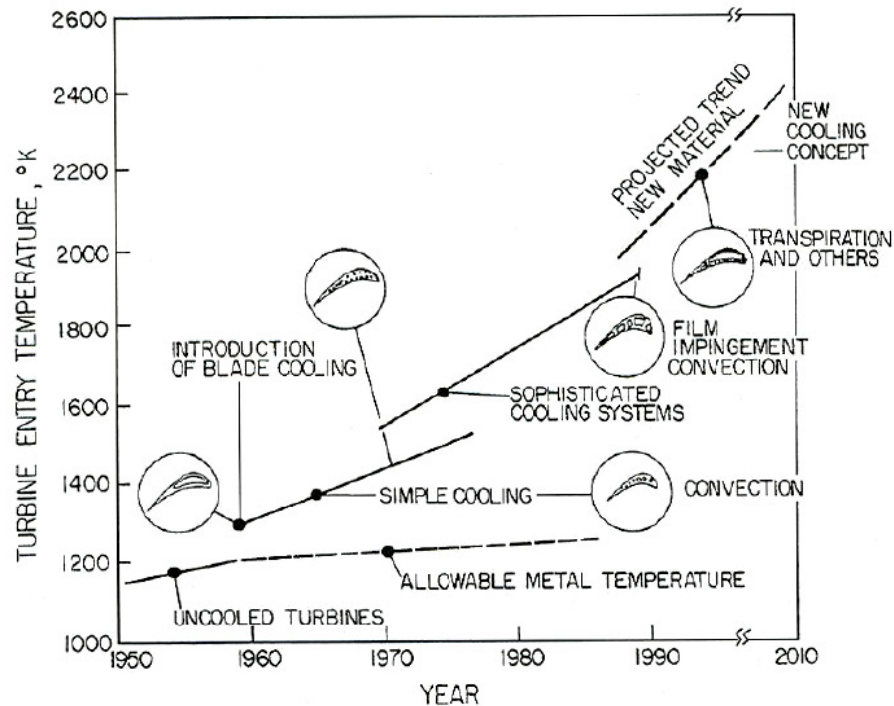
Figure 1.1. Improvements on turbine inlet temperature through time

As can be seen from Figure 1.1 the allowable material temperature line has no interest with the current needs of gas turbine engines. Figure 1.1 also reveals that turbine inlet temperatures of 2000 K are typical for current gas turbines. It is apparent that to cope with the thermal efficiency and power output requirements, using turbine cooling techniques is inevitable.

1.2 Turbine Cooling Strategies

The turbine blades are cooled by the air extracted from the compressor of the engine. The task is keeping maximum metal temperature below the values specified by material capabilities and besides avoid from high temperature variations within the turbine blade to maintain acceptable life and operational requirements with extracting the minimum cooling air possible. To achieve this task, special techniques are implemented to optimize turbine cooling. The cooling strategies are mainly divided into two groups as internal cooling and external cooling.

2

1.2.1   Internal Cooling

Various cooling arrangements are employed to enhance heat removal from the blade. These arrangements are chosen according to which zone of the turbine blade is being cooled. Figure 1.2 describes the most effective turbine internal cooling applications which are being used at modern turbine blades. There are three major internal cooling zones in a turbine blade. Regions near leading edge are cooled using impingement cooling, at central regions air is ducted through serpentine passages which are often ribbed and trailing edge region is equipped with an array of pin-fins.
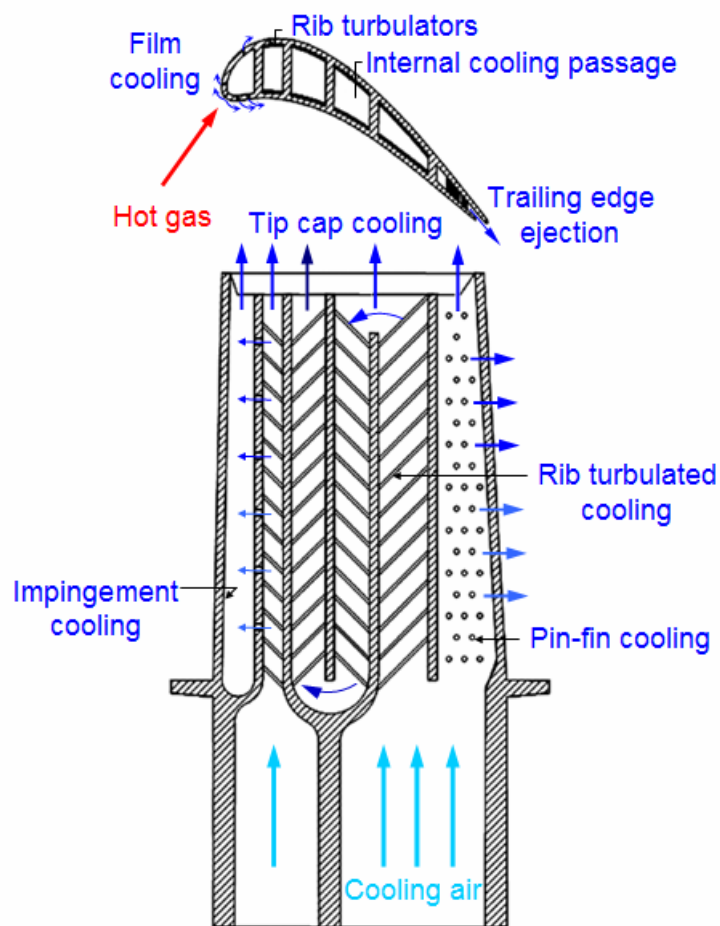
Figure 1.2.   Cooling concepts of a modern gas turbine engine

Among all internal turbine cooling techniques, jet impingement is the most effective at increasing heat transfer coefficient. In jet impingement method air jets, which are being created by forcing air through perforated plates, impinge on hot interior blade regions. Modern cooling configurations generally use jet impingement method at leading edge due to its structural constraints. Serpentine passages with ribs turbulators on the inner walls are used near the middle portion of the turbine blades. Repeated rib turbulators are cast into the serpentine passage to increase heat transfer coefficient. Close to trailing edge, turbine blade becomes thinner and pin-fins are preferred because of its structural advantages. They generally have staggered array and extend interior suction to pressure surfaces. Both rib turbulators and pin-fins have vast variation of shape, height, width, placement in the internal cooling channel and angle with the air flow. Each configuration has its own advantages and disadvantages in terms of heat transfer coefficient enhancement and created loses.

1.2.2   External (Film) Cooling

In cooling arrangements which solely use internal cooling applications, circulated air in the internal cooling passages is ejected from trailing edge ejection slots. However in external cooling, the idea is injecting coolant air inside the blade to the hot gas path by discrete holes other than trailing edge ejection slots and protecting blade from hot gasses by forming a film layer on the blade. Injected fluid introduces a secondary flow and protects both immediate region of injection and downstream of it so compared to internal cooling techniques which remove heat from inside surface, external cooling applications directly protects the blade surface.

External cooling configuration success depends on many parameters. The geometrical aspects of the hole like shape, length-to-diameter ratio and injected flow angle relative to the main flow are very important. Besides, location and distribution of the holes on the surface have also primary importance for blade protection from hot gases. The most common film cooling hole drilling locations are depicted at Figure 1.3.
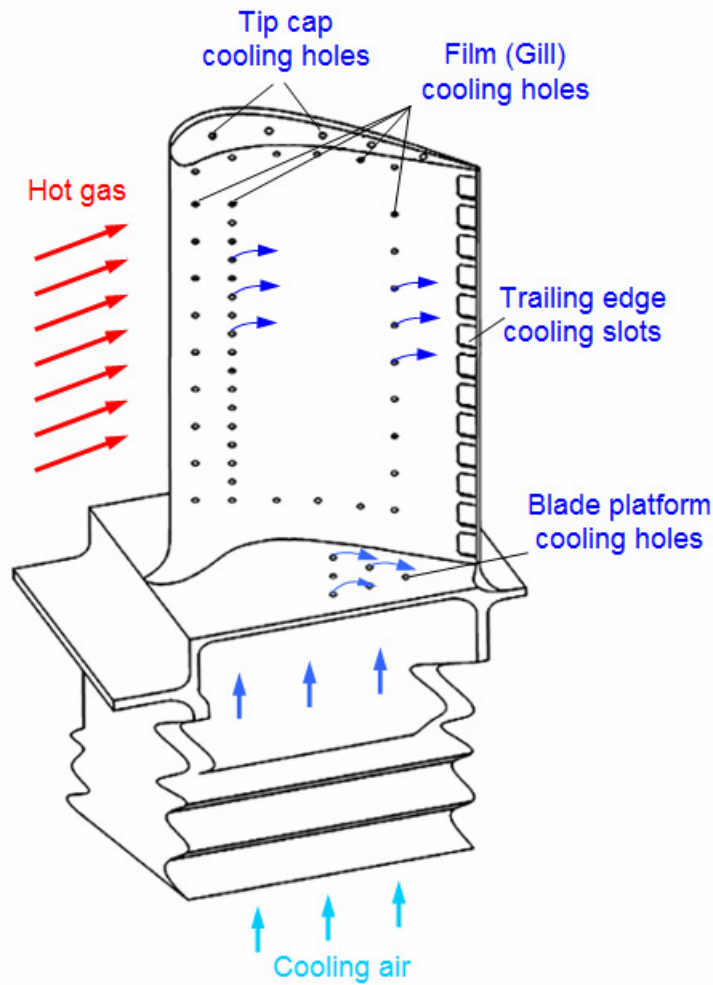
Figure 1.3. External (film) cooling hole locations

The holes responsible from leading edge and tip cap cooling are the most critical ones. The reason is that, first deals with the highest temperatures due to the stagnation of hot gases at the leading edge and second has a location where lacks durability and difficult to cool because of the tip leakage. Other common film cooling holes locations are blade platform cooling holes and gill holes which are also depicted at Figure 1.3.

Although, there are common locations for turbine cooling holes as presented at Figure 1.3, some quantities are evaluated to decide their exact locations. Most useful measures of quantifying effectiveness of external cooling configuration are coolant to mainstream temperature ratio (Tc/Tg) and pressure ratio (Pc/Pg). In general lower temperature ratio and higher pressure ratio are

favourable while the other parameter kept constant. However, a too high coolant to mainstream pressure ratio may cause jet penetration to mainstream and reduce the external cooling effectiveness. Therefore, amount of coolant used for internal and external cooling needs should be optimized under engine operating conditions.

1.3 Objectives and Limitations of the Study

The objectives of this study can be listed as follows:

- Presenting the capabilities of RANS based turbulence models in predicting the conjugate heat transfer analyses.

- Examining the performance of RANS based turbulence models in simulations of different flow features that are characteristics of modern cooling configurations employed at gas turbines.

- Developing a computational methodology to analyse advanced turbine cooling problems.

- Presenting a comprehensive definition of the theory, equations and basic versions of V2-f turbulence model with related realizability constraints and coefficients.

- Demonstrating the capabilities of V2-f turbulence model in predicting laminar to turbulence transition.

The limitations of this study can be listed as follows:

- External cooling applications are out of the scope of this study.

- The entire test cases have been simulated with the steady-state RANS based turbulence models so unsteady analyses are out of the scope of this study.

- None of the test cases contain rotation so Coriolis effects caused from rotation are not present.

- Buoyancy effects (natural convection) have been neglected at all simulations.

1.4   Literature Review

There have been large numbers of studies about the straight and multi-pass, stationary and rotating channels which are equipped with turbulence promoters and have different cross sections. These studies have examined the effects of different configurations of rib turbulators and pin-fins, geometry of the turn region and divider wall of multi-pass channels, aspect ratio of channels and rotation to the heat transfer distribution along the channels. The effects of different aspect ratios have been studied with square, rectangular and trapezoidal cross sections. The effects of different configurations of rib turbulators have been studied with different angles (45°, 60°, 90°, etc.), shapes (V-shape, W-shape, broken type, etc.), height-to-hydraulic diameter ratios and pitch-to-height ratios. The effects of different pin-fin distributions (inline, staggered, broken, etc.) have been studied with different height-to-hydraulic diameter ratios and diameter-to-height ratios. The effects of Coriolis force caused from rotation and buoyancy force caused from channel orientation also have been studied. In all these studies effects of different Reynolds numbers, density and rotation ratios have been presented by using experimental and numerical methods. Therefore, literature survey is discussed in two separate parts namely experimental studies and numerical studies.

Analyses of conjugate heat transfer problems with RANS methods is an important part of this study so available past investigations about this subject are also mentioned in this literature review under aforementioned parts.

It should also be noted that many of the studies that will be mentioned in this literature survey are widely clarified in the chapters of Han et al. [1] and article of Iacovides et al. [2].

1.4.1 Experimental Studies

Various investigators conducted experimental studies in the straight channel geometries to understand the effects of different internal cooling configurations summarised above. Periodic rib configuration in a straight channel is investigated by Tanda et al. [3], Casarsa [4] and H. Liu [5]. In addition to these studies Y.H. Liu [6] examined the effect of rotation to straight channels configured with ribs. The impingement cooling is widely studied by Schueren et al. [7], Wang et al. [8] and Gao [9]. Effectiveness of dimple geometries have been examined in stationary straight channels by Jordan et al. [10], Tran et al. [11] and Zhou [12]. In the case of smooth two-pass channels, there are studies conducted by Monson et al. [13], and Liou et al. [14]. In case of two-pass channels rotating at a certain radial velocity studies have been investigated by Iacovides et al. [15] and Liou et al. [16]. Chen et al. [17], Mochizuki et al. [18], Han et al. [19], Ekkad et al. [20] and Lee [21] investigated on two-pass channels roughened with rib turbulators. Effect of rotation on these type of cooling channel configurations is studied by Liou et al. [22,23], Agarwal [24], Huh [25], Fu [26] and Y.H. Liu [27]. Although there are countless experimental studies conducted on internal cooling configurations, studies including both internal and external flow characteristics with solid effect are not so diverse. Many studies suit to this description make use of film cooling methods so the documentation of sole effect of internal cooling is very limited. The experimental work of Hylton et al. [28] is known as one of the oldest and most comprehensive investigation dealing with the effects of internal cooling and for a long time it was the only study documenting the metal temperature values. Recently Dees [29] and Davidson et al. [30] conducted experimental studies to examine the effect of internal cooling on the blade surface and these studies provided an experimental benchmark for the validation of computational conjugate heat transfer codes.

Tanda et al. [3] conducted heat transfer experiments on a straight rectangular channel (aspect ratio equal to 5) roughened with straight and V-shape (45° and 60°) rib turbulators having rectangular and square cross sections. Heat transfer coefficient distributions are obtained at Reynolds number values of 8900 and 28500 using liquid crystal thermography. It has been concluded that at

high pitch-to-height ratios broken straight rib configuration has better performance yet at lover ratios V-shape rib turbulators are more advantageous. Casarsa [4] conducted PIV measurements on a square channel equipped with transverse rib turbulators. Aero-thermal comparison of the experimental data revealed that heat transfer distribution is strongly effected by the velocity fluctuations normal to the wall. H. Liu [5] investigated on channels having two different aspect ratio values (0.5 and 1). For each aspect ratio different blockage ratio values ranging from 0.1 to 0.25 and pitch-to-height ratio values varied from 5 to 10 have been studied. Channels have been studied at Reynolds number values of 20000-150000 and configured with round edged rib turbulators having a 45° angle to the main flow. Results show that lower pitch-to-height and higher blockage ratio values enhance heat transfer coefficient at the expense of increasing friction factor. Y.H. Liu [6] conducted heat transfer experiments at high rotation numbers. Equilateral triangle channel is used to simulate the leading edge cooling channel with three rib angles with the main flow (45°, inverted 45° and 90°) and four Reynolds number values ranging around 10000 to 40000. Five different rotational speeds ranging from 0 to 400 rpm have been investigated. By varying Reynolds numbers and rotation speeds, rotation and buoyancy number values ranged between 0 to 0.58 and 0 to 2.3 respectively. Trailing edge cooling channel have been simulated as a wedge-shaped channel with rotational speeds between 0 and 500 rpm. Leading and trailing surfaces have been equipped with 45° staggered ribs. Same Reynolds number values of the equilateral triangle channel have been used and once again rotation and buoyancy numbers ranged according to varying Reynolds numbers and rotation speeds. Results showed that 45° angled ribs have the highest thermal performance at stationary condition. 90° angled ribs have the highest thermal performance at the highest rotation number of 0.58. Wedge-shaped channel simulating the trailing edge cooling channel showed that heat transfer is high where strong slot ejection exists. Schueren et al. [7] studied the trapezoidal channel with two staggered rows of inclined impingement jets. The dimensionless pitch has been varied between 3 to 6 and for value of 3, cylindrical as well as conically narrowing bores with a cross section reduction of 25% and 50%, respectively have been investigated. Reynolds number values ranging between 10000-75000 have been studied and results showed that greater

dimensionless pitch decreases interaction between jets and so heat transfer. Also conical bores increases heat transfer by accelerating the jets. Wang et al. [8] investigated the characteristics of an impinging jet with a shallow-angle in a crossflow in the presence of a rib. Crossflow Reynolds number value was 80000 and jet Reynolds number values were 20000 and 40000. In all the cases rib presence has enhanced the heat transfer performance. At the lower value of jet Reynolds number value, rib presence has a more pronounced effect to increase jet performance. At the higher value of jet Reynolds number rib presence makes heat transfer rate more uniform yet the impinging jet effect tends to be weaker. Gao [9] studied on different jet array arrangements. Experimented basic inline jet arrays have three different configurations as 4X4, 8X4 and 8X8. Linearly stretched arrays have two cases as uniform diameter and the varying diameter. For the inline jet arrays, three jet heights (1, 3 and 5) and three Reynolds number values (5000, 10000 and 15000) have been investigated. For linearly stretched arrays, the same three jet heights and Reynolds number values of 2000, 6000 and 10000 have been investigated. Results showed that for the inline jet arrays heat transfer coefficient is higher when jet height equals 3 and for the linearly stretched array, the varying diameter case produces higher heat transfer coefficient at large Reynolds number values. Jordan et al. [10] investigated on cooling channel which has an aspect ratio value of 3 and equipped with inline V-shaped dimple arrays. V-shaped dimples had a depth-to-diameter ratio of 0.3 and spacing of 3.2 diameters at both streamwise and spanwise directions. Reynolds number values ranging from 10000 to 40000 have been studied. It has been reported that V-shaped dimple design is a promising alternative to traditional rib turbulators and hemispherical dimples. At lower Reynolds number values, the V-shaped dimples display heat transfer and friction behaviour similar to traditional hemispherical dimples. Higher Reynolds number values increase the magnitudes of secondary flows developed in the V-shaped concavities and so enhance the heat transfer much more than traditional hemispherical dimpled surfaces. It is also reported that this enhancement creates only marginal increase in pressure drop so as Reynolds number increases thermal performance of the V-shape dimpled channel also increases. Tran et al. [11] conducted PIV measurements at the fully developed portion of the rectangular channel (aspect ratio equals 2) having dimples at one wall. Three different Reynolds number

values (5000, 10000 and 15000) and dimple geometries (large dimple, small dimple and double dimple) have been investigated. The double dimples are reported to have better thermal performance because of the similar heat transfer augmentation comparable to the large dimples and lower friction factor augmentation comparable to the small dimples. Zhou [12] studied four single dimple geometries (square, triangle, circle, and teardrop) in the same test section with Reynolds number value of 21000. Results showed that teardrop dimple shows the most promising heat transfer characteristics. Monson et al. [13] investigated the low speed internal flow in a two-dimensional u-duct at two Reynolds number values (10^5 and 10^6) with Laser-Doppler velocimetry. Valuable data reported about the behaviour of the flow in a strongly-curved duct. Liou et al. [14] studied the effect of divider thickness on the local heat transfer distributions in a two-pass smooth square duct. Tested divider thickness to channel inlet hydraulic diameter ratios were 0.1, 0.25 and 0.5 at a Reynolds number value of 12000. Results showed that divider ratio of 0.25 provided the highest heat transfer values. Iacovides et al. [15] examined the rotating, square ended smooth u-duct aero-thermally. Reynolds number values were 100000 and 30000 during the conducted experiments for flow and heat transfer measurements respectively. Rotation number was 0.2 and working fluid was water for both cases. Results showed that at the immediate downstream of u-bend and within the u-bend, heat transfer distribution is highly affected by rotation. Liou et al. [16] also studied rotating square ended smooth two-pass cooling channel at rotation number ranging 0 to 0.2. The Reynolds number value was 10000 and working fluid was air in this investigation. Results showed that before a critical rotation number which is between 0.1-0.15, rotation has no prominent effect on the regionally averaged Nusselt number ratios in a two-pass cooling channel. Above the critical rotation number an overall enhancement on heat transfer performance of the duct occurs. Secondary flow at the rotating cases in the mid-turn is dominated by a single vortex most of which impinges outer part of the leading edge and greatly enhances the heat transfer rate. Chen et al. [17] investigated the local heat transfer and pressure drop distribution of a ribbed square cooling channel with different configurations in the turn region. Three turn configurations under three Reynolds number values (30000, 40000 and 50000) are examined and results showed that suitable turning vane

configurations with ribs are promising to meet cooling channel heat transfer requirements. Mochizuki et al. [18] investigated heat transfer and fluid flow in two-pass straight rectangular channels with ribs are attached to two opposite walls with an angle of 90° and 60° to the flow. Four different combination of 60° rib pattern is examined. For all test cases Reynolds number value is kept at 15000 and channel aspect ratio was 2. Results showed that 60° rib configurations have higher heat transfer rates than 90° configuration except in the bend and immediate downstream of the bend. It is also reported that among the four 60° rib arrangements the one coinciding secondary flows induced by rib and bend has higher heat transfer rate than other arrangements at the bend region and second pass. Han et al. [19] investigated two-pass, square, smooth and ribbed cooling channel via naphthalene sublimation technique. Transverse rib configurations with different rib height-to-hydraulic diameter ratios (0.063 and 0.094) and rib pitch-to-height ratios (10 and 20) have been studied. Three Reynolds number values (15000, 30000 and 60000) have been used in this study. Results showed that heat transfer rate at he turn and second pass is higher from heat transfer rate at first pass for all cases. It is also reported that heat transfer rate is increasing with increasing rib height and decreasing pitch ratio. Ekkad et al. [20] studied two-pass, square channel with one wall was ribbed and sprayed with thermochromic liquid crystals. Transient tests have been conducted with Reynolds number values ranging from 6000 to 60000. Rib configurations of 90°, 60°, 60° V and 60° V broken have been used with a rib height-to-hydraulic diameter ratio of 0.125 and rib pitch-to-height ratio of 10. Results showed that 60° V broken rib configuration has the highest heat transfer rate at the turn and second pass. However, 60°, 60° V and 60° V broken rib configurations have produced similar heat transfer enhancements at the first pass. For all rib configurations highest Nusselt number values are obtained at the top of the ribs and lowest values obtained immediately before and after the rib. Lee [21] have examined the two-pass trapezoidal cooling channel via naphthalene sublimation technique. Channels were equipped with transverse rib turbulators on one wall or two opposite walls. Results were obtained for Reynolds number values ranging 10000 to 60000. Studies revealed that in the entire ribbed channel cases studied, the regional average heat transfer was higher in the turn of the trapezoidal channel when flow enters to the channel from smaller

inlet section. However, immediately downstream of the turn, the regional average heat transfer decreases abruptly and keeps its level until the channel exit. In case of flow enters to the channel from larger section the regional average heat transfer continues to increase after the turn region so contrary to flow enters to the channel from smaller section, maximum regional average heat transfer values achieved at immediately downstream of the turn. It should be also noted that when flow enters from larger cross section inlet, pressure drop across the channel is higher. Liou et al. [22] studied the rotating u-duct which was equipped with transverse inline rib turbulators on the leading and trailing walls. Rib height-to-hydraulic diameter ratio and pitch-to-height ratio were 0.136 and 10 respectively. The Reynolds number value based on duct hydraulic diameter and bulk mean velocity was fixed at 10000 whereas the rotation number varied 0 to 0.2. Results showed that the rotating ribbed u-duct provides higher and stronger total averaged secondary flow hence heat transfer rate is enhanced. Liou et al. [23] also studied the 45° rib angle configuration with the same parameters. Results showed that the 45° ribs are found to reduce the friction loss to 60% of the 90° ribs for rotating duct under the same operating conditions. Agarwal [24] studied rectangular smooth and ribbed two-pass channels with and without rotation in two different aspect ratios (1:4 and 4:1) each have been performed for two different orientations of the test section (90° and 45°) by using naphthalene sublimation technique. The Reynolds number value is varied in the range of 5000 to 40000 and rotation number in the range of 0 to 0.12. Two different configurations of the transverse ribs first, rib height-to-hydraulic diameter ratio and pitch-to-height ratio of 0.3125 and 8 respectively and second, rib height-to-hydraulic diameter ratio and pitch-to-height ratio of 0.156 and 11.2 respectively were placed on the leading and the trailing sides. Results revealed that ribbed configurations are more sensitive to the rotation number variation hence while rotation number increases enhancement of heat transfer rate is higher for ribbed channel than smooth channel. Besides, ribbed configurations are less sensitive to orientation hence at both orientations acquired heat transfer enhancement levels are very close to each other. It is also documented that higher aspect ratios provide higher heat transfer enhancement because of the wider rib turbulator surfaces. Huh [25] conducted a series of experiment on cooling channels with a developing flow entrance condition. Two

different aspect ratios (1:4 and 2:1) with an extended range of the rotation number and buoyancy parameter for the each aspect ratio value were studied. The maximum rotation number and buoyancy parameter for the channel aspect ratio value of 1:4 was 0.67 and 1.9, respectively. For the 2:1 channel, these values were 0.45 and 0.85, respectively. Rib spacing and rib height effect on heat transfer is studied for the channel which has an aspect ratio value of 1:4. Three different pitch-to-rib height ratios (2.5, 5 and 10) for a selected rib height-to-hydraulic diameter ratio (0.078) were investigated to understand the effect of rib spacing on heat transfer rate. To investigate the effect of rib height; rib height-to-hydraulic diameter ratio and pitch-to-height ratio of 0.156 and 10 is studied and results are compared with the rib height-to-hydraulic diameter ratio of 0.078 at the same rib spacing value. For the channel aspect ratio value of 2:1; smooth channel surface condition was studied. For each channel aspect ratio and surface condition, five Reynolds number values were studied up to 40000 and at each Reynolds number values, five rotational speeds were considered up to 400 rpm. The results showed that rotation can cause significant increase in heat transfer rate on the first pass trailing surface of both aspect ratio channels. In ribbed channels the leading surface of the first pass has shown a dramatic decrease in heat transfer with rotation and in the second pass, both surfaces with ribs showed very similar effects of rotation. The effect of rotation varied with the rib spacing and rib pitch-to-height ratio of 2.5 showed the highest sensitivity to the rotation. The rib height in the channel aspect ratio value of 1:4 showed minimal impact due to the large distance between the leading and trailing surfaces. The tip cap heat transfer for both channels showed large increases with rotation. Fu [26] investigated the effects of aspect ratio and orientation angle with respect to the plane of rotation on smooth and rib turbulated two-pass channels. Experiments conducted configurations which had 90$^{\text{o}}$ and 45° of channel orientations with respect to rotation plane and channel aspect ratios of 4:1, 2:1, 1:1, 1:2 and 1:4. Four different Reynolds number values have been studied (5000, 10000, 25000 and 40000) and the rotation speed is kept fixed at 550 rpm for all tests. Rib turbulators which have 45$^{\text{o}}$ angle with the flow direction and rib pitch-to-height ratio of 10 are placed on leading and trailing surfaces of the channels. Results revealed that level of rotation effect on channel depends on channel aspect ratio for both smooth and ribbed

14

configurations. The low aspect ratio channels cause larger variations of heat transfer with respect to large aspect ratio channels. Square channel shows the least sensitivity to the rotation number and rotation effect also decreases with increasing Reynolds number value. The heat transfer rate is more uniform at 45° channel orientation and overall level of the heat transfer rate enhancement at ribbed channel geometries are comparable for all aspect ratio values. However, lowest pressure loss value for ribbed channels occurs at an aspect ratio value of 1:4, as a result of this highest thermal performance have been obtained at this aspect ratio value. Y.H. Liu [27] studied on the same experimental set up at which Fu [26] used earlier. Experiments are carried on same Reynolds number and rotational speed values. Only the channel aspect ratio value of 1:2 at a 90° orientation with respect to rotation plane has been investigated. Rib turbulators had once more 45° angle with the flow direction but rib pitch-to-height ratio value have been ranged from 3 to 10 this time. Results showed that for stationary cases highest heat transfer coefficients are produced at rib pitch-to-height ratio of 5 and highest pressure drop has occurred at rib pitch-to-height ratio of 3. Highest thermal performance is produced between rib pitch-to-height ratios of 5 to 7.5 depending on the Reynolds number value. For rotating cases highest heat transfer coefficients are produced between rib pitch-to-height ratios of 5 to 7.5 and highest pressure drop has occurred at rib pitch-to-height ratio of 5. Highest thermal performance is produced at rib pitch-to-height ratio of 7.5 at rotating cases. For both cases lowest pressure drop is achieved at rib pitch-to-height ratio of 10. Hylton et al. [28] investigated experiments to acquire both aerodynamic and heat transfer distributions over the surfaces of two highly loaded, low solidity turbine nozzle guide vanes (C3X and MarkII) in moderate temperatures, three vane linear cascade under steady-state conditions. The independent parameters were Mach number, Reynolds number, turbulent intensity and wall temperature-to-gas temperature ratio. Results showed that heat transfer distribution on vane surface is sensitive to the surface pressure distribution (isentropic Mach number) especially where the boundary layer experiences transition. The heat transfer distribution seems mostly influenced by Reynolds number and it also strongly affects the onset and extent of boundary transition. Turbulent intensity and wall temperature-to-gas temperature ratio do not have a clear effect on heat transfer distribution but changes in these

15

parameters create small but systematic changes on heat transfer distribution. Dees [29] investigated on internally and externally cooled experimental model which utilizes Bi method to produce non-dimensional surface temperature measurements that are representative of engine conditions. C3X vane of Hylton et al. [28] is scaled 3.88 times and equipped with a two-pass channel which is placed at the leading edge and vane centre and a radial channel which is placed at the trailing edge for cooling purposes. Test section was a simulated three vanes, two passages linear cascade. Results showed that at nearly all conditions addition of film cooling decreases the surface temperatures. However, for high momentum flux ratios the film cooling jet detaches from the surface and vane surface temperature becomes higher relative to non-film cooled case at those small jet detachment regions. Davidson et al. [30] investigated on the test set-up that Dees [29] previously studied. Coated and twelve times scaled-up C3X vane of Hylton et al. [28] have been used to model the conjugate heat transfer effects of a real engine. Experiments conducted for a range of coolant Reynolds number values on the same internal cooling configuration that Dees [29] studied. Results showed that thermal barrier coating dampens the variations in overall coolant effectiveness caused from changes in coolant Reynolds number value so it lowers the detrimental effects of high coolant blowing ratios. It is also discovered that thermal barrier coating application increases the performance of standard round coolant holes.

1.4.2   Numerical Studies

The numerical simulations related with the aforementioned experimental studies have been conducted with various type methodologies like Large Eddy Simulation (LES), Detached Eddy Simulation (DES) and RANS-based turbulence modeling by employing different commercial and in-house flow solvers. These studies have been roughly arranged in this literature survey and investigations which employing similar methods have been mentioned together.

LES has been used by many investigators to simulate heat transfer problems. In LES, idea is modeling on the small isentropic scales and resolving

the energy containing eddies. The LES applications became available by the exponential increase of computational power at last decades however; it is still limited with simulating the small portions of actual computational domains. Patil et al. [31], Tafti [32] and Abdel-Wahab [33] investigated on periodic flows of rib turbulated channels by using LES. Sewall et al. [34, 35] also investigated on LES simulations and studied with bigger computational domains. DES is a hybrid URANS-LES method that makes it more feasible to apply large simulation problems with respect to LES method. Investigation of Viswanathan [36] is a very good example to DES studies. Saha et al. [37] also conducted LES studies and compared them with URANS. RANS methods have been preferred over LES and DES applications because of their lower computational needs and relatively short duration of simulations. Studies conducted by RANS methods can be summarized as Chen et al. [17], Jang et al. [38], Al-Qahtani et al. [39], Rokni et al. [40], Rumsey et al. [41], Sleiti [42] and Su [43]. York et al. [44] and Saha et al. [45] investigated the success of URANS applications on turbine cooling methods. Conjugate heat transfer analyses have been conducted by RANS-based turbulence models and their pros and cons have been revealed by various commercial and in-house codes. The most popular test case for validation was experiments of Hylton et al. [28] on MARK-II and NASA-C3X vanes. Numerical studies on MARK-II test case have been conducted by Bohn et al. [46], Rahman [47] and Mangesh [48] and numerical studies on NASA-C3X test case have been conducted by York [49], Facchini et al. [50], Findlay [51] and Ledezma et al. [52]. Peigang et al. [53] was the only researcher investigated on both cases. The newly introduced four-equation RANS turbulence model V2-f has been implemented to conjugate heat transfer analyses by Luo et al. [54] and Mangani et al. [55]. It has also been used for various different cooling problems by Luo et al. [56, 57] and Takashashi et al. [58].

Patil et al. [31] investigated the LES of flow and heat transfer in a square stationary in-line ribbed duct with rib height-to-hydraulic diameter ratio of 0.1 and 0.05 and rib pitch-to-height ratio of 10 and 20. A new methodology has been presented to model the heat transfer by using both Neumann and Dirichlet wall boundary conditions. Reynolds number values of 20000 and 60000 are investigated on a periodic computational domain and results showed that

presented wall modeled LES methodology reduced the overall computational complexity by factors of 60-140 compared to resolved LES without any significant loss in accuracy. The resolved LES data which has been used to compare wall modeled LES solutions were obtained from the studies of Tafti [32]. Two mesh resolutions (96^3 and 128^3) have been investigated by Tafti [32]. Results showed that calculations capture the mean flow structures and turbulent root mean square (rms) quantities with precision and both mesh resolutions compare well with experimental data with insignificant differences. The friction factor and Nusselt number values were under predicted when compared to measurements in literature. Abdel-Wahab [33] investigated on fully developed flow and heat transfer in a staggered 45º ribbed duct and orthogonally rotating 90º ribbed duct. In the first case rib pitch-to-height ratio was 10 and a rib height-to-hydraulic diameter ratio was 0.1. The Reynolds number value based on the bulk flow rate and hydraulic diameter was 47300. In the second case Reynolds number value based on the bulk flow rate was 20000. Three rotation number values (0.18, 0.35 and 0.67) and two buoyancy number values (0.12 and 0.29) were investigated for this case. Rib pitch-to-height and rib height-to-hydraulic diameter ratios were the same as in the first case. Results showed that LES method is a very powerful tool in predicting mean flow and heat transfer quantities for different Reynolds, rotation and buoyancy number values. Sewall et al. [34, 35] carried on LES analyses on a stationary straight duct equipped with six rib turbulators and two-pass channel equipped with in-line orthogonal rib turbulators that three pairs are placed at the first and three pairs are placed at the second pass respectively. Results showed that at straight channel mean flow velocities reach to fully developed state at the fourth rib and heat transfer coefficients reach to fully developed state at the third rib. The two-pass channel results revealed that LES has very accurate predictions for highly separated flows which have high thermal gradient at both smooth and rib turbulated wall geometries. Viswanathan [36] conducted DES analyses on well known experimental cases like back-facing step, periodic rib configuration with Coriolis and buoyancy forces and two-pass rib turbulated channel. Studies of Viswanathan were in conjunction with the Sewalls investigations and results revealed that DES is superior to the RANS turbulence models. DES accurately predicts the primary and secondary flow features, the turbulence characteristics

and the heat transfer in both stationary ducts and in rotating ducts, where the effects of Coriolis forces and centrifugal buoyancy forces are dominant. DES computations are carried out at a computational cost that is almost an order of magnitude less than the LES with little compromise on the accuracy. Results also revealed that the capabilities of DES in predicting the transition to turbulence are inadequate however, once the flow becomes fully turbulent DES shows good agreement with the experiments and LES. Saha et al. [37] compared LES with URANS for both flow and heat transfer quantities in a rotating duct equipped with staggered transverse rib turbulators. The LES results were based on dynamic Smagorinsky model for the sub-grid stresses. The URANS analyses are conducted with two-equation k-ε turbulence model. Both Coriolis and centrifugal buoyancy effects are included in the simulations. The URANS computations have been carried out for Reynolds number values ranging from 12500 to 100000, rotation number values ranging from 0 to 0.5 and density ratio values ranging from 0 to 0.5. LES results were only reported for a single Reynolds number value of 12500 without rotation and with rotation value of 0.12 and density ratio value of 0.13. Results revealed that both URANS and LES analyses agree well with the experimental data and compared to URANS, LES has higher heat transfer predictions. Chen et al. [17] carried out numerical analyses on two-pass rib turbulated channel for Reynolds number value of 40000 by using k-ε, SST and Omega Reynolds Stress (ORS) turbulence models. All turbulence models captured the trend of heat transfer and pressure drop. All turbulence models over predicted heat transfer values and among three turbulence models ORS model provided best predictions. Jang et al. [38] carried out numerical studies of three-dimensional flow and heat transfer for a two-pass square channel with and without 60° angled parallel rib turbulators at Reynolds number value of 30000. The rib height-to-hydraulic diameter ratio was 0.125 and the rib pitch-to-height ratio was 10. The finite analytic method solved the RANS equations in conjunction with a near-wall second-order Reynolds stress (second-moment) closure model, and a two-layer k-ε turbulence model. Results showed that the angled rib turbulators and the sharp turn of the two-pass channel has been produced strong non-isotropic turbulence. As a result of this the near-wall second-moment closure model provided an improved heat transfer prediction in comparison with the k- ε model. Al-Qahtani et al. [39] investigated on rotating

cooling channels equipped with 45° rib turbulators at different orientation angles. The rib height-to-hydraulic diameter ratio was 0.078 and the rib-pitch-to-height ratio was 10. The rotation number and inlet coolant-to-wall density ratios were varied from 0.0 to 0.28 and from 0.122 to 0.40 respectively while the Reynolds number value was fixed at 10000 and channel aspect ratio was 4:1. The channel orientations with respect to rotation direction were 90° and 135°. Results show that second-moment closure model employed with the multi-block RANS method predicted fairly well the complex three dimensional flow and heat transfer characteristics. Rokni et al. [40] presented the numerical results of fully developed, three-dimensional turbulent flow duct flows. Various duct shapes are investigated (square, rectangular, trapezoidal, triangular and wavy) with Explicit Algebraic Stress Model (EASM). Results revealed that predictions were in excellent agreement with the well established correlations extracted from experimental studies, besides calculation procedure was robust and computational cost was low. Rumsey et al. [41] also used EASM to numerically solve previously mentioned Monson's [13] test case along with three other turbulence models namely SST, Spalart-Allmaras and RSM. Results revealed that EASM performs better than one and two-equation turbulence models. All turbulence models lack to capture the enhanced turbulence close to the outer wall and only RSM succeed to simulate suppressed turbulence the close to inner wall. Sleiti [42] investigated on both smooth and rib turbulated internal cooling channels with and without u-bends. Rotation and buoyancy effects are investigated separately and simultaneously by employing isotropic two-equation (k-ε and k-ω) and anisotropic RSM turbulence models. Results showed that k- ε and k-ω models are far from simulating the anisotropic nature of cooling channel flows caused from rib turbulators, rotation, buoyancy and curvature. RSM on the other hand, by the advantage of being an anisotropic turbulence model, was in a very good agreement with the available experimental data. Su [43] has been validated cooling channels flows which have been equipped with different type of turbulators. Various rotation, buoyancy and Reynolds number values have been investigated with a multi-block RANS solver which uses a near-wall second-moment turbulence closure. First, rotating rectangular channel of aspect ratio 4:1 with V-shaped rib turbulators has been investigated. The rib height-to-hydraulic diameter ratio was 0.078 and the rib pitch-to-height ratio was 10. The rotation

number and inlet coolant-to-wall density ratio were varied from 0.0 to 0.28 and from 0.122 to 0.40, respectively, while the Reynolds number values was varied from 10000 to 500000. Three channel orientations (90°, -135° and 135°) with respect to the plane of rotation were also investigated. Second, rotating rectangular channel of aspect ratio 4:1 with staggered arrays of pin-fins has been studied. The pin length-to-diameter ratio was 2.0, and the pin spacing-to-diameter ratio was 2.0 in both the streamwise and spanwise directions. The rotation number and inlet coolant-to-wall density ratio were varied from 0.0 to 0.28 and from 0.122 to 0.20 respectively while the Reynolds number values was varied from 10000 to 100000. For the rotating cases, the rectangular channel was oriented at 150 degrees with respect to the plane of rotation. Third, rotating two-pass rectangular channel with 45° rib turbulators and three different aspect ratios (1:1, 1:2, and 1:4) were investigated. Flow and heat transfer predictions for two Reynolds number values (10000 and 100000) were carried out with fixed rib height and the rib-pitch-to-height ratio were 10. The channel orientations were set as 90° and the rotation number and inlet coolant-to-wall density ratio varied from 0.0 to 0.28 and from 0.13 to 0.40 respectively. The fourth case was rotating two-pass smooth channel with three aspect ratios (1:1, 1:2, and 1:4). Flow and heat transfer predictions for two Reynolds number values (10000 and 100000) were carried out. The rotation number and inlet coolant-to-wall density ratio varied from 0 to 0.28 and from 0.13 to 0.40 respectively. Results show that predictions of multi-block RANS solver which uses a near-wall second-moment turbulence closure were very good agreement with the experimental data, especially for the first and second cases. York et al. [44] studied numerically on a rib turbulated straight channel. Two steady simulations with RKE and RSM turbulence models and an unsteady simulation with an in-house three equation turbulence model have been carried out at Reynolds number value of 24000. Results showed that although, RSM has been provided the better predictions both RKE and RSM turbulence models were unable to simulate the unsteady vortex shedding over the rib turbulators. Results of the unsteady in-house turbulence model provided the best predictions with a slight over prediction of maximum heat transfer after each rib turbulator. Saha et al. [45] carried out flow and heat transfer simulations in a rib turbulated rectangular passage for two

different aspect ratio values (4:1 and 1:4). Rotation number value has been varied from 0.12 to 0.5. Reynolds number and density ratio values have been 25000 and 0.13 respectively for all simulations. Results showed that the URANS procedure utilizing two-equation k-ε turbulence model has been good agreement with the experimental data. Bohn et al. [46] conducted one of the earliest three dimensional conjugate heat transfer analysis and investigated the effect of thermal barrier coating on MARK-II vane. Algebraic turbulence closure model of Baldvin-Lomax has been used in this study and results were in good agreement with the experimental data. Rahman [47] has also been studied on MARK-II vane but these analyses were two-dimensional. The RKE and Spalart-Allmaras turbulence models have been employed in this study and results showed that RKE turbulence model predicted heat transfer quantities and pressure distribution slightly better than Spalart-Allmaras. Lately Mangesh [48] conducted two-dimensional analyses on MARK-II vane by using RKE turbulence model and reported that heat transfer coefficient results deviates 30% from the experimental data at the leading edge suction side. It is also reported that cause of this deviation might be the relaminarization of the flow at the leading edge. Hylton's [28] other test case, the NASA-C3X vane has more often been the choice of the researchers with respect to MARK-II vane because of its more realistic geometry and well defined leading edge. York [49] was one of the earliest researchers that conducted the numerical simulations on NASA-C3X test case. In this study two mainstream operating conditions, one subsonic and one transonic, have been investigated three dimensionally to identify the accuracy of different turbulence models at different flow conditions. Standard and Realizable k-ε turbulence models have been used and latter turbulence model exhibited the best agreement with the experimental data. Both turbulence models are lack to simulate the laminar flow and transition to turbulence at the downstream of the leading edge on the suction side. Facchini et al. [50] used variants of k-ε turbulence model (Low-Reynolds, ReNormalization group and High-Reynolds versions) to three dimensionally simulate the NASA-C3X test case. Results showed that k-ε based two-equation turbulence models are not capable of solving turbulence transition occurring at the suction side of the blade and among three k-ε turbulence models best agreement with the experimental data has been acquired by High-Reynolds k-ε turbulence model. Findlay [51] studied

the same experimental test run (run 112) that Facchini et al. [50] used to study by implementing Spalart-Allmaras turbulence model to the simulations. Results showed that Spalart-Allmaras turbulence model has better predictions than High-Reynolds k-ε turbulence model at both suction side and pressure side. Ledezma et al. [52] used four different turbulence models (standard k-ε, k-ω, SST and Omega Stress models) to three dimensionally simulate the NASA-C3X test case. Results showed that all four turbulence models, especially SST, are accurately predicting the metal temperature and heat transfer coefficient distributions on the pressure side and downstream of the suction side at the mid span of the NASA-C3X test case. All three eddy viscosity turbulence models and anisotropic Omega Stress model lack to simulate the transitional flow occurring at the suction side of the blade by using both wall integration and wall function meshes. Peigang et al. [53] investigated on both of the NASA-C3X and MARK-II vanes. Different commercial codes (FLUENT and CFX) and an in-house code are used with various turbulence models (standard k-ε, k-ω, SST, SST k-ω GamaTheta). Among all turbulence models available at commercial codes, SST k-ω GamaTheta turbulence model of CFX provided better predictions than other turbulence models. The in-house code with adjusted transition modeling provided the best agreement with the available experimental data. Luo et al. [54] has been implemented V2-f turbulence model to different conjugate heat transfer analyses. Luo et al. [54] investigated on three different test runs of (run 112, 154 and 158) NASA-C3X test case with low-Reynolds k-ε, non-linear quadratic k-ε and V2-f turbulence models. Conducted simulations have been revealed that V2-f turbulence model is in the closest agreement with the experimental data and has the ability of representing the boundary layer transition at the suction side which two-equation eddy viscosity models generally lacks. Mangani et al. [55] has been implemented V2-f and three other (Spalart-Allmaras, SST and two-layer) turbulence models to the conjugate heat transfer analyses of a different version of NASA-C3X test case which includes both internal and external cooling. The internal cooling has been achieved by ten radial cooling channels and external cooling has been undertaken by shower-head application at the leading edge. Results showed that all of the turbulence models have been in good agreement with the experimental data in terms of blade temperature and aerodynamic loads. Heat transfer coefficient results of all turbulence models except two-layer

turbulence model have shown good agreement with the experimental data. Spalart-Allmaras turbulence model has shown the best fitted slope with the experimental data and V2-f turbulence model predicted the local maximum heat transfer coefficient at the suction side accurately. In previous studies both Spalart-Allmaras and SST turbulence models have been reported as unsuccessful to predict heat transfer coefficient distribution because of their inability to model the boundary layer transition. However, in this test case flow injected from shower-head to the main flow introduces additional turbulence and reduces laminar flow region at the suction side and as a result improves the predictions of Spalart-Allmaras and SST turbulence models. The capabilities of V2-f turbulence model has been examined with different simulations related turbine cooling besides conjugate heat transfer analyses. Luo et al. [56] studied the numerical simulation of two and three dimensional two-pass cooling channels with V2-f turbulence model. Results showed that V2-f turbulence model predicted unphysical friction factor values at the downstream of the bend region because of the flow re-attachment. This was caused from the inaccurate prediction of high turbulence level and it should also cause poor prediction of heat transfer quantities. Comparisons against three different turbulence models (k-ε, SST and RSM) revealed no superiority of V2-f turbulence model against other turbulence models in terms of pressure distribution and velocity profile predictions. Luo et al. [57] have also implemented the V2-f turbulence model to the non-conjugate analyses of turbine vane and rotor geometries with three other (k-ε, SST and RSM) turbulence models. Results showed that inlet turbulent length scale is very effective on freestream turbulence decay, turbulence level at the turbine passage and boundary layer transition. Analyses with different turbulent length scale values have shown the importance of deciding on a reasonable turbulent inlet boundary condition to accurately predict the heat transfer quantities. Among the investigated turbulence models V2-f turbulence model provided the best predictions in terms of heat transfer coefficient distribution. V2-f and SST turbulence models have shown similar behaviours about the evolution of freestream turbulence along the turbine passage with RSM results but k-ε predicts high turbulence values along the turbine passage and this causes over-prediction of the heat transfer quantities. Takashashi et al. [58] investigated on the blade leading edge with circular cooling holes in order to contribute durability

assessment of the turbine blades. Steady RANS, unsteady RANS and DES analyses have been carried out to simulate wind tunnel experiments and solve thermal convection. Steady RANS analyses have been conducted with SST turbulence model and unsteady RANS analyses have been conducted by using V2-f and Spalart-Allmaras turbulence models. DES analysis has been based on Spalart-Allmaras turbulence model. Results showed that unsteady V2-f and DES analyses provided better predictions in terms of cooling effectiveness on the leading edge surface with respect to unsteady Spalart-Allmaras and steady SST turbulence models. DES and unsteady V2-f turbulence model evaluated the unsteady temperature fluctuations induced by the vortex structures explicitly. However, unsteady simulations carried out with Spalart-Allmaras turbulence model could not clearly predict these anisotropic motions.

1.5   Outline of the Study

The organization of this thesis can be given as follows:

In Chapter 1 the general information about turbine cooling technologies was given briefly. The objectives and limitations of the study was given item by item and this part was followed by a detailed literature review of experimental and numerical studies.

In Chapter 2 governing equations of fluid flow, heat transfer and turbulence models employed in this thesis will be presented. In this chapter a closer look will be taken on V2-f turbulence model. Additional literature review which is only related with the studies conducted with this turbulence model will be listed and different versions of V2-f turbulence model will be documented in detail.

In chapter 3 five different test cases simulated in this thesis will be introduced in detail. Solid models, boundary conditions will be presented and numerical modeling approaches related with each test case will be discussed.

Chapter 4 is devoted to the presentation of the results derived from numerical simulations. Findings related with each test case will be discussed and success of each turbulence model will be evaluated.

Chapter 5 includes the general conclusions drawn from this study and provides recommendations for the future works.

CHAPTER 2

GOVERNING EQUATIONS

The fluid motion and heat transfer are governed by a set of non-linear partial differential equations. These equations completely define and manage the conservation of mass, momentum and energy flow through a medium (solid, gas or liquid) however, simulations using RANS-based methods require additional turbulence closure equations. Equations given in this chapter are in conservative form and index notation.

2.1 Flow and Energy Equations

Equations that govern fluid motion and heat transfer are continuity, momentum and energy equations. Details of the formulations below can be found in Blazek [59].

2.1.1 Continuity Equation

Continuity equation based on the theory that mass can neither be created nor destroyed. The continuity equation for a three-dimensional, unsteady, compressible flow is;

$$\frac{\partial \rho}{\partial t} + \frac{\partial}{\partial t}\left(\rho u_i\right) = 0 \tag{2.1}$$

2.1.2 Momentum Equation

Momentum equations are derived from the Newton's 2nd law and they express that applied forces on a fluid volume must be balanced.

$$\frac{\partial}{\partial t}(\rho u_i) + \frac{\partial}{\partial x_j}(\rho u_j u_i) = -\frac{\partial p}{\partial x_i} + \frac{\partial \tau_{ij}}{\partial x_j}$$

(2.2)

For fluids like air and water Isaac Newton stated that shear stress caused from viscosity is proportional to the velocity gradient therefore, these type of fluids are designated as Newtonian fluid. Starting from the Newton's statement George Stokes derived the shear stress expressions (τ_{ij}) for these type of fluids;

$$\tau_{ij} = 2\mu S_{ij} + \lambda \frac{\partial u_k}{\partial x_k}\delta_{ij}$$

(2.3)

Where shear strain rate (S_{ij}) can be defined as;

$$S_{ij} = \frac{1}{2}\left(\frac{\partial u_i}{\partial x_j} + \frac{\partial u_j}{\partial x_i}\right)$$

(2.4)

In viscosity tensor formulation λ represents the second viscosity coefficient and μ denotes the dynamic viscosity. One of these viscosity representations must be eliminated by relating them with each other. Stokes's hypothesis was based on that for a Newtonian fluid total normal viscous stress should be equal to zero, in other words sum of the normal stresses should be equal to the pressure. In order to close the shear stress expression for the normal stresses Stokes introduced the following relation;

$$\lambda + \frac{2}{3}\mu = 0$$

(2.5)

With the exception of extremely high temperatures or pressures, there is still no experimental evidence that Stokes's hypothesis does not hold so it is generally used to eliminate λ from the shear stress expression. After setting the

value of λ, shear stress expression for a compressible Newtonian fluid appears in the following relation;

$$\tau_{ij} = 2\mu S_{ij} - \left(\frac{2\mu}{3}\right)\frac{\partial u_k}{\partial x_k}\delta_{ij}$$ (2.6)

For an incompressible flow, second term in the equation 2.6 which corresponds to the divergence of the velocity disappears (continuity equation).

2.1.3   Energy Equation

According to first law of thermodynamics, the change of energy for a system is the result of applied work and heat transfer through that system. The energy equation is given as;

$$\frac{\partial}{\partial t}\left(\rho E\right) + \frac{\partial}{\partial x_j}\left(\rho u_j H\right) = \frac{\partial}{\partial x_j}\left(u_i\tau_{ij}\right) + \frac{\partial}{\partial x_j}\left(k\frac{\partial T}{\partial x_j}\right)$$ (2.7)

Iteration of thermal quantities are run and total amount of energy in the computational domain is kept constant by this governing equation.

2.2   Turbulence Modeling

2.2.1   Hierarchy of Turbulence Models

Governing equations of fluid motion and heat transfer can not be solved analytically, except a few simple cases. Therefore, most flow cases must be solved numerically by discretizing the differential equations. Different numerical approaches have been developed to solve the random motions occurring at wide range of scales in time and space. Although, accurate definition of turbulence requires very fine meshes and high computational resources, less demanding methods which can provide acceptable results have been developed for industrial

purposes. An overview of the classes of turbulence models, which are sorted according to their decreasing level of complexity, is displayed at the following figure.
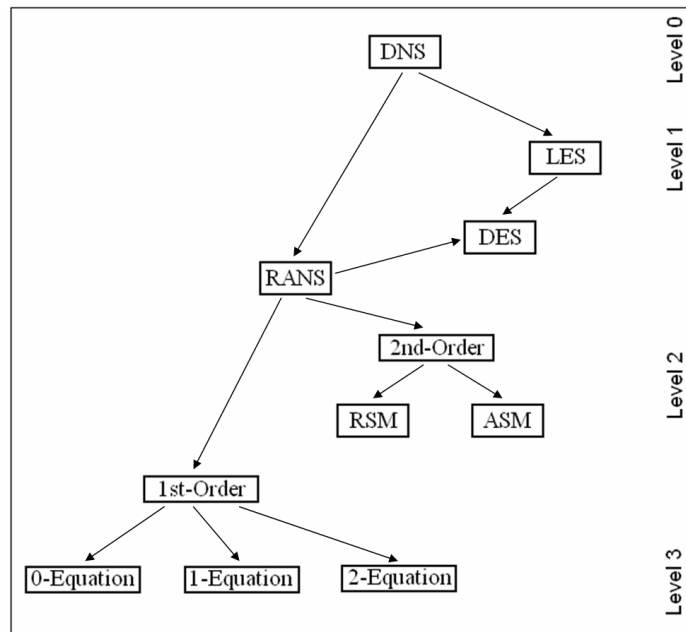
Figure 2.1. Turbulence model classes

The high complexity of turbulence models also requires high computational power so Figure… can be also perceived as the order of turbulence models according to their difficulty to apply industrial purposes. The advancements in computer technology only let us to use levels under the RANS actively for now but applications of the higher levels are becoming more and more available with the exponential growth of the computational resources.

2.2.2   Direct Numerical Simulation (DNS)

Direct Numerical Simulations solve the governing equations without modeling and attempts to accommodate all turbulent length scales in time and space. However, turbulence causes very small length scales in terms of size and duration and this makes DNS a very challenging and demanding type of flow analysis. The rough estimate of number of grid size and time step requirement

for DNS can be related with Reynolds number. The Kolmogorov length scale (η) is assumed as the smallest length scale in the flow and L as the largest (integral) length scale such as boundary layer thickness. Then by using turbulent dissipation and Kolmogorov length scale relations ($\varepsilon \equiv u_{rms}{}^3 / L$ and $\eta = \left(v^3 / \varepsilon \right)^{1/4}$) and keeping in mind that at least 4-6 grid points should be used for each Kolmogorov length scale in each direction, total grid size can be estimated as follows;

$$\left(6 \frac{L}{\eta} \right)^3 = 216 (\text{Re})^{9/4} \tag{2.8}$$

Time scale should also be adjusted such that for the smallest length scale Courant number value should be lower than 1. As a result of this total number of time integration steps becomes;

$$\left(\frac{L}{\eta} \right) = (\text{Re})^{3/4} \tag{2.9}$$

Above equations are evaluated with the assumption of a cubical computational domain however, even for a simple duct flow domain extends to each direction for several integral length scales. Thus, with the capability of available computers DNS applications are limited to simple geometries at relatively low Reynolds numbers. Although, DNS is inappropriate for industrial purposes but it provides important data on the process of developing and improving other turbulence models. Besides, it can be applied to flow cases of which are very difficult or impossible measure experimentally. Therefore, DNS is a very important tool to understand turbulent flow and its importance grows rapidly with the development of more powerful computers.

2.2.3   Large Eddy Simulation (LES)

Large Eddy Simulation is a trade of between DNS and RANS, where all scales of turbulence are resolved and modelled respectively. Turbulent flow can be characterized by eddies with a wide range of length and time scales. LES is

based on the observation that large eddies which are mainly responsible from transport of mass, momentum and energy are highly dependent on flow conditions and geometries under consideration so they must be resolved directly. Same observation also states that small eddies are more universal and tend to be isentropic so their effect can be modelled by a subgrid scale model. The homogeneity of the smaller scales makes the subgrid scale turbulence model applicable to wide range of flow regimes and conditions. Modeling of small eddies instead of resolving them results in much less restrictive mesh and time step requirements with respect to DNS hence, analysis with an order of magnitude higher Reynolds number is available with LES. However, current grid sizes and total number of integral time steps is very high for available computational power and being a regular tool of industrial is still impossible. In addition to this, if smaller scales are effective in the flow such as combustion problems, resolving these scales brings the analysis closer to the DNS. Therefore, in order to further reduce computational requirements, development studies on approximate wall models which function in conjunction with LES, with an acceptable loss of accuracy, are continuing.

2.2.4   Detached Eddy Simulation (DES)

In Detached Eddy Simulation approach, unsteady RANS models are employed in the boundary layer and remaining regions are treated with LES. The RANS region is naturally associated with the turbulent structures which can be assumed isentropic and LES is concerned with the turbulent regions where large unsteady turbulent scales take place so RANS model behaves like the subgrid scale model of LES. Application of unsteady RANS methods in the boundary layer region causes less prohibitive mesh requirements with respect to LES so analysis with an order of magnitude higher Reynolds number is available with DES. The DES approach is frequently employed for applications such as high Reynolds external aerodynamics simulations which LES can not be used. However, DES would be still demanding for many applications and require significant computational time. Therefore, it is recommended to employ full RANS approach

for practical cases. The majority of DES approaches rely on only to the grid distribution to recognize if the location is a RANS or LES region so they are insensitive to local flow features. Current DES studies intend to shift between RANS and LES depending to the eddy length scale hence make the computation more independent from grid density.

2.2.5   Reynolds Averaged Navier-Stokes (RANS)

2.2.5.1 Reynolds Decomposition and Boussinesq Hypothesis

Reynolds Averaged Navier-Stokes approach is the most famous approximate treatment applied to the turbulent flows. The methodology is based on the decomposition of governing equations of flow and heat transfer into a mean and a fluctuating part as in the following equation;

$$\phi = \bar{\phi} + \phi' \tag{2.10}$$

Resultant equations then solved for mean values. RANS equations are identical to the form of the governing equations before the decomposition with the exception of an additional term. Representative decomposition of the incompressible momentum equation can be written as follows;

$$\frac{\partial}{\partial t}\overline{(\bar{u}_i + u'_i)} + \frac{\partial}{\partial x_j}\left[\overline{(\bar{u}_j + u'_j)(\bar{u}_i + u'_i)}\right] =$$

$$= -\frac{1}{\rho}\frac{\partial}{\partial x_i}\overline{(\bar{p} + p')} + \nu \frac{\partial^2}{\partial x^2_j}\overline{(\bar{u}_j + u'_j)} \tag{2.11}$$

The cross multiplication at the second term of left-hand side of the equation 2.11 results with four different terms which can be written as;

$$\frac{\partial}{\partial x_j}\left(\overline{\bar{u}_j \bar{u}_i} + \overline{\bar{u}_j u'_i} + \overline{\bar{u}_i u'_j} + \overline{u'_i u'_j}\right) \tag{2.12}$$

First term in the equation 2.12 is ruled out from incompressible continuity equation, second and third terms are also ruled out because time average of the velocity fluctuations is zero. Last term however, does not necessarily have to be equal to zero because time average of two fluctuating components may have a correlation in space and time. This non-zero term is the turbulent character of the flow and called Reynolds stress tensor. The difficulty is that Reynolds stress tensor $(-\rho\overline{u_i'u_j'})$ is a 3x3 symmetric tensor which introduces 6 independent variables to the problem so it has to be modelled. Majority of the turbulence modeling efforts employ the Boussinesq hypothesis, which was presented approximately 20 years before the equations of RANS have been derived. Boussinesq hypothesis is based on that momentum transfer in a turbulent flow is dominated by the mixing caused by large eddies so it assumes that the Reynolds stress tensor is related linearly to the mean rate of strain as in a laminar flow. For a Reynolds averaged compressible flow it can be written as;

$$-\rho\overline{u_i'u_j'} = 2\mu_T \overline{S}_{ij} - \frac{2}{3}\left(\rho k + \mu_T \frac{\partial \overline{u_i}}{\partial x_i}\right)\delta_{ij} \qquad (2.13)$$

Where k stands for turbulent kinetic energy and μ_T denotes the turbulent (eddy) viscosity which is not a physical characteristic of the fluid but a function of local flow conditions and is strongly affected by flow history effects. All first-order turbulence models are merely different approaches to calculate the μ_T unknown in equation 2.13. Once this value is obtained it is simply added to the laminar viscosity and so Reynolds stress tensor arouse at equation 2.12 during the Reynolds decomposition is eliminated. The hypothesis of Boussinesq is, at least from engineering point of view, very attractive since it requires only the evaluation of μ_T so vast numbers of first-order turbulence models have been developed. All turbulence models utilized in this thesis study, excluding RSM, rely on Boussinesq hypothesis. Formulations at the following parts belong to the turbulence models employed in this thesis study and details of them can be found in Hoffmann et al. [60,61,62], ANSYS Fluent Theory Guide [63] and ANSYS Fluent V2-f Turbulence Model Manual [64].

2.2.5.2 Realizable k-ε Model (RKE)

Realizable k-ε is a first order turbulence model which employs two separate transport equations which independently determine the turbulent velocity and length scales. Results of the transport equations are used to evaluate a single turbulent viscosity term which is valid in all directions so k-ε is an isotropic turbulence model. The equation of turbulent kinetic energy is derived from exact equation and can be written as;

$$
\frac{\partial}{\partial t}(\rho k) + \frac{\partial}{\partial x_j}(\rho k u_j) =
$$

$$
= \frac{\partial}{\partial x_j}\left[\left(\mu + \frac{\mu_T}{\sigma_k}\right)\frac{\partial k}{\partial x_j}\right] + G_k - \rho\varepsilon - Y_M
$$

(2.14)

The model equation of dissipation rate (ε) at the standard k-ε model (SKE) was obtained empirically and does not resemble its mathematical counterpart. To improve the performance of the model, a new dissipation rate transport equation has been derived from the exact equation for the transport of the mean-square vorticity fluctuation. The transport equation of dissipation rate used at the RKE can be written as;

$$
\frac{\partial}{\partial t}(\rho\varepsilon) + \frac{\partial}{\partial x_j}(\rho\varepsilon u_j) =
$$

$$
= \frac{\partial}{\partial x_j}\left[\left(\mu + \frac{\mu_T}{\sigma_\varepsilon}\right)\frac{\partial\varepsilon}{\partial x_j}\right] + \rho C_1 S\varepsilon - \rho C_2 \frac{\varepsilon^2}{k + \sqrt{\nu\varepsilon}}
$$

(2.15)

The SKE uses a very simple equation of turbulent viscosity value which employs the terms representing density, turbulent velocity, dissipation rate. The following equation is evaluated for the turbulent viscosity value.

$$
\mu_T = \rho C_\mu \frac{k^2}{\varepsilon}
$$

(2.16)

In equation 2.16 C_μ is the constant coefficient with a value of 0.09. Because of the C_μ being constant so not flow dependent, SKE produces excessive kinetic energy in the areas of rapid and irrotational strain e.g. stagnation point on the leading edge of a turbine airfoil. To improve the turbulence model performance on such flow conditions a realizibility constraint is applied to the C_μ coefficient so it is no longer constant. Following equation set is employed to ensure that model satisfies certain mathematical constraints on the Reynolds stresses and also consistent with the physics of the turbulent flows;

$$C_\mu = \frac{1}{A_0 + A_s \dfrac{kU^*}{\varepsilon}}$$

$$U^* \equiv \sqrt{S_{ij}S_{ij} + \widetilde{\Omega}_{ij}\widetilde{\Omega}_{ij}}$$

$$\widetilde{\Omega}_{ij} = \Omega_{ij} - 2\varepsilon_{ijk}\omega_k \quad \text{and} \quad \Omega_{ij} = \overline{\Omega_{ij}} - \varepsilon_{ijk}\omega_k \qquad (2.17)$$

$$A_0 = 4.04 \quad , \quad A_s = \sqrt{6}\cos\phi \; , \quad \phi = \frac{1}{3}\cos^{-1}\left(\sqrt{6}W\right)$$

$$W = \frac{S_{ij}S_{jk}S_{ki}}{\widetilde{S}^3} \quad \text{and} \quad \widetilde{S} = \sqrt{S_{ij}S_{ij}}$$

In equation set 2.17 $\overline{\Omega_{ij}}$ is mean rate of rotation tensor viewed in a moving reference frame with the angular velocity ω_k and (S_{ij}) is the shear strain rate as mentioned in equation 2.4. The remaining equations and model constants of RKE are listed as follows.

Generation of turbulence kinetic energy due to mean velocity gradients has an exact equation as ;

$$G_k = -\rho\overline{u_i' u_j'}\frac{\partial u_j}{\partial x_i} \qquad (2.18)$$

Model equation of this term used in the transport equation of turbulent kinetic energy is consistent with the Boussinesq hypothesis;

$$G_k = \mu_T S^2 \text{ where } S \equiv \sqrt{2S_{ij}S_{ij}} \qquad (2.19)$$

Effect of compressibility on turbulence is modeled as;

$$Y_M = 2\rho\varepsilon M_t^2 \text{ where } M_t = \sqrt{\frac{k}{a^2}} \text{ and } a = \sqrt{\gamma RT} \qquad (2.20)$$

C_1 and C_2 at the transport equation of turbulent dissipation rate are established as;

$$C_1 = \max\left[0.43, \frac{\eta}{\eta + 5}\right] \text{ where } \eta = S\frac{k}{\varepsilon}$$

$$C_2 = 1.9 \qquad (2.21)$$

The turbulent Prandtl numbers for k and ε are established to ensure that model performs well. Their values are $\sigma_k = 1.0$ and $\sigma_\varepsilon = 1.2$.

In derivation of the k-ε model, the flow is assumed to be fully turbulent and the effects of the molecular viscosity are almost neglected. Therefore, this model is only valid for fully turbulent flows. However, the robustness, economy and the reasonable accuracy offered by the model for a wide range of turbulent flows make it very popular for industrial purposes.

2.2.5.3 Shear-Stress Transport k-ω Model (SST)

The Shear-Stress Transport k-ω model is developed to effectively combine the success of the k-ω in the near wall region and k-ε at the free stream by a blending function. In SST, a transformed form of k-ε model is added to the k-ω formulation after multiplying each turbulence model by the blending functions. Blending functions operate at several equations and work such that their value get close to one in the near-wall region so only k-ω part becomes active and zero away from the surface so only k-ε part becomes active. This feature makes the SST applicable to a wider class of flow problems. Similar to

RKE, SST is also a first-order, two-equation and isentropic turbulence model. The equations of turbulent kinetic energy and specific dissipation rate can be written as;

$$\frac{\partial}{\partial t}(\rho k) + \frac{\partial}{\partial x_i}(\rho k u_i) =$$

$$= \frac{\partial}{\partial x_j}\left(\Gamma_k \frac{\partial k}{\partial x_j}\right) + \widetilde{G}_k - Y_k \qquad (2.22)$$

$$\frac{\partial}{\partial t}(\rho \omega) + \frac{\partial}{\partial x_i}(\rho \omega u_i) =$$

$$= \frac{\partial}{\partial x_j}\left(\Gamma_\omega \frac{\partial \omega}{\partial x_j}\right) + G_\omega - Y_\omega + D_\omega \qquad (2.23)$$

In SST, effective diffusivities (Γ_k and Γ_ω) and turbulent viscosity(μ_T) all employ blending functions in their formulation and these terms are evaluated as follows;

$$\Gamma_k = \mu + \frac{\mu_T}{\sigma_k} \quad \text{and} \quad \Gamma_\omega = \mu + \frac{\mu_T}{\sigma_\omega} \qquad (2.24)$$

$$\mu_T = \frac{\rho k}{\omega}\frac{1}{\max\left[\dfrac{1}{\alpha^*},\dfrac{SF_2}{a_1\omega}\right]} \qquad (2.25)$$

The coefficient α^*, which damps the turbulent viscosity for low-Reynolds number flows, can be written as the following set of equations;

$$\alpha^* = \alpha_\infty^* \left(\frac{\alpha_0^* + \text{Re}_t / R_k}{1 + \text{Re}_t / R_k} \right) \qquad \text{where}$$

(2.26)

$$\text{Re}_t = \frac{\rho k}{\mu \omega} \text{ , } \alpha_0^* = \frac{\beta_i}{3} \text{ and } \beta_i = F_1 \beta_{i,1} + (1 - F_1) \beta_{i,2}$$

In the high-Reynolds number form $\alpha^* = \alpha_\infty^* = 1$. The turbulent Prandtl numbers for k and ω, which were specified as constant values at RKE and standard form of k-ω model, can be given by the following set of equations;

$$\sigma_k = \frac{1}{F_1 / \sigma_{k,1} + (1 - F_1) / \sigma_{k,2}}$$

(2.27)

$$\sigma_\omega = \frac{1}{F_1 / \sigma_{\omega,1} + (1 - F_1) / \sigma_{\omega,2}}$$

There are production and dissipation terms of turbulent kinetic energy and specific dissipation rate at both transport equations. Production term of turbulent kinetic energy can be written as;

$$\widetilde{G}_k = \min(G_k, 10 \rho \beta^* k \omega)$$

(2.28)

The exact and modeled form of G_k is given at equation 2.18 and 2.19 respectively. The production of specific dissipation rate is related with the $\widetilde{G}_k$ and it can be written as

$$G_\omega = \frac{\alpha}{\nu_T} \widetilde{G}_k$$

(2.29)

The coefficient α has a form similar to the coefficient which damps the turbulent viscosity at equation 2.26.

$$\alpha = \frac{\alpha_\infty}{\alpha^*}\left(\frac{\alpha_0 + \mathrm{Re}_t/R_\omega}{1 + \mathrm{Re}_t/R_\omega}\right) \qquad (2.30)$$

The constant α_∞ is also calculated with the help of blending functions. In the high-Reynolds number form $\alpha = \alpha_\infty = 1$.

$$\alpha_\infty = F_1\alpha_{\infty,1} + (1 - F_1)\alpha_{\infty,2} \quad \text{where}$$

$$\alpha_{\infty,1} = \frac{\beta_{i,1}}{\beta_\infty^*} - \frac{\kappa^2}{\sigma_{\omega,1}\sqrt{\beta_\infty^*}} \qquad (2.31)$$

$$\alpha_{\infty,2} = \frac{\beta_{i,2}}{\beta_\infty^*} - \frac{\kappa^2}{\sigma_{\omega,2}\sqrt{\beta_\infty^*}}$$

The dissipation term of turbulent kinetic energy (Y_k) can be defined as;

$$Y_k = \rho\beta^* k\omega \qquad (2.32)$$

The coefficient β^* can be given by;

$$\beta^* = \beta_i^*\left[1 + \zeta^* F(M_t)\right] \quad \text{where}$$

$$\beta_i^* = \beta_\infty^*\left(\frac{4/15 + (\mathrm{Re}_t/R_\beta)^4}{1 + (\mathrm{Re}_t/R_\beta)^4}\right) \qquad (2.33)$$

The dissipation term of specific dissipation rate (Y_ω) can be defined as;

$$Y_\omega = \rho\beta\omega^2 \qquad (2.34)$$

The coefficient β has a similar relation with β^*;

$$\beta = \beta_i\left[1 - \frac{\beta_i^*}{\beta_i}\zeta^* F(M_t)\right] \qquad (2.35)$$

The coefficient β_i^* and β_i has been presented at equation sets 2.33 and 2.26 respectively. The compressibility function ($F(M_t)$), which used in dissipation terms of turbulent kinetic energy and specific dissipation rate, can be given by;

$$F(M_t) = 0 \ \text{if} \ M_t \leq M_{t0}$$

$$F(M_t) = M_t^2 - M_{t0}^2 \ \text{if} \ M_t > M_{t0}$$

$$M_t^2 \equiv \frac{2k}{a^2}$$

(2.36)

In the equation 2.36, a is speed of sound as formulated in equation set 2.20. For high-Reynolds number flows $\beta_i^* = \beta_\infty^*$ and for incompressible flows $\beta^* = \beta_i^*$. Cross-diffusion term comes out from the transformation of the k-ε equations to the k-ω equations and placed in the transport equation of specific dissipation rate. This term is nested with the first blending function that it consists first blending function in its formulation and positive portion of cross-diffusion term is employed in the first blending function. The cross-diffusion term can be written as;

$$D_\omega = 2(1 - F_1)\rho \frac{1}{\omega \sigma_{\omega,2}} \frac{\partial k}{\partial x_j} \frac{\partial \omega}{\partial x_j}$$

(2.37)

Remaining coefficients established to ensure that model performs well. Their values are; $a_1 = 0.31$, $\alpha_\infty^* = 1$, $\alpha_0 = \frac{1}{9}$, $R_k = 6$, $R_w = 2.95$, $R_\beta = 8$, $\beta_\infty^* = 0.09$, $\beta_{i,1} = 0.075$, $\beta_{i,2} = 0.0828$, $\kappa = 0.41$, $\zeta = 1.5$, $M_{t0} = 0.25$ $\sigma_{k,1} = 1.176$, $\sigma_{k,2} = 1$, $\sigma_{w,1} = 2$, $\sigma_{w,2} = 1.168$.

Finally, the blending functions used in the SST formulation can be given as the following set of equations;

$$F_1 = \tanh\left(\Phi_1^4\right)$$

$$\Phi_1 = \min\left[\max\left(\frac{\sqrt{k}}{0.09\omega y}, \frac{500\mu}{\rho y^2 \omega}\right), \frac{4\rho k}{\sigma_{\omega,2} D_\omega^+ y^2}\right]$$

$$D_\omega^+ = \max\left[2\rho\frac{1}{\sigma_{\omega,2}}\frac{1}{\omega}\frac{\partial k}{\partial x_j}\frac{\partial \omega}{\partial x_j}, 10^{-10}\right] \qquad (2.38)$$

$$F_2 = \tanh\left(\Phi_2^2\right)$$

$$\Phi_2 = \max\left(\frac{\sqrt{k}}{0.09\omega y}, \frac{500\mu}{\rho y^2 \omega}\right)$$

In equation set 2.38 y is the distance to the next surface and D_ω^+ is the positive portion of the cross-diffusion term as mentioned before.

SST is not as robust as RKE however, it is provides similar economical advantages and reasonable accuracy for a wider range of flows so it is also very popular in industrial applications.

2.2.5.4 Reynolds Stress Model (RSM)

Reynolds Stress Model is a second-order RANS turbulence model. This turbulence model solves transport equations of the Reynolds Stresses together with a dissipation rate equation. This means there will be seven additional transport equations are required for three-dimensional flows. The anisotropic characteristics of RSM provides greater potential with respect to RKE and SST in terms of accurate prediction of complex flows however, fidelity of RSM predictions are still relies on closure assumptions applied to model various terms in the exact term of transport equations of the Reynolds stresses. Moreover, RSM results might not be superior to the isotropic turbulence models in all flow cases. The general form of the equations for the transport of Reynolds stresses is given in equation 2.39. Modeling of pressure strain and dissipation rate is particularly effective on the accuracy of RSM predictions.

$$\frac{\partial}{\partial t}\left(\rho \overline{u_i' u_j'}\right) + C_{ij} = D_{T,ij} + D_{L,ij} + P_{ij} + \phi_{ij} + \varepsilon_{ij} \qquad (2.39)$$

Among the various terms in the transport equation of Reynolds stresses, convection (C_{ij}), molecular diffusion ($D_{L,ij}$) and stress production (P_{ij}) terms do not require any modeling. Their exact equations can be given by;

$$C_{ij} = \frac{\partial}{\partial x_k}\left(\rho u_k \overline{u_i' u_j'}\right)$$

$$D_{L,ij} = \frac{\partial}{\partial x_k}\left[\mu \frac{\partial}{\partial x_k}\left(\overline{u_i' u_j'}\right)\right] \qquad (2.40)$$

$$P_{ij} = -\rho\left(\overline{u_i' u_k'} \frac{\partial u_j}{\partial x_k} + \overline{u_j' u_k'} \frac{\partial u_i}{\partial x_k}\right)$$

Rest of the terms need to be modeled. Following equations are presenting the exact equations of the remaining terms and describing the modeling assumptions required to close the equation set. Exact equation of turbulent diffusion ($D_{T,ij}$) can be given by;

$$D_{T,ij} = -\frac{\partial}{\partial x_k}\left[\rho \overline{u_i' u_j' u_k'} + \overline{p\left(\delta_{kj} u_i' + \delta_{ik} u_j'\right)}\right] \qquad (2.41)$$

Equation 2.41 has been modeled by using a scalar turbulent diffusivity as follows;

$$D_{T,ij} = \frac{\partial}{\partial x_k}\left(\frac{\mu_T}{\sigma_k} \frac{\partial \overline{u_i' u_j'}}{\partial x_k}\right) \qquad (2.42)$$

Pressure-strain term (ϕ_{ij}) has an exact definition as follows;

$$\phi_{ij} = p\left(\frac{\partial u_i'}{\partial x_j} + \frac{\partial u_j'}{\partial x_i}\right)$$

(2.43)

For the pressure-strain term low-Re stress-omega model is selected which is ideal for flows over curved surfaces and swirling flows. The closure equations are similar to the k-ω model and can be listed as follows;

$$\phi_{ij} = \phi_{ij,1} + \phi_{ij,2}$$

(2.44)

where first term of the decomposition ($\phi_{ij,1}$) counts for the slow pressure-strain term, also known as return-to-isotropy term, second term ($\phi_{ij,2}$) counts for the rapid pressure-strain term. The pressure-strain term can be modeled as;

$$\phi_{ij} = -C_1 \rho \beta^*_{RSM} \omega \left[\overline{u_i' u_j'} - 2/3\delta_{ij}k\right] - \hat{\alpha}_0 \left[P_{ij} - 1/3 P_{kk}\delta_{ij}\right]$$

$$- \hat{\beta}_0 \left[D_{ij} - 1/3 P_{kk}\delta_{ij}\right] - k\hat{\gamma}_0 \left[S_{ij} - 1/3 S_{kk}\delta_{ij}\right] \text{ where}$$

$$D_{ij} = -\rho\left[\overline{u_i' u_m'}\frac{\partial u_m}{\partial x_j} + \overline{u_j' u_m'}\frac{\partial u_m}{\partial x_i}\right] \text{ and}$$

(2.45)

$$\beta^*_{RSM} = \beta^* f_{\beta^*}$$

The β^* has been presented at the equation sets 2.33 and 2.36. The f_{β^*} is defined in the same way as for the standard k-ω model

$$f_{\beta^*} = 1 \text{ if } \chi_k \leq 0$$

$$f_{\beta^*} = \frac{1 + 640\chi_k^2}{1 + 400\chi_k^2} \text{ if } \chi_k > 0 \qquad \text{where}$$

(2.46)

$$\chi_k \equiv \frac{1}{\omega^3}\frac{\partial k}{\partial x_j}\frac{\partial \omega}{\partial x_j}$$

The constants in the above equations can be given as follows;

$$\hat{\alpha}_0 = \frac{8 + C_2}{11}$$

$$\hat{\beta}_0 = \frac{8C_2 - 2}{11}$$ (2.47)

$$\hat{\gamma}_0 = \frac{60C_2 - 4}{55}$$

Inclusion of viscous damping can improve the flow predictions. For this following changes should be conducted;

$$\hat{\alpha} = \frac{1 + \hat{\alpha}_0 \, \mathrm{Re}_t / R_k}{1 + \mathrm{Re}_t / R_k}$$

$$\hat{\beta} = \hat{\beta}_0 \frac{\mathrm{Re}_t / R_k}{1 + \mathrm{Re}_t / R_k}$$ (2.48)

$$\hat{\gamma} = \hat{\gamma}_0 \frac{0.007 + \mathrm{Re}_t / R_k}{1 + \mathrm{Re}_t / R_k}$$

Without viscous damping function C_1 value of equation set 2.45 equals to 1.8. It is evaluated as follows with the viscous damping function;

$$C_1 = 1.8 \left[\frac{5/3 + \mathrm{Re}_t / R_k}{1 + \mathrm{Re}_t / R_k} \right]$$ (2.49)

The terms $\hat{\alpha}_0$, $\hat{\beta}_0$, $\hat{\gamma}_0$ in the equation set 2.45 should be replaced with the $\hat{\alpha}$, $\hat{\beta}$, $\hat{\gamma}$ terms given at equation set 2.48 to get viscous damping effective.

When turbulence kinetic energy is needed for modeling any term it is obtained by taking the race of Reynolds stress tensor as follows;

$$k = \frac{1}{2} \overline{u'_i u'_i}$$ (2.50)

In order to obtain boundary conditions for the Reynolds stresses a transport equation of turbulence kinetic energy identical to equation 2.14 is solved. This equation can be given as follows;

$$\frac{\partial}{\partial t}(\rho k) + \frac{\partial}{\partial x_j}(\rho k u_j) =$$

$$= \frac{\partial}{\partial x_j}\left[\left(\mu + \frac{\mu_T}{\sigma_k}\right)\frac{\partial k}{\partial x_j}\right] + \frac{1}{2}P_{ii} - \rho\varepsilon\left(1 + 2M_t^2\right)$$

(2.51)

It should be noted that in equations 2.42 and 2.51 σ_k is equal to 0.82 instead of 1. The calculation of M_t^2 has been given in equation set 2.36. The dissipation tensor (ε_{ij}), which is the last term of the transport equation of the Reynolds stresses has the exact definition as follows;

$$\varepsilon_{ij} = -2\mu\overline{\frac{\partial u_i'}{\partial x_k}\frac{\partial u_j'}{\partial x_k}}$$

(2.52)

The dissipation tensor is modeled as follows when it is coupled with omega (ω) equation;

$$\varepsilon_{ij} = 2/3\delta_{ij}\rho\beta_{RSM}^* k\omega$$

(2.53)

The β_{RSM}^* is evaluated as defined at the equations above and the specific dissipation rate is calculated by transport equation of the standard k-ω model which is given by;

$$\frac{\partial}{\partial t}(\rho\omega) + \frac{\partial}{\partial x_i}(\rho\omega u_i) =$$

$$= \frac{\partial}{\partial x_j}\left(\Gamma_\omega \frac{\partial \omega}{\partial x_j}\right) + G_\omega - Y_\omega$$

(2.54)

In fact this equation is identical to equation 2.23 with minor changes like there is no cross-diffusion term (D_w) and turbulent Prandtl numbers for k and ω (σ_k and σ_ω) are constants. The turbulent viscosity is computed similarly to standard k-ε model as given in equation 2.16. Remaining coefficients established to ensure that model performs well. Their values are; $\alpha_\infty^* = 1$, $\alpha_0 = \frac{1}{9}$, $\alpha_\infty = 0.52$, $C_2 = 0.52$, $R_k = 12$, $R_w = 6.2$, $R_\beta = 12$, $\beta_\infty^* = 0.09$, $\beta_i = 0.072$, $\zeta = 1.5$, $M_{t0} = 0.25$, $\sigma_w=2$.

Analyses conducted with RSM demands higher computational power and more time for each iteration. Moreover, analyses are not robust because of the high coupling between the momentum equations and Reynolds stresses. Therefore, RSM is not frequently preferred in industrial purposes unless problem consists of high anisotropy like highly swirling flows or stress-induced secondary flows in ducts.

2.2.5.5 V2-f Turbulence Model (V2-f)

V2-f is a four equation, first-order RANS based turbulence model in which the transport equations of turbulence kinetic energy (k), turbulence dissipation rate (ε), velocity variance scale ($\overline{v^2}$) and elliptic relaxation function (f) are solved and an alternative eddy viscosity formulation is used. The first introduction of V2-f model arises from observations of Durbin [65] upon the shear-stress in a fully developed channel flow. Durbin pointed out that Reynolds stress component ($\overline{uv}$) is not correctly modelled by the velocity scale ($k^{1/2}$) employed in standard k-ε model because of its low damping in the vicinity of the solid walls ($k \sim y^2$). Besides, it is also demonstrated that velocity fluctuation normal to the streamlines has a higher damping at the same region ($\overline{v^2} \sim y^4$).

Findings can be interpreted that, if somehow distribution of $\overline{v^2}$ is obtained and employed in the eddy viscosity formulation we can get a very good estimate of shear stress especially in the important near-wall region. In order to apply the

ideas emerged from the channel flow case to more complex geometries, a new transport equation for an imaginary stress component that is always normal to the closest wall ($\overline{v^2}$) is introduced. Besides, an elliptic transport equation is also introduced to have the near wall properties on the imaginary stress component properly. V2-f has somewhat anisotropic features by making use of a second velocity scale operating at wall-normal direction and advantageous over other first-order RANS turbulence models. Therefore, during the last few years, V2-f has become increasingly popular. Several modifications to the original model have been proposed by researchers and besides vast number of validation studies been conducted.

2.2.5.5.1. Equations of V2-f and Model Constants

V2-f model simply extends the standard k-ε model to low-Re number flow regions by incorporating near-wall turbulence anisotropy while retaining the Boussinesq approximation. This is realized by modifying eddy viscosity formulation and solving two additional partial differential equations. Consequently, V2-f model requires solving standard k-ε model equations together with the transport equation of the turbulent intensity normal to the streamlines and an elliptic relaxation equation. For convenience, notations frequently used in literature to describe V2-f model are employed at the following equations. A slightly careful examination will realize that in fact equations 2.14 and 2.55 are identical. Turbulence kinetic energy equation for V2-f model can be given as follows;

$$\frac{\partial}{\partial t}\left(\rho k\right) + \frac{\partial}{\partial x_i}\left(\rho k u_i\right) =$$

$$= P_k - \rho\varepsilon + \frac{\partial}{\partial x_j}\left[\left(\mu + \frac{\mu_T}{\sigma_k}\right)\frac{\partial k}{\partial x_j}\right]$$

(2.55)

Turbulence dissipation rate equation is given by;

$$\frac{\partial}{\partial t}(\rho \varepsilon) + \frac{\partial}{\partial x_i}(\rho \varepsilon\, u_i) =$$

$$= \frac{C_{\varepsilon 1}P_k - C_{\varepsilon 2}\rho\varepsilon}{T} + \frac{\partial}{\partial x_j}\left[\left(\mu + \frac{\mu_T}{\sigma_\varepsilon}\right)\frac{\partial \varepsilon}{\partial x_j}\right] \qquad (2.56)$$

Reynolds stress transport equation with boundary condition simplifications is used as the starting point for derivation of $\overline{v^2}$ model equation. In the first introduced version, Durbin [66] proposed the following transport equation to model the imaginary stress component normal to the wall.

$$\frac{\partial}{\partial t}\left(\rho\, \overline{v^2}\right) + \frac{\partial}{\partial x_i}\left(\rho\, \overline{v^2} u_i\right) =$$

$$= \rho k f - \frac{\varepsilon}{k}\rho\overline{v^2} + \frac{\partial}{\partial x_j}\left[(\mu + \mu_T)\frac{\partial \overline{v^2}}{\partial x_j}\right] \qquad (2.57)$$

The first term in the right hand side of equation 2.57 is the modelled effect of pressure strain and it is controlled by elliptic relaxation function. It should be noted that pressure in a fluid flow is in elliptic nature and so correlation of fluctuating variables, and so is pressure-strain, are also elliptic. Therefore, f is governed by a modified Helmholtz equation of elliptic nature;

$$f - L^2 \frac{\partial^2 f}{\partial x_j^2} =$$

$$= \frac{C_1}{T}\left(\frac{2}{3} - \frac{\overline{v^2}}{k}\right) + C_2 \frac{P_k}{\rho k} - \frac{1}{T}\left(\frac{2}{3} - \frac{\overline{v^2}}{k}\right) \qquad (2.58)$$

The first and second terms in the left hand side of equation 2.58 can be interpreted as slow and rapid pressure-strain terms similar to RSM model and last term ensures the correct farfield behaviour of the equation. Remaining equations of the original V2-f model are as follows;

$$P_k = 2\mu_T S^2 \quad \text{where} \quad S^2 \equiv S_{ij}S_{ij}$$

$$C_{\varepsilon 1} = 1.3 + 0.25 / \left[1 + (C_L d / 2L)^2 \right]^4$$

(2.59)

Where d is the wall distance and S_{ij} is the shear strain rate which is given at equation 2.4.

The turbulent viscosity is evaluated by employing the imaginary stress component in the formulation;

$$\mu_T = \rho C_\mu \overline{v^2} T$$

(2.60)

Time scale constraint is also used in turbulent viscosity evaluation because most of the eddy-viscosity models overpredict the turbulence kinetic energy, especially at stagnation points. The limits expressed in Kolmogorov variables are applied to the time and length scales as realizibility constraints in order to avoid this overprediction. Durbin [67] suggested the following constraint can be used to derive a bound on turbulent time scale;

$$2k \geq \overline{v^2} \geq 0$$

(2.61)

This constraint is imposed by finding the eigenvectors of the strain tensor and rotating the strain tensor so that it becomes diagonal with the eigenvectors which is the worst case. Then for V2-f model time scale becomes;

$$T = \min \left(\max \left(\frac{k}{\varepsilon}, 6\sqrt{\frac{v}{\varepsilon}} \right), \frac{k}{3C_\mu \overline{v^2}} \frac{1}{\max \lambda_\alpha} \right)$$

(2.62)

In equation 2.62, $\max \lambda_\alpha$ is the largest eigenvalue of strain rate tensor. The realizibility constraint presented in equation 2.62 was modified by Lien&Kalitzin [68] through adding model constant $C_{\lim}$ to allow for tuning against experiments. Use of time scale constraint significantly improves the turbulence kinetic energy predictions.

$$T' = \max\left(\frac{k}{\varepsilon}, 6\sqrt{\frac{\nu}{\varepsilon}} \right)$$

$$T = \min\left(T', \frac{C_{\lim}k}{\sqrt{6}\,\overline{v^2}\,C_\mu\sqrt{S^2}} \right) \tag{2.63}$$

In addition to the time scale constraint (T), a similar constraint on the turbulent length scale (L), which is only effective in elliptic relaxation function, is also proposed by Lien&Kalitzin [68].

$$L' = \min\left(\frac{k^{3/2}}{\varepsilon}, \frac{k^{3/2}}{\sqrt{6}\,\overline{v^2}\,C_\mu\sqrt{S^2}} \right)$$

$$L = C_L \max\left(L', C_\eta\left(\frac{\nu^3}{\varepsilon} \right)^{1/4} \right) \tag{2.64}$$

The boundary conditions which enforce the correct near wall behavior can be given as follows;

$$k_w = 0 \quad \text{and} \quad \overline{v_w^2} = 0$$

$$\varepsilon_w = 2\nu\frac{k_1}{y_1^2} \quad \text{and} \quad f_w = -\frac{20\nu^2\,\overline{v_1^2}}{\varepsilon_w y_1^4} \tag{2.65}$$

In equation 2.65 indices w and 1 denote the wall and first point above the wall. The boundary conditions of turbulence kinetic energy and velocity variance scale come out from no-slip boundary condition for wall. Wall boundary condition of turbulence dissipation rate is derived from simplifying the Taylor expansion of fluctuating velocities by neglecting high-order terms and employing no-slip and continuity concepts. The wall boundary condition of elliptic relaxation function is derived by studying velocity variance transport equation but in fact velocity variance is equal to zero at wall because of the no-slip boundary condition. Therefore, equation 2.57 is re-written at a small distance from wall

and f is assumed to be constant until wall. Same assumption has been also used for ε because once again k is equal to zero at wall because of the no-slip boundary condition.

After Durbin [65] proposed V2-f model many researchers suggested modifications and calibrated constants related with the new formulations. The modification offered by Parneix&Durbin [69] aimed to eliminate the wall distance (d) which is present in equation 2.57. In this version $C_{\varepsilon 1}$ has been defined with $k/\overline{v^2}$ ratio and a new set of constants has been used.

$$C_{\varepsilon 1} = C'_{\varepsilon 1}\left(1 + C_{\varepsilon d}\sqrt{k/\overline{v^2}}\right)$$

(2.66)

The V2-f model version of Parneix&Durbin [69] uses same realizibility constraints with the original model. An additional modification applied to the V2-f aimed to make the model suitable for segregated solvers. The original version suffers from being numerically unstable because of the strong coupling of f, $\overline{v^2}$ and ε in the f boundary condition (equation 2.65). Lien&Kalitzin [68] suggested a modification to the transport equations so that f boundary condition becomes much more numerically compatible. Operation consists of adding a new source term to f equation and subtracting a similar term from $\overline{v^2}$. This solution maintains the near-wall variable dependence of $\overline{v^2}$ which is $\overline{v^2} \sim y^4$ and gives exactly the same farfield results with the $\overline{v^2}$ equation in the original model. The only difference is that the elliptic relaxation function has been offset in the whole flow region so that boundary condition becomes $f_w = 0$. The transport equations of $\overline{v^2}$ and f become;

$$\frac{\partial}{\partial t}\left(\rho\,\overline{v^2}\right) + \frac{\partial}{\partial x_i}\left(\rho\,\overline{v^2}u_i\right) =$$

$$= \rho k f - \frac{\varepsilon}{k}\rho\overline{v^2} + \frac{\partial}{\partial x_j}\left[(\mu + \mu_T)\frac{\partial\overline{v^2}}{\partial x_j}\right] - \frac{5\varepsilon}{k}\rho\overline{v^2}$$

(2.67)

$$f - L^2 \frac{\partial^2 f}{\partial x_j^2} =$$

$$= \frac{C_1}{T}\left(\frac{2}{3} - \frac{\overline{v^2}}{k}\right) + C_2 \frac{P_k}{\rho k} - \frac{1}{T}\left(\frac{2}{3} - \frac{\overline{v^2}}{k}\right) + 5\frac{\overline{v^2}}{kT} \qquad (2.68)$$

The ratio k/ε appearing in the new f equation is replaced with time scale T. The table below summarizes the model constants employed in the aforementioned models.

Table 2.1. V2-f model constants

	Durbin[65] (original)	Parneix&Durbin[69]	Lien&Kalitzin[68]
C_μ	0.19	0.22	0.22
$C_{\varepsilon 1}$	Wall distance	Linear relation	Linear relation
$C'_{\varepsilon 1}$	-	1.4	1.4
$C_{\varepsilon d}$	-	0.045	0.050
$C_{\varepsilon 2}$	1.9	1.9	1.9
C_1	1.4	1.4	1.4
C_2	0.3	0.3	0.3
$C_{\lim}$	0.6	0.6	0.6
C_L	0.30	0.25	0.23
C_η	70	85	70
σ_k	1	1	1
σ_ε	1.3	1.3	1.3

Modifications suggested by Lien&Kalitzin [68] are very effective on the stability of the computations so they are widely used in commercial codes. For instance, NUMECA software directly uses the above formulation of the

Lien&Kalitzin [68] version of V2-f model whereas FLUENT software employs the same formulation with a small difference such that in FLUENT version of V2-f model, $C_{\varepsilon d}$ is set equal to 0.045.

The latest suggestions to the V2-f model in the literature were about physical limitation of the wall normal stress ($\overline{v^2}$). Davidson et al. [70] reminded the fact that $\overline{v^2}$ should be the smallest normal stress because its source term kf is dampened by wall. Then following relation should be correct;

$$\text{If } \overline{v^2} \leq \overline{u^2} \text{ and } \overline{v^2} \leq \overline{\omega^2} \text{ and}$$

$$k = \frac{1}{2}\left(\overline{u^2} + \overline{v^2} + \overline{\omega^2}\right) \text{ then}$$

$$\overline{v^2} \leq \frac{2}{3}k$$

(2.69)

In homogeneous region away from the wall, Lien&Kalitzin [68] assumed that the elliptic operator ($\partial^2 f / \partial x_j^2$) is negligible. It turns out that this assumption is not true because Davidson et al. [70] conducted analysis with the Lien&Kalitzin [68] version of V2-f model on fully developed channel flow and revealed that model predicts $\overline{v^2}$ values higher than $2k/3$ away from the wall. The elliptic operator in fact significantly contributes to the source term, kf in the $\overline{v^2}$ equation, and as a consequence non-physical overprediction of $\overline{v^2}$ occurs. Davidson et al. [70] set an upper bound to the source term (kf) of $\overline{v^2}$ equation to eliminate these unreasonable $\overline{v^2}$ predictions;

$$\overline{v^2_{source}} = \min\left\{ kf, \frac{C_1 k}{T}\left(\frac{2}{3} - \frac{\overline{v^2}}{k}\right) + C_2\frac{P_k}{\rho} \right. $$
$$\left. -\frac{k}{T}\left(\frac{2}{3} - \frac{\overline{v^2}}{k}\right) + 5\frac{\overline{v^2}}{T} \right\}$$

(2.70)

Equation 2.70 ensures that $\overline{v^2}$ value stay below the $2k/3$ value however, in regions where $\overline{v^2} \cong 2/3\,k$ V2-f model predicts very large turbulent viscosities. Remember that high turbulent viscosity values predicted by SKE are caused from using a constant C_μ value in the turbulent viscosity formulation and RKE was the solution of the problem. Similarly V2-f has a constant C_μ with a much larger value. Therefore, in the regions where $\overline{v^2}$ value becomes closer to $2k/3$, V2-f predicts the turbulent viscosity even higher from SKE. The simple precaution taken for this situation can be given as follows;

$$\mu_T = \min \left\{ \rho C_{\mu,SKE}\, k^2 / \varepsilon, \rho C_{\mu,V2-f}\, \overline{v^2}T \right\} \quad \text{where}$$
$$C_{\mu,SKE} = 0.09 \quad \text{and} \quad C_{\mu,V2-f} = 0.22 \tag{2.71}$$

The Davidson et al. [70] studied the Lien&Kalitzin [68] version of the V2-f model so same constants have been used including C_μ value in equation 2.71. The relations 2.70 and 2.71 is used together on fully developed channel flow and 3D wall jet by Davidson et al. [70] and compared with Lien&Kalitzin [68] version of the V2-f model. It is observed that in both analyses the modification works very well and predictions improve. The final modification in the literature is once again suggested by Davidson et al [70] to the Lien&Kalitzin [68] version of the V2-f model. Second modification suggested by Davidson et al. [70] is composed around a very simple idea such that, unlike other first-order RANS based turbulence models, in V2-f model transport equation of two velocity scales $(k, \overline{v^2})$ are available. Therefore, V2-f model can be modified so that, one turbulent viscosity computed with $\overline{v^2}$ is used for turbulent diffusion in the wall normal direction and other turbulent viscosity computed with k is used for turbulent diffusion in the wall parallel directions. Equations for turbulent viscosities are given by;

$$\mu_{T,\perp} = 0.22\overline{v^2}T \quad \text{and} \quad \mu_{T,\parallel} = 0.09kT \tag{2.72}$$

Above modification is also implemented to the Lien&Kalitzin version of the V2-f model and it was found to give only a small improvement for 3D wall jet. Realizibility constraints suggested for in V2-f model are examined by Sveningsson [71]. It was concluded that realizibility constraint used for turbulent length scale is less effective than the constraint used for turbulent time scale on the results. Moreover, three different values of model constant $C_{\lim}$ have been investigated. Values of 1 and ∞ (no constraint) have given almost identical results. When the $C_{\lim}$ value was equal to 0.6, predictions were the closest to experimental data and hardly distinguishable from FLUENT V2-f model solutions. It should be noted that Sveningsson [71] used a V2-f model version implementing a non-zero f wall boundary condition (similar to Parneix&Durbin [69]), which is numerically unstable, and acquired very similar results with FLUENT V2-f model (similar to Lien&Kalitzin [68]), which is numerically stable. This indicates that only effect of reformulation conducted by Lien&Kalitzin [68] on the V2-f model is the desired effect of making the solution more stable.

2.2.5.5.2. Literature Review of V2-f Model Validations

V2-f model has gone through several validation and comparison studies after it has been first suggested by Durbin [65]. Iaccarino [72] and El-Behery et al. [73] investigated the planar asymmetric diffuser by V2-f model. Iaccarino [72] carried out numerical simulations with three commercial CFD codes: CFX, FLUENT, and Star-CD. A low-Re k-ε model with damping functions and the four-equation V2-f model have been used. The V2-f model predictions agree very well with the experiments both for the mean velocity and the turbulent kinetic energy. The three codes employed showed very similar characteristics in terms of convergence and accuracy; in particular the results obtained using the V2-f are consistent in all the codes. El-Behery et al. [73] studied on the same test case and compared six turbulence models (standard k-ω, SKE, low-Re k-ε, SST, RSM and V2-f). Results reveal that the closest predictions are acquired with V2-f model besides RSM, standard k-ω and SST provided accurate results. Tieszen et al. [74] and Choi et al. [75] examined the success of V2-f model at natural

convection analyses. Tieszen et al [74] made computations on flat plate and box with hot and cold walls and results showed that V2-f model predictions are at least as good as k-ε model. Choi et al. [75] studied on natural convection in a rectangular cavity with a two-layer turbulence model and two versions of V2-f model. One of the V2-f models was the original model and other was one of the numerically stable versions. Results showed that both versions of the V2-f model performs much better than the two-layer turbulence model. Besides, predictions of the original V2-f model were more accurate compared to the numerically stable version. Forced convection dominant flow in a strongly heated vertical tube is examined by Spall et al. [76]. V2-f model results are compared with the k-ω model for a low-Mach number gas flowing upward. Comparisons revealed that V2-f model performs quite well in forced convection dominant predictions and better than k-ω model. Smirnow [77] studied on flow and heat transfer over a backward-facing step. The V2-f model tested against experimental data, DNS results and two versions of k-ω (standard and low-Re) model. Friction coefficient results were well predicted by all turbulence models and low-Re version of the k-ω provided the best agreement with the experimental data. In fact, V2-f model gave the worst friction coefficient predictions and highly over estimated the Stanton number at heat transfer analyses. Kalitzin [78, 79, 80] investigated on transonic flow with various versions of V2-f model. Kalitzin [78] implemented Spalart-Allmaras model and V2-f model to a 3D ONERA M2 wing and results show that investigated turbulence models provided every similar predictions so Spalart-Allmaras model should be preferred for less overall computational cost. In continuing study Kalitzin [79] expanded the investigation of transonic flows and studied on three multi-element airfoils with three different versions of V2-f model, SST and Spalart-Allmaras model. Results showed that in majority of the computations Spalart-Allmaras and SST have better predictions than V2-f model. Among the V2-f model versions the first version which uses the wall distance (d) to evaluate the $C_{\varepsilon 1}$ value provides the closest agreement with the other turbulence models and experimental data and the second and third versions which use $k/\sqrt{v^2}$ ratio to evaluate $C_{\varepsilon 1}$ overestimate the friction coefficient values. In the latest validation study of Kalitzin [80] transonic bump geometry has been studied. Two different versions of the V2-f, first one uses the wall

distance (d) and second one uses $k/\overline{v^2}$ ratio to evaluate the $C_{\varepsilon1}$, have been studied. Results were parallel with the previous studies of Kalitzin [78,79] such that first version provides better agreement with the experimental data and second version overestimates the friction coefficient. The most comprehensive studies have been conducted by Cokljat et al. [81] and Zhang et al. [82] in terms of validation case diversity and compared turbulence models with V2-f model. Cokljat et al. [81] studied on six different test cases and analyses conducted by turbulence models based on k-ω and k-ε models have been compared with the FLUENT version of V2-f model. Test cases can be listed as two-dimensional channel flow, backward-facing step, wavy channel, planar asymmetric diffuser, axisymmetric afterbody and flow in a U-duct. Results showed that for two-dimensional channel flow and planar asymmetric diffuser V2-f model is undisputedly superior to other turbulence models. For backward-facing step and wavy channel cases V2-f results are quite accurate but not the best at every region of the flow. Finally for axisymmetric afterbody and U-duct cases although, V2-f results provided reasonable predictions, SST provided the best results for axisymmetric after body and RKE provided the most accurate results for U-duct. These mentioned results indicates that while success of two-equation turbulence models varies unpredictably, V2-f model performs quite consistently over various test cases considered. Zhang et al. [82] investigated the indoor flows such that forced convection in a room with partitions, mixed convection in a square cavity and natural convection with large temperature gradient in a model fire room. Various turbulence models which have different level of complexity (LES, V2-f, SST, RNG k-ε and 0-eqn) have been employed to solve these cases. The employed V2-f model version was the first modification of Davidson et al. [70]. Results showed that while LES provides most detailed information about the flow, its accuracy may not be the best especially at the near wall regions because of the algebraic model employed for subgrid scales. The V2-f model has provided the overall best performance in this study.

CHAPTER 3

DESCRIPTION of VALIDATION CASES

This chapter represents the experimental test cases numerically simulated for the validation purposes. In the first two cases, which are two-dimensional u-duct and periodic rib configuration in a straight channel, only the flow properties have been examined. In the third and fourth validation cases, which are flow in a trapezoidal smooth two-pass channel and rib turbulated two-pass channel, heat transfer quantities are also considered. In the last validation case, conjugate heat transfer is investigated on a turbine blade cooled with radial cooling channels.

3.1   Experimental Setups and Boundary Conditions

3.1.1   Two-Dimensional Strongly Curved Flow in a U-Duct

The first test case is chosen to investigate the ability of turbulence models to predict the strong streamline curvature because flow in a modern cooling scheme experiences multiple U-bend events. Therefore, experimental study of Monson et al. [13], the low speed internal flow (M=0.1) in a strongly curved U-duct, has been analysed. Although, flow problem in the U-duct looks simple it includes strong acceleration, separation and reattachment which can be challenging for the turbulence models. To minimize the wall effects and have a nominally two-dimensional flow data, high aspect ratio geometry has been used and sidewall boundary layer suction has been employed. Therefore, mid-pitch of the channel is modelled with a two-dimensional computational domain. The

channel height (H) is 38.1 mm and equal to the radius (from channel centerline) of the turn. A view of the computational domain together with sections at which experimental data and numerical simulation results will be presented is given in the following figure.
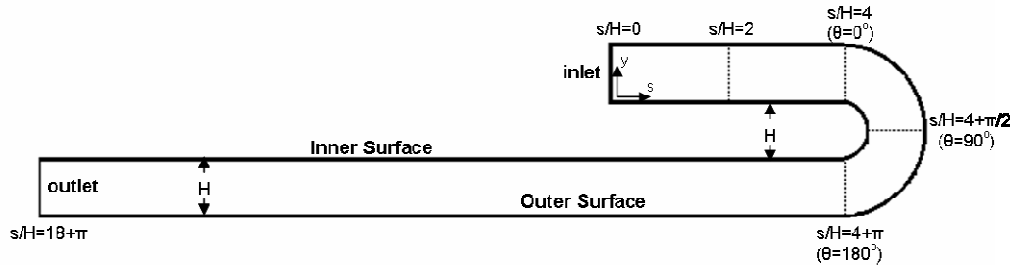
Figure 3.1. Computational domain for U-duct simulation

The tests were conducted at one low and one high Reynolds number values (10^5 and 10^6) based on channel height and mean velocity (30.1 m/s and 31.1 m/s respectively). Velocity inlet boundary condition is used as inlet boundary condition in the simulations. Experimental data presented for s/H=0 location have been used as profiles for velocity (in both directions) and turbulent kinetic energy. These profiles are shown in the following figures;

(a) (b)
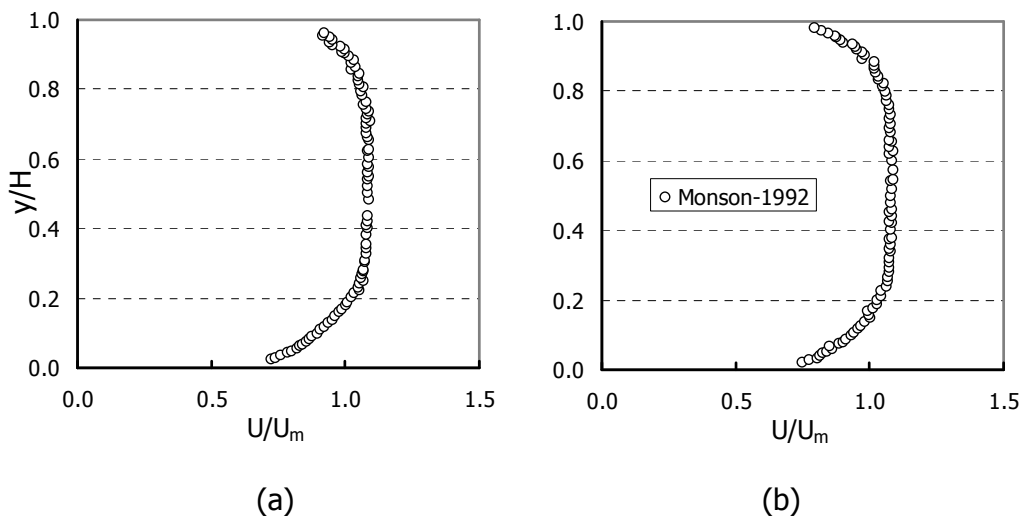
Figure 3.2. Longitudinal mean velocity (a) Re=10^5 (b) Re=10^6

It should be noted that the flow is not quite symmetric at the entrance of the computational domain due to an asymmetric section in the experimental setup.
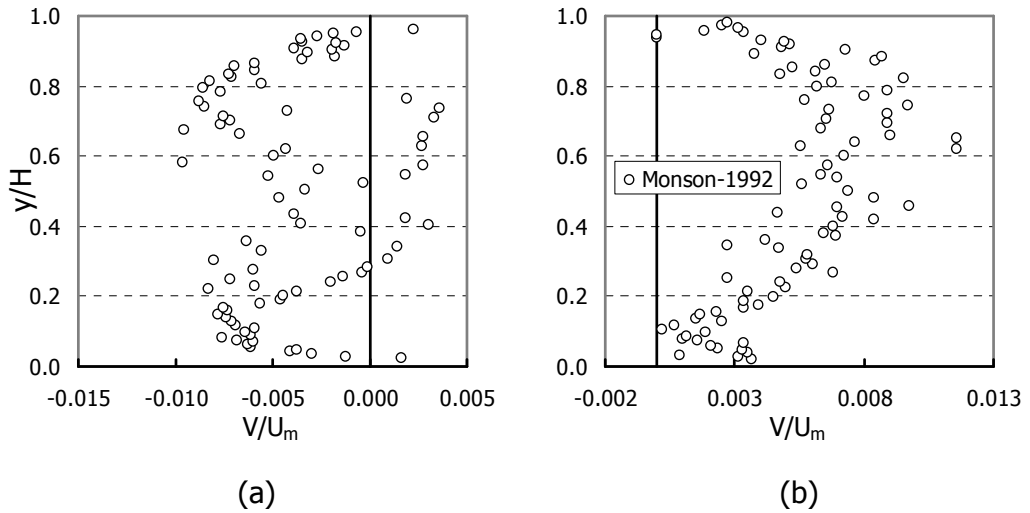
Figure 3.3. Vertical mean velocity (a) Re=10^5 (b) Re=10^6
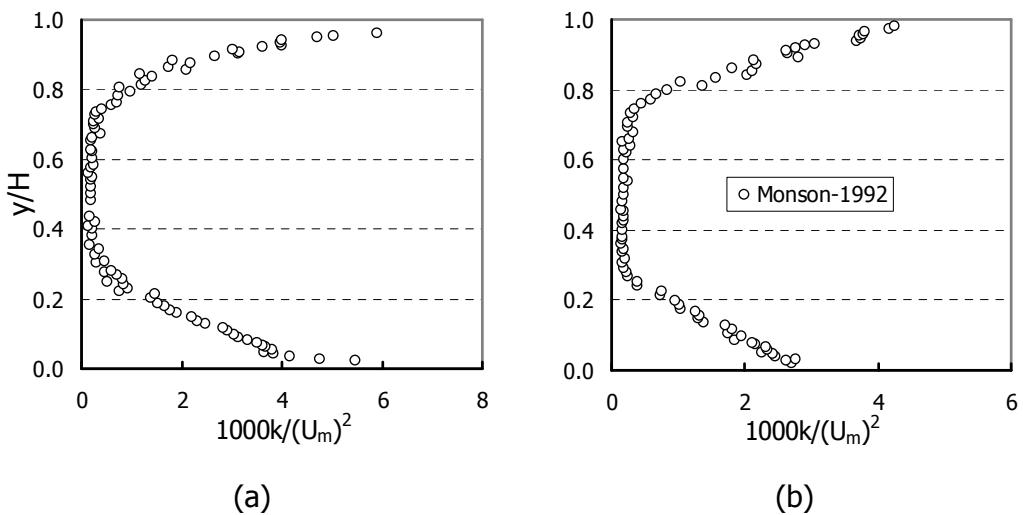
Figure 3.4. Inlet turbulent kinetic energy (a) Re=10^5 (b) Re=10^6

As shown in Figure 3.2, velocity profiles were not defined up to walls thus the remaining part of the inlet is modelled by using 1/7 power law which is a good assumption for a wide range turbulent flows;

$$u/U_m = (y/H)^{1/7}$$

$$(3.1)$$

Note that y is the wall normal direction and measured from inner surface to outer surface. The different inlet boundary condition quantities specific to the employed turbulence model are also evaluated with the help of the formulas obtained from ANSYS FLUENT Users Guide [83].

$$\ell = 0.07 \times H$$

$$\varepsilon = C_\mu^{3/4} \frac{k^{3/2}}{\ell}$$

$$\omega = \varepsilon/(kC_\mu) = \frac{k^{1/2}}{C_\mu^{1/4}\ell}$$

$$(3.2)$$

$$\overline{v^2} = \frac{2}{3}k$$

In equation set 3.2, C_μ takes value according to the turbulence model employed and finally, domain outlet is considered to be at atmospheric pressure. This test case will be named as "Monson's test case" in the continuing sections.

3.1.2   Rib Roughened Channel Flow

Second case have chosen as rib roughened channel flow because majority of the advanced cooling strategies employ various kind of rib configurations to increase the turbulence and so heat transfer. On the other hand, placement of rib turbulators into a cooling channel causes significant pressure drop thus a careful optimization procedure should be conducted and mechanism of this complex flow should be understand. To test the predictive capability of the RANS turbulence models against this flow phenomenon the experimental study of Casarsa [4] has been elected. In this study, square cross-sectioned (30 mm x 30 mm) rib turbulators were placed on one face of the stationary straight channel

with the pitch-to-height ratio of 10. The experimental setup of Casarsa is a scaled up model of turbine cooling channel;
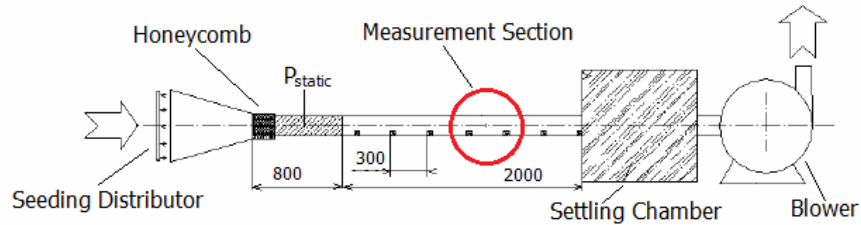
Figure 3.5. Experimental setup of Casarsa [4]

Channel has also a square cross-section with a 100 mm height thus rib turbulators provide a blockage ratio of 30 % which is in fact a high value for turbine cooling applications. Air at atmospheric pressure is aspirated through the channel with an engine representative Reynolds number value of 40000. The study of Casarsa [4] also documented that periodicity is already reached in flow and heat transfer characteristics between fourth and fifth rib. Therefore, a computational domain enclosed with periodic boundary conditions has been used.
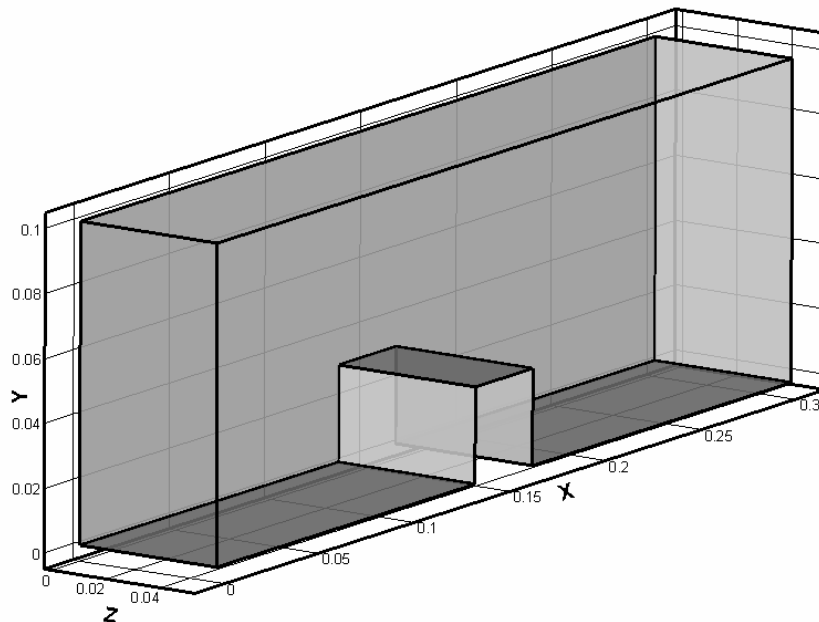
Figure 3.6. Computational domain of periodic flow on a rib turbulator

Employing periodic boundary conditions provides smaller computational domain and so reduces the computational costs. The target Reynolds number value is acquired by specifying the calculated mass flow rate in the periodic boundary condition. It should be noted that computational domain has been further reduced to half of it by using symmetry boundary condition and all the other boundaries are walls with adiabatic no-slip condition. This test case will be named as "Casarsa's test case" in the continuing sections.

3.1.3   Smooth Two-Pass Trapezoidal Channel

The cooling channels placed into the turbine blades are generally have a trapezoidal cross-section and the sizes of these channels are not same even on the same blade.
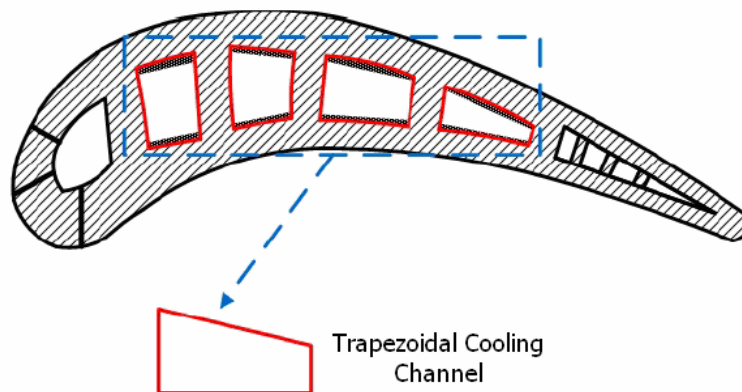
Figure 3.7.   Trapezoidal cooling channels with different dimensions

These trapezoidal cross-sections are connected to each other with sharp U-bends so in a real turbine, during flow experiencing streamline curvature effects studied at Monson's test case, it also undergoes to a compression-expansion phenomena. Cross-section change highly affects the speed, turbulence level and the maximum heat transfer location in the cooling channel and contrary to regular cooling channels (cross-sections of square or rectangular) the direction of the flow becomes important. It is important to represent that if RANS turbulence models are sensitive to this flow event. Therefore, the experimental

study of Lee [21] has been chosen as the third validation case. The full computational domain used in numerical simulations is shown in figure below.
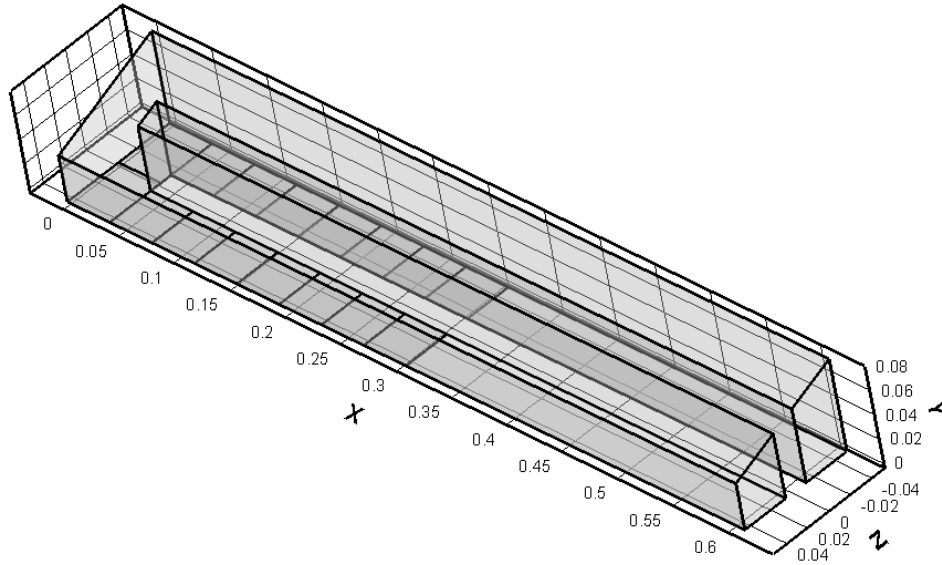
Figure 3.8. Smooth two-pass trapezoidal cooling channel

The channel end wall to inlet or exit was 610 mm and divider wall between two channels was 19.1 mm. The width of each section was 38.1 mm and the angle between top and bottom walls was 21.8 degrees. The dimensions of the trapezoidal cross-sections are shown at the following figure.
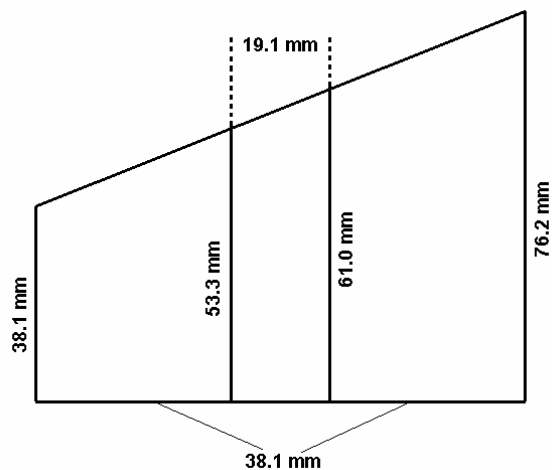
Figure 3.9. Cutaway cross-section of cooling channel

The simulations conducted for two Reynolds number values (16800 and 57200) based on mean velocity and hydraulic diameter of the rectangular flow cross-section between the tip of the divider wall and end wall. For lower Reynolds number value flow entrance from both smaller and larger channel inlets are simulated. Incompressible analyses have been conducted with a uniform velocity defined as the inlet boundary condition. The experiments were conducted by naphthalene sublimation technique and heat and mass transfer analogy was used to study heat transfer distribution at the bottom wall. The constant wall concentration of naphthalene is analogous to constant temperature wall boundary condition so all walls are considered to be at 350° K and fluid inlet temperature was selected as 310° K. The bottom wall has been separated to segments and area-averaged heat transfer data is obtained from each segment.
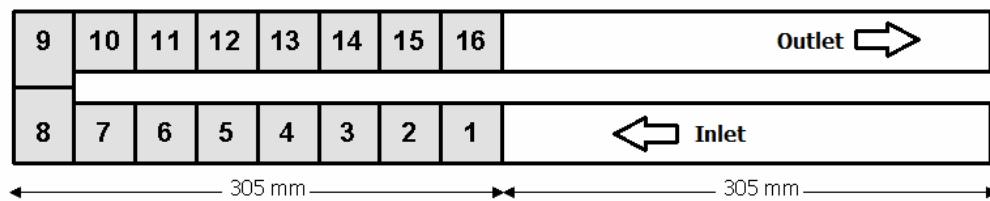
Figure 3.10. Segment numbers at the bottom wall of the channel

The segment numbers are related with the flow direction such that 1st segment is always at the inlet and 16th segment is always at the outlet side of the computational domain. The pressure-outlet boundary condition was imposed at the outlet and it was considered to be at atmospheric pressure. This test case will be named as "Lee's test case" in the continuing sections.

3.1.4   Two-Pass Cooling Channel with Angled Rib Turbulators

The rib turbulated serpentine cooling systems are typical for modern gas turbine cooling configurations. Therefore, experiments of Chen et al. [17] conducted by applying transient liquid crystal method has been used as the fourth test case. The two-pass cooling channel which equipped with 45° rib turbulators is somewhat combination of the two-dimensional U-duct configuration

and rib turbulated channel configuration which are presented as the first and second cases previously however, unlike them this case includes heat transfer and results of the simulation are discussed similar to the third test case. In Chen's experimental setup, a 1.8 m square duct and five layers of turbulence grid were installed before the test section to have a stable, fully developed flow with the appropriate turbulence intensity at the inlet of the test section. In numerical simulations channel has been extended ten times of the hydraulic diameter (1000 mm) to have a similar flow condition at the inlet and to lower the computational costs symmetry condition was applied. The computational domain of the cooling channel is shown in the following figure.
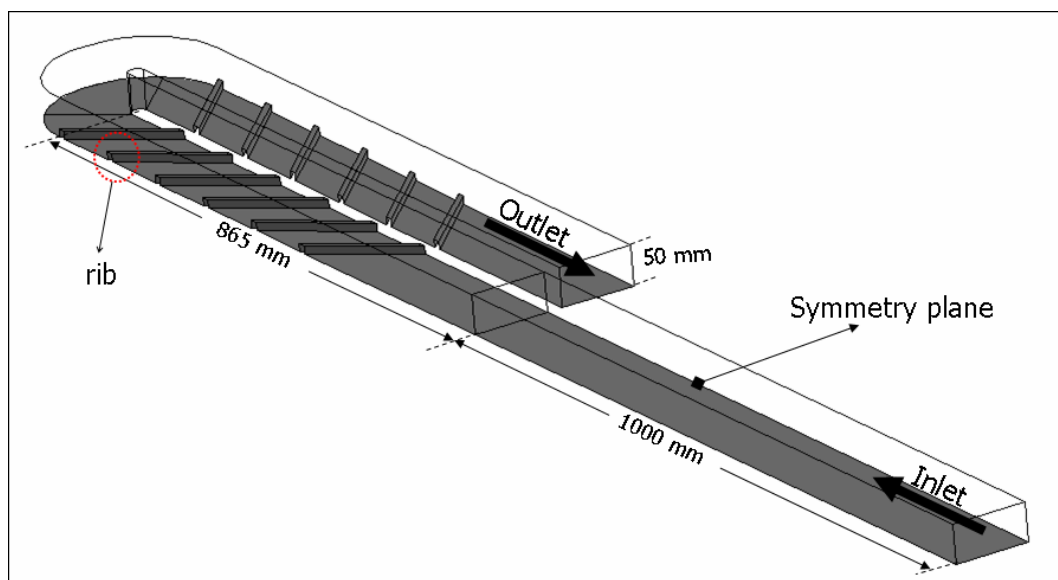
Figure 3.11. Rib turbulated two-pass cooling channel

The cooling channels were square cross-sectioned with 100 mm hydraulic diameter and connected to each other with a U-bend which has a 55 mm radius at the centreline. The divider wall between two ducts had a 20 mm thickness and its tip was cylindrically shaped with a radius of 10 mm. Channels were equipped with square cross-sectioned rib turbulators of which has a 10 mm height and 45° angled with the flow. The ribs are placed into the channel with a parallel arrangement and rib pitch-to-height ratio was 10. Dimensions of the cooling channel remaining from Figure 3.11 and segment numbers increasing in the flow direction are shown in the following figure.
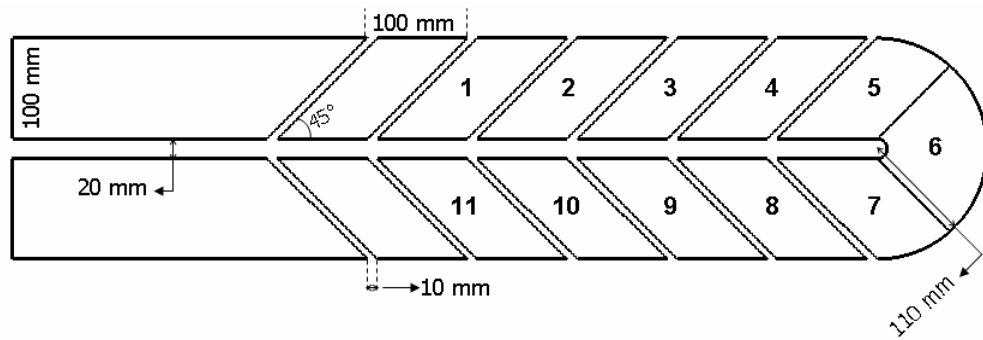
Figure 3.12. Segment numbers and dimensions of the cooling channel

The simulations conducted for Reynolds number value of 40000 based on mean velocity and hydraulic diameter of the channel. Incompressible analyses have been conducted with a uniform velocity defined as the inlet boundary condition. The walls are assumed to be at constant temperature wall boundary condition so all walls are considered to be at 303° K and fluid inlet temperature was selected as 313° K. The bottom wall has been separated to segments and area-averaged heat transfer data is obtained from each segment. Once again pressure-outlet boundary condition was imposed at the outlet and it was considered to be at atmospheric pressure. This test case will be named as "Chen's test case" in the continuing sections.

3.1.5   Turbine Vane Conjugate Heat Transfer (CHT)

At the first periods of turbine cooling analyses, prediction of turbine aerodynamic loading and heat transfer coefficient distributions were investigated separately tough, they are closely coupled in reality. Typically both internal and external heat transfer coefficients on the cooled turbine are predicted by boundary layer codes or empirical correlations using pressure distributions obtained from RANS analysis. This information is passed to a finite-element code as the boundary conditions of the solid zone and metal temperatures of the turbine blade are acquired by a conduction analysis. This decoupled approach requires simulating internal, external flows and solid blade separately and several iterative processes to improve solution accuracy. Besides, it is time-consuming

68

and accuracy is lost in the decoupling of the heat transfer modes. Therefore, conjugate heat transfer methodology, which allows a coupled approach to aerodynamics and heat transfer and provides simultaneous solution in the external and internal flows and conduction in the solid metal, became very popular. This methodology does not require any boundary condition on the walls and implements a physically-realistic approach by analysing every component in a single simulation. Although, recent computations conducted by CHT have offered promising results, its accuracy is still limited by the performance of applied turbulence model.

As mentioned above, CHT analyses test the turbulence models in every aspects of complex flow problem. Thus, in order to conclude the investigation about the predictive capabilities of RANS based turbulence models on turbine cooling analysis, experimental study of Hylton et al. [28] is chosen as the fifth test case. In this test case, engine-realistic conditions in the test section were supplied from the discharged flow from a burner. The simulated experiment consists of linear cascade of three NASA C3X vanes which are internally cooled by air flowing radially through ten round cooling holes. Linear cascade and placement of the instrumentation is shown in the following figure.
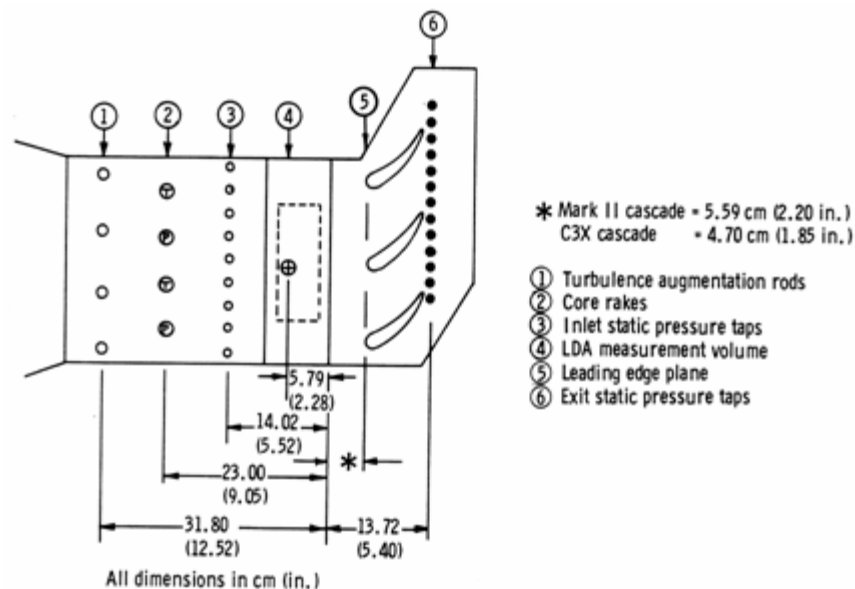
Figure 3.13. Experimental setup of Hylton et al.[28]

Only the vane at the center is instrumented for temperature and pressure distributions and coolant mass flow rate for each radial hole of this vane is documented. In the numerical simulations the NASA C3X vane is created from the points in x-y plane provided by Hylton et al. [28] and to replicate the linear cascade, periodic boundary conditions with no pressure drop (different from Casarsa's test case) has been used. Periodic boundary shape is kept similar to streamline shape at the center of vane passage for optimum accuracy and periodic planes are separated by 117.3 mm from each other. Computational domain and boundary conditions types used for numerical simulations are shown in the following figure.
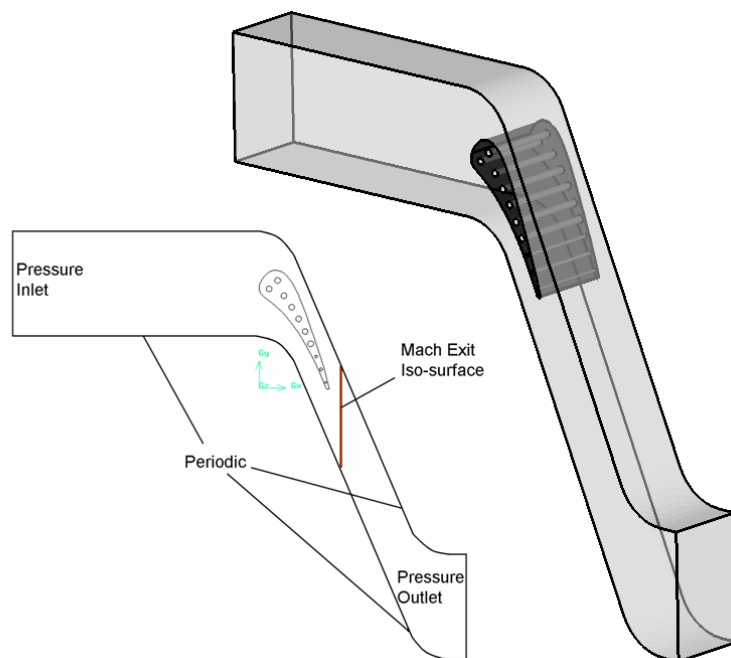
Figure 3.14. Computational domain and boundary condition types

The NASA C3X vane has a 76.2 mm span with no twist, true chord of 144.93 mm and axial chord of 78.1558 mm. The distance between the inlet boundary to NASA C3X vane in the computational domain is the same with the total pressure and temperature measurement plane (section 2 in Figure 3.13) to vane leading edge plane (section 5 in Figure 3.13) in the experimental setup. The outlet plane was located approximately 1.5 times of the true chord downstream of the trailing edge. Surface temperatures and pressures were measured at the

mid-span of the blade. The hole numbering and measurement plane are shown in the following figure.
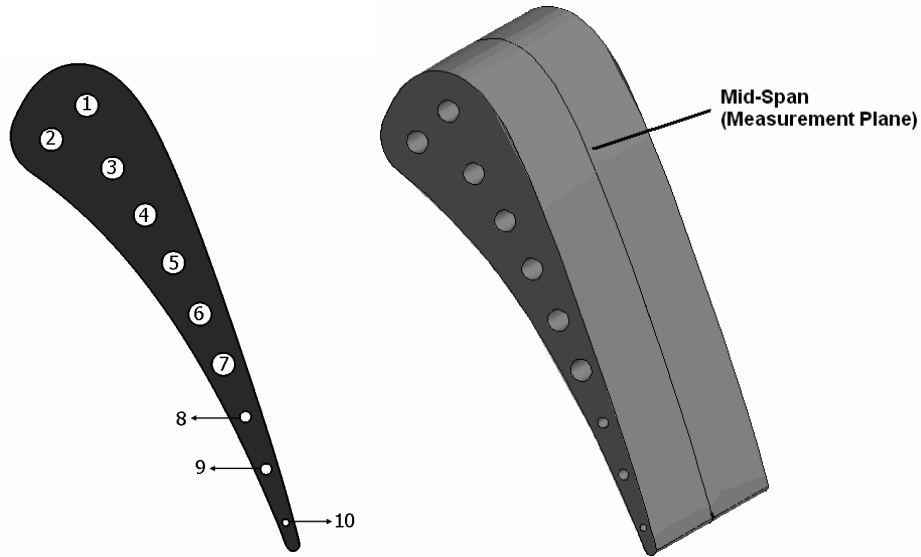
Figure 3.15. Cooling channel numbering and measurement plane

Experiments conducted on the NASA C3X vane were classified according to four control variables which are exit Mach number, exit Reynolds number, inlet turbulence intensity and blade surface temperature ratio. Two distinct flow conditions have been chosen for simulations in terms of exit Mach number, exit Reynolds number and inlet turbulence intensity to clearly compare the capabilities of the turbulence models. The boundary conditions of these flow cases are given in the following table.

Table 3.1.   Hylton's test case boundary conditions

	P_o (kPa)	T_o (K)	M_i	M_e	ℓ (m)	Tu (%)	Re_e
Case 1(Run 149)	245	795	0.17	0.92	0.016	6.5	1.51×10^6
Case 2 (Run 155)	386	789	0.17	1.06	0.016	8.3	2.47×10^6

The exit Mach number and Reynolds number were reported at the wake of the vane where static pressure taps are located. In numerical simulations, the

iso-surface named Mach exit, which is shown in the Figure 3.14, is created as a control surface that has no effect on the solution. This surface is placed at the same coordinates (x=90.18319 mm) with the pressure taps placed at the wake of the vane. To fully simulate the flow conditions, static pressure at the outlet is adjusted until the Mach number at the Mach exit iso-surface matches the experimental exit Mach number. For both cases turbulence length scale was set at 0.016 m which is about 20% of the span [49] and turbulence intensity values were taken directly from experiments.

The cooling setup was designed to give uniform blade surface temperatures to minimize the error in the calculation of heat transfer coefficients, thus mass flow in the cooling channels were individually controlled. In numerical simulations mass flow inlet boundary condition is used for coolant channel inlets. Following table shows the channel diameter values of the NASA C3X vane and coolant mass flow rates of two studied cases.

Table 3.2.   Channel diameters and mass flow rates

Hole Number	Diameter (m)	Mass Flow Rates (kg/s)	
		Case 1 – Run 149	Case 2 – Run 155
1	0.0062992	0.00793	0.00817
2	0.0062992	0.00706	0.00822
3	0.0062992	0.00700	0.00770
4	0.0062992	0.00721	0.00841
5	0.0062992	0.00747	0.00889
6	0.0062992	0.00738	0.00916
7	0.0062992	0.00697	0.00873
8	0.0030988	0.00248	0.00290
9	0.0030988	0.00137	0.00172
10	0.0019812	0.000789	0.000953

The flow was assumed to be fully developed at the hole inlets as there were long tubes feeding the radial channels in the experiment of Hylton et al.

[28]. To represent this situation the cooling channels were solely solved isothermally and resultant mass flow rate distributions at the exit of the channels were implemented to the real cases by an inlet mass flow rate profile file. In the description of the experiments, Hylton et al. [28] did not presented the measured inlet and exit total temperature values. Therefore, assuming that all cooling channels have been fed from same source and there were no heat addition to the tubes carrying coolant flow, inlet total temperature of 300K has been imposed to all cooling channels [49]. The inlet turbulence intensity for all channels was 0.2%. The pressure-outlet boundary condition was imposed at the channel outlets and it was considered to be at atmospheric pressure. This test case will be named as "Hylton's test case" in the continuing sections.

3.2   Numerical Methods and Mesh Strategies

The numerical simulations are conducted with commercial software ANSYS FLUENT 13.0. The steady, time-averaged Navier-Stokes equations were solved, and pressure-velocity coupling was achieved with the SIMPLE algorithm. In all simulations if convergence is acquired, all equations were discretized with second-order accuracy. However, for RSM in which Reynolds stresses are highly coupled with momentum equations, turbulence discretization was always kept at first-order accuracy to obtain converged solutions. Otherwise, it is observed that simulations were rapidly diverging. It should also be noted that it is advised to employ PRESTO for the high-order pressure discretization in incompressible flow problems including high streamline curvature. Therefore, for the first four cases PRESTO has been employed. The Hylton's test case however, is a highly compressible test case especially in the cooling channels and ANSYS FLUENT 13.0 Users Guide advises to employ second-order accuracy in this kind of flow problems for high-order pressure discretization. Thus, second-order accuracy is employed for the pressure discretization in the numerical simulations of the fifth test case. Green-Gauss node based spatial discretization scheme is preferred because it is known to be more accurate with unstructured tetrahedral meshes.

The computational presented for all test cases are consist of tetrahedral (triangular for 2D) and prism (quad for 2D) cells. Prism cells are created with TGRID to model boundary layer and tetrahedral cells are created with GAMBIT to fill the remaining domain. Boundary layer modeling is performed with great care 20 layer is prism cells created that first 10 layers expand from wall surfaces with geometric growth ratio of 1.15 to capture high velocity and thermal gradients occurring at near wall region. Remaining 10 layers are created with the last ratio method to provide a smooth transition between prism cells to tetrahedral cells.
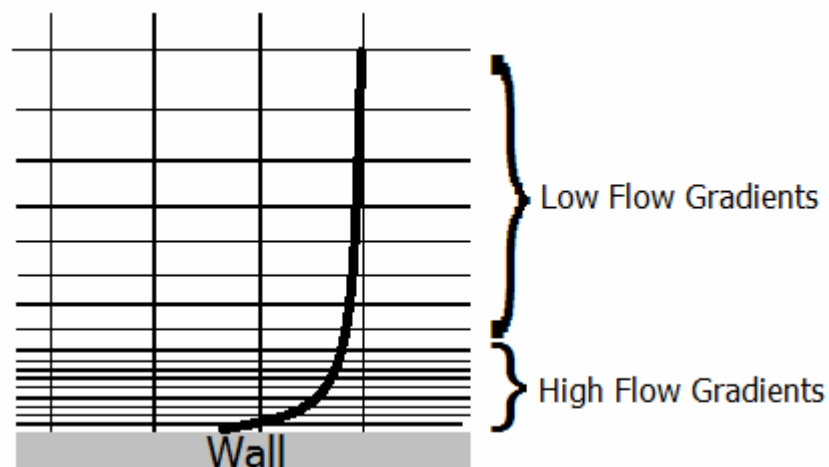
Figure 3.16. Near wall modeling

In all simulations, first heights of the boundary layers were selected such that y^+ values at all regions and flow conditions are kept smaller than 1. Remaining domains were filled with tetrahedral cells by a growth ratio of 1.15. None of the cases, grid independency study is conducted. Instead, grid dependency studies conducted by previous researchers were examined and grids were generated in accordance with those studies. Investigated grid sensitivity studies for Monson's test case were conducted by Rumsey et al. [41], Cokljat et al. [81] and Luo et al. [56]. Rumsey et al. [41] used a medium mesh consists of nearly 16000 hexahedral cells and fine mesh consists of nearly 64000 hexahedral cells and results obtained from these meshes did not show significant differences. Total cell counts of the meshes employed by Luo et al. [56] and Cokljat et al. [81] after the grid independence study were nearly 41000 and 38000 respectively. Studies of Fransen et al. [84] and Vass [85] were

investigated for grid sensitivity of Casarsa's test case. Fransen et al. [84] conducted a grid independence study with grid sizes of 550000, 1800000 and 5500000 cells and concluded that there is no significant difference between the medium and fine grid in terms of velocity profiles. Vass [85] used grid size of nearly 470000 for the same problem and it should be noted that both researchers conducted LES analyses with mentioned grids. Lee's test case was previously simulated by Siddique et al. [86]. Three different grids sizes with cell numbers of 1900000, 3100000 and 4820000 have been generated for the most complex case (ribs on three walls) and a maximum deviation of 1.85 % in the area averaged Nusselt number was found. The coarsest grid has been employed by Siddique et al. [86] for remaining simulations. Chen's test case was simulated by Chen et al. [17]. It is reported based on the grid independency study, suitable grid size found as 2200000 cells. As mentioned before, Hylton's test case has been used in various studies for validation purposes. Investigations of York [49], Facchini et al. [50] and Luo et al. [54] have been examined for grid independency. York [49] reported nearly 3750000 cells for hot gas path, 1600000 cells for solid and 1340000 cell for cooling holes thus a total grid size of 6700000 cells. Facchini et al. [50] reported a very coarse grid with respect to York [49] by using 700000 cells for hot gas path, 190000 cells for solid and 280000 cells for cooling holes thus a total grid size of 1170000 cells . Luo et al. [54] reported a moderate grid size with a total cell number of 3100000. In this grid, about 1400000 cells for hot gas path, 700000 cells for solid and 1000000 cells for cooling holes have been used. The sizes of the grid employed in this study are listed in table below.

Table 3.3.   Total cell numbers of the grids used for simulations

Test Case	Monson	Casarsa	Lee	Chen	Hylton
Number of Elements	82636	2141816	2793635	4808465	5307301

As can be seen Table 3.3 finer meshes have been used with respect to previous studies. In the test cases of Monson, Casarsa and Chen, employed

meshes are far finer than previous ones and in the case of Lee contrary to geometry modelled by Siddique et al. [86]; tabulated cell number is valid for the smooth channel simulation that is sufficiently fine. In the grid employed for Hylton's test case; 2740000 cells for hot gas path, 1180000 cells for solid and 1380000 cells for cooling holes have been used. The mesh size was far finer than the grids employed by Facchini et al. [50] and Luo et al. [54] but coarser than grid used by York [49]. This was caused from the lack of the computational resources.

Verifying solution convergence criteria is a critical step to achieve accurate results. As simulated test cases are very different from each other a single convergence criterion is not possible. Therefore, observed quantities were different for each case. In the Monson's test case the wall drag force, Casarsa's test case periodic pressure drop, Lee's and Chen's test cases wall drag force together with bottom wall heat flux and finally Hyton's test case vane surface temperatures were constant with additional iterations. The meaning of "constant" in this case is observed quantities were changing less than 1% after several hundred iterations. Addition to these constraints the temperature, heat flux and pressure contours are observed in the critical areas and verified that they are not changing with additional iterations.

3.3   Additional Considerations on Heat Transfer Modeling

Analyses related with turbine cooling may require additional material modeling because of the changes in the temperature values throughout the computational domain. Especially in the conjugate heat transfer analysis, temperature dependent properties of both solid and fluid materials should be modelled carefully to obtain accurate results. For this reason, molecular viscosity, thermal conductivity and specific heat of air were modelled as 6th order polynomial functions of temperature, which were acquired through a best-fit of available tabulated data. The general format of the polynomial function can be given as follows;

$$\phi(T) = A_0 + A_1T + A_2T^2 + A_3T^3 + A_4T^4 + A_5T^5 + A_6T^6 \qquad (3.3)$$

The tabulated data for molecular viscosity of air ranging from 85K to 2000K are acquired from the study of Kadoya et al. [87]. Same study is also utilized for thermal conductivity data and additionally, investigation of Stephan et al. [88] has been made use of. Tabulated data of the two studies, which have been selected similar sources as the reliable data sets, have been combined to generate polynomial equation. The data presented by Kadoya et al. [87] was once again ranged from 85K to 2000K and Stephan et al. [88] was ranged from 70K to 1000K. Specific heat data was reported by Park et al. [89] and ranged from 100K to 4000K. The coefficients of the polynomials used to model these air properties are given in the following table.

Table 3.4. Coefficients of the polynomials

Coefficients	Molecular Viscosity (kg/m.s)	Thermal Conductivity (W/m.K)	Specific Heat (J/kg.K)
A_0	-4.938765E-07	-8.707956E-04	1.020140E+03
A_1	8.410710E-08	1.116641E-04	-2.490412E-01
A_2	-9.110942E-11	-9.274773E-08	8.285550E-04
A_3	8.996424E-14	8.217279E-11	-6.751344E-07
A_4	-5.432558E-17	-4.367839E-14	2.568782E-10
A_5	1.764147E-20	1.267559E-17	-4.726902E-14
A_6	-2.350264E-24	-1.533084E-21	3.391438E-18

The variation of the molecular viscosity, thermal conductivity and specific heat of the air with temperature is shown in the following figures.
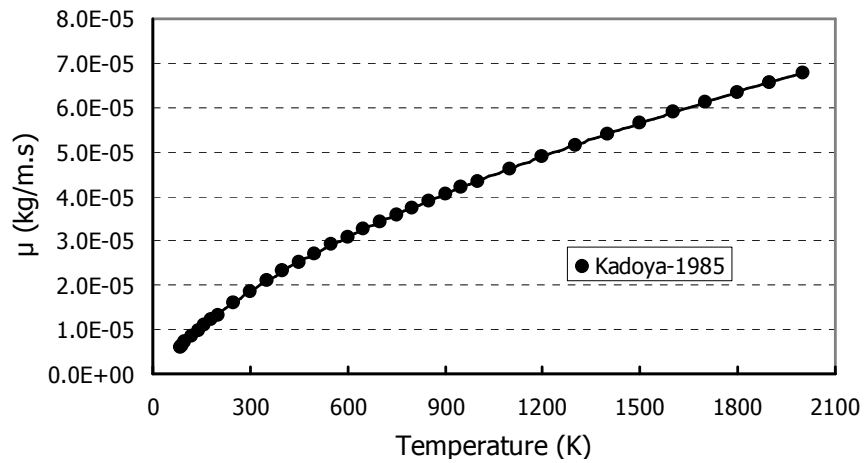
Figure 3.17. Change of molecular dynamic viscosity of air with temperature
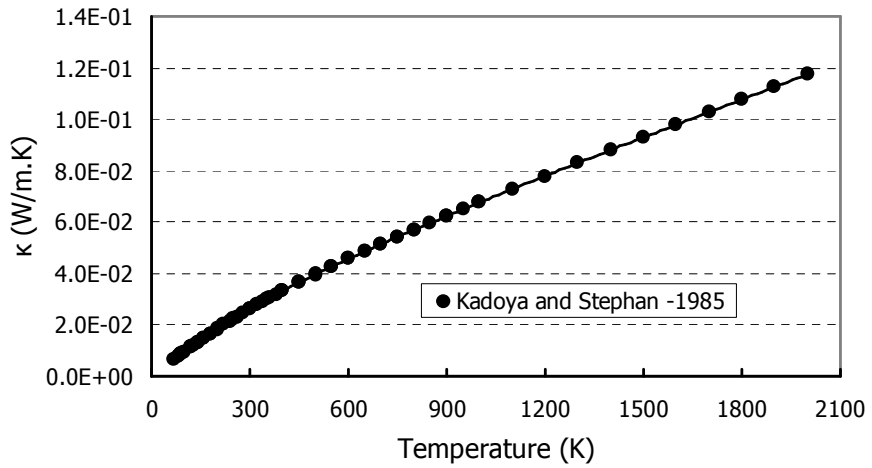
Figure 3.18. Change of thermal conductivity of air with temperature
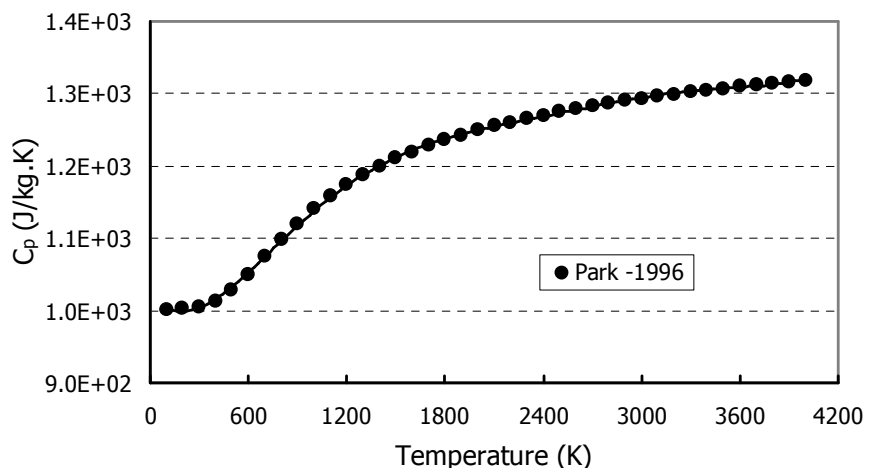
Figure 3.19. Change of specific heat of air with temperature

The vanes were fabricated from ASTM 310 stainless steel and according to experimental data from Goldsmith et al. [90] this material has a nearly constant density of 7900 kg/m^3 and specific heat of 585.15 J/kg.K at the temperature range of experiments conducted. Also based on experimental data of Goldsmith et al. [90], the thermal conductivity was specified by the following linear relationship.

$$\kappa = 0.020176T + 6.811 \text{ (W/m.K)} \tag{3.4}$$

Above equation is specified for temperature range from 300K to 800K which is sufficient for the simulations of Hylton's test case. Moreover, ASTM 310 stainless steel has a relatively low thermal conductivity which reduces the measurement errors.

CHAPTER 4

RESULTS and DISCUSSIONS

In this section, results of the numerical simulations related with the aforementioned experimental test cases have been discussed. The order of the results introduced is the same with the test cases presented at Chapter 3.

4.1   Monson's Test Case

Results related with Monson's test case have been presented in terms of streamwise velocity profiles, turbulent kinetic energy profiles, pressure coefficient and friction coefficient distributions. The first two quantities have been normalized with U_m and presented in wall normal direction which was always measured inner wall to outer wall. The last two quantities were pressure coefficient and friction coefficient distributions which have been plotted in streamwise direction that is always measured inlet to outlet.

4.1.1   High Reynolds Number Case (Re=10^6)

As mentioned before in Figure 3.1, results will be plotted at four different sections. The first section is located at s/H=2 at where prediction capabilities of the turbulence models before the flow becomes complex can be examined.
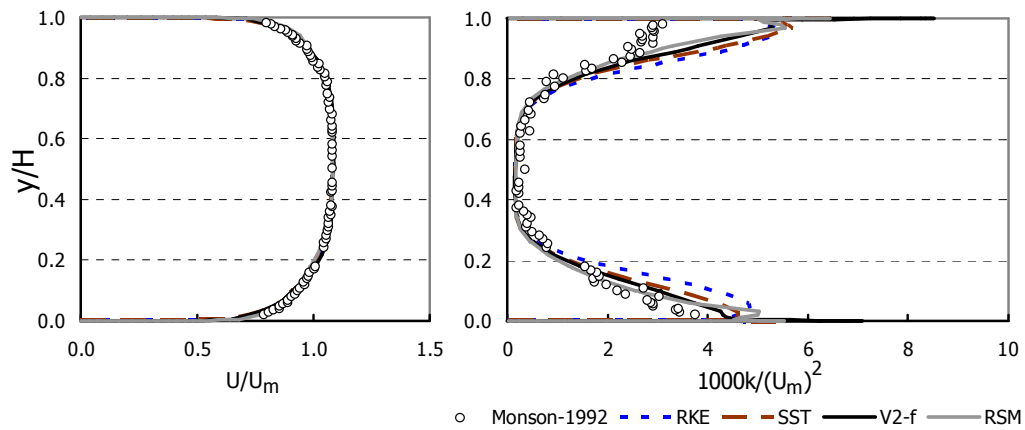
Figure 4.1. Normalized velocity and turbulent kinetic energy profiles at s/H=2

As can be seen in Figure 4.1, velocity profile at the s/H=2 is nicely resolved by all turbulence models which shows that velocity profiles at the inlet were implemented correctly. The RSM model has a slightly better turbulent kinetic energy prediction than other turbulence models at this location.

The velocity and turbulent kinetic energy profiles at the next section, the entrance of the U-bend geometry, can be seen in Figure 4.2. As expected, flow becomes faster near the inner wall and once again velocity profile is correctly predicted by all turbulence models.
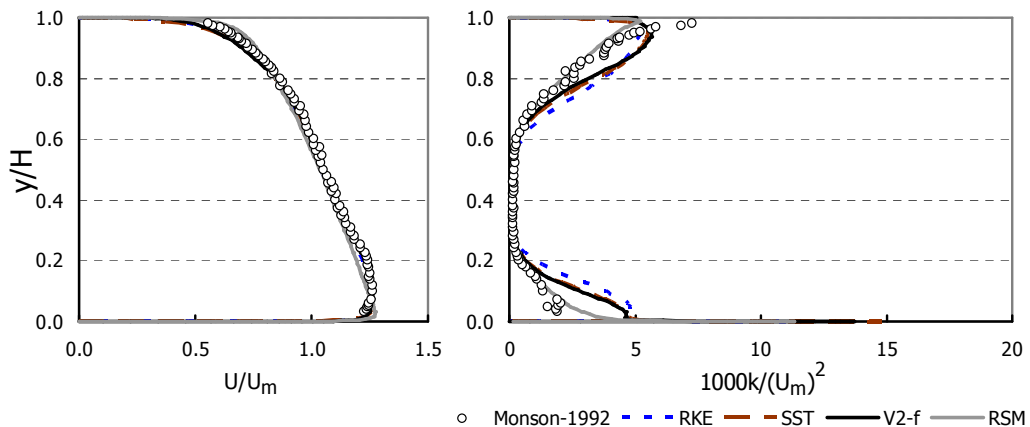
Figure 4.2. Normalized velocity and turbulent kinetic energy profiles at θ=0°

Turbulent kinetic energy predictions of the RSM were superior to other turbulence models at both regions near the inner wall and outer wall. The

inviscid flow occupying the core of the channel is correctly predicted by all turbulence models.

The third section was the halfway of the bend section and results related with this region of the geometry were presented at Figure 4.3. The increasing complexity of the flow caused from the geometry resulted with inaccurate predictions. Velocity profile has been underpredicted near the outer wall. Only the RSM succeeded to resolve the velocity distribution accurately.
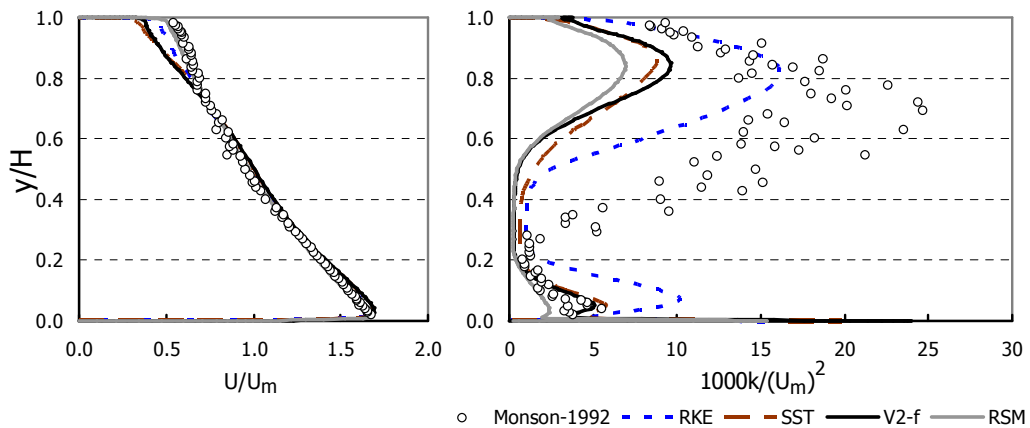
Figure 4.3. Normalized velocity and turbulent kinetic energy profiles at $\theta=90^\circ$

On the other hand, even RSM lacked to resolve turbulent kinetic energy distribution at this region. In this region experiments have shown decrease in turbulent kinetic energy near the inner wall and increase close to outer wall. This behavior has not been presented by any of turbulence models employed. The RKE gave the best yet unsatisfactory predictions near the outer wall. Close to inner wall region V2-f and SST provided the best results. At this region RKE came up with excessive turbulence predictions.

At the bend exit region, predictions were significantly different from experiments as presented in Figure 4.4. Velocity distribution has been underpredicted at the core of the channel by all turbulence models moreover close to inner wall magnitude of the negative velocity and height of the boundary layer is underpredicted.
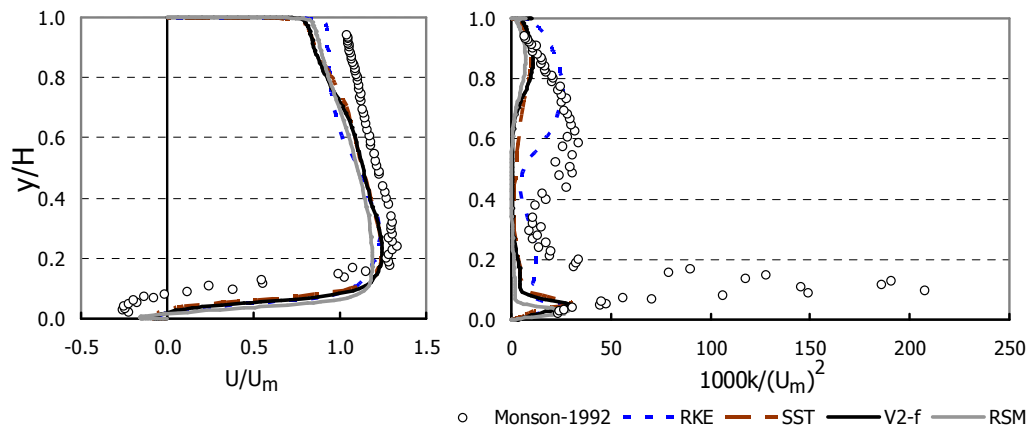
Figure 4.4. Normalized velocity and turbulent kinetic energy profiles at $\theta=180°$

All turbulence models also failed to resolve turbulent kinetic energy distribution satisfactorily. High turbulent kinetic energy caused from flow separation is missed by all turbulence models. Only the RKE has predicted high turbulence values at the upper half of the Figure 4.4, close to outer wall however, maximum turbulent kinetic energy value and the location it occurs has not been predicted accurately.

Figure 4.5 and 4.6 show predicted and measured pressure coefficient values.
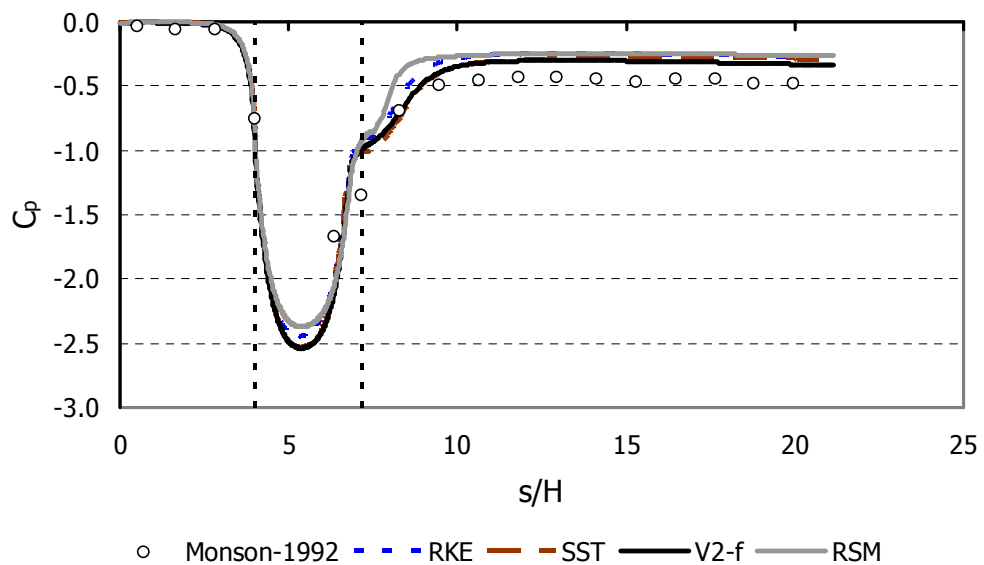
Figure 4.5. Pressure coefficient distribution on the inner wall
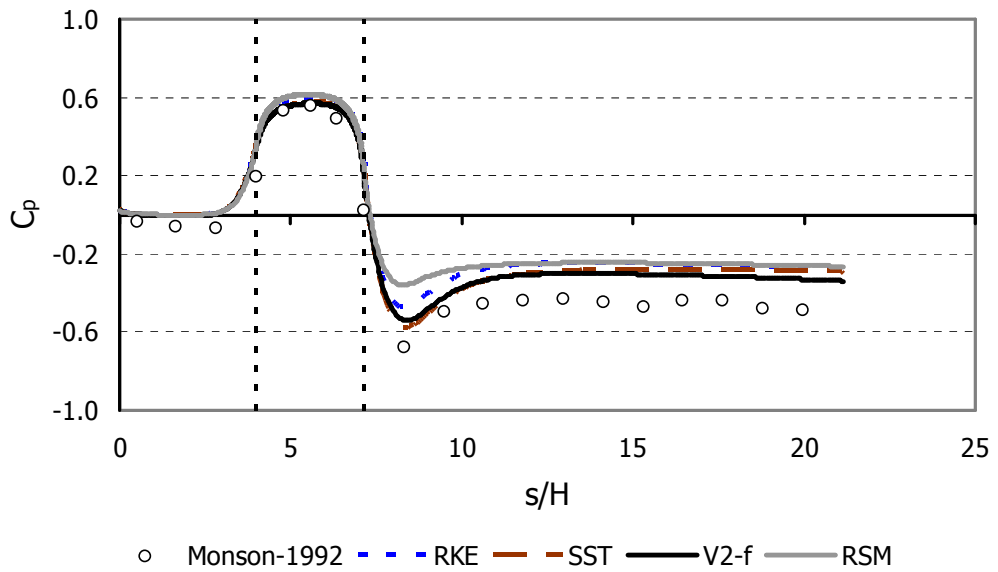
Figure 4.6. Pressure coefficient distribution on the outer wall

All models came up with good predictions of pressure coefficient both in inner wall and outer wall. Predictions of the bend region are highly accurate especially at the outer wall region and best results are provided by V2-f model throughout the wall regions.

Figure 4.7 and 4.8 show predicted and measured friction coefficient values.
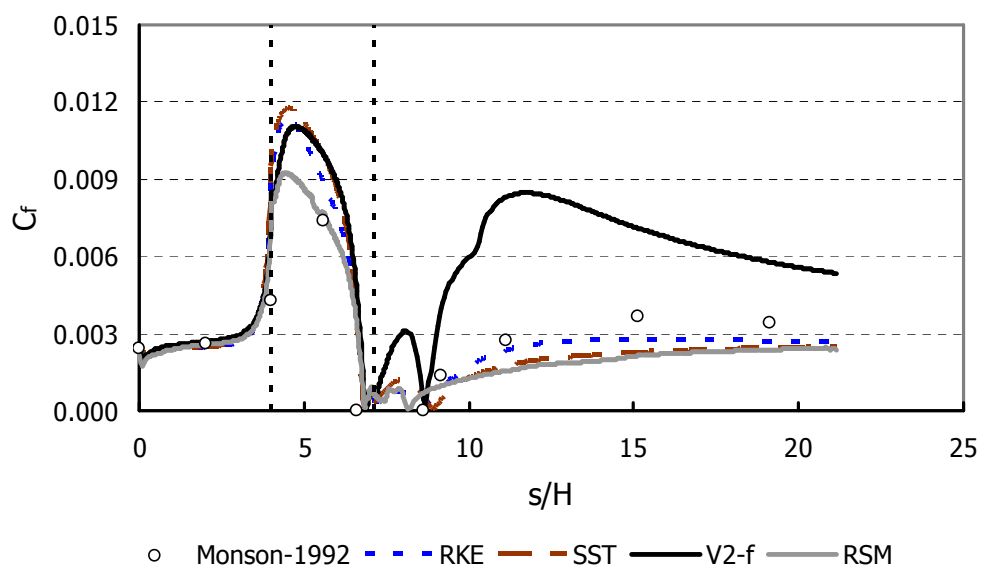
Figure 4.7. Friction coefficient distribution on the inner wall
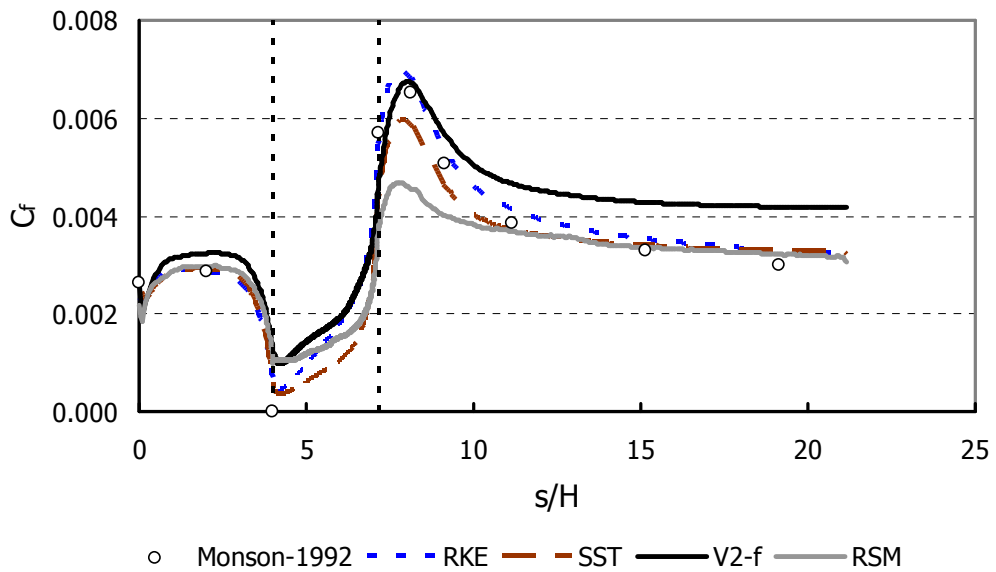
Figure 4.8.   Friction coefficient distribution on the outer wall

Although, mean flow is dominated by pressure gradient the turbulent and so heat transfer behavior the flow can be determined from friction coefficient. Similar to turbulent kinetic energy predictions, best friction coefficient results are obtained from RKE model throughout the wall regions.

As can be seen in Figure 4.7, V2-f model predicts unexpected friction coefficient values at the inner wall region, downstream of flow re-attachment. This situation is caused from the non-physical overprediction of $\overline{v^2}$ mentioned by Davidson et al. [70] which causes high turbulent viscosity values and Reynolds analogy indicates that V2-f would also cause inaccurate heat transfer rate predictions at these regions.

4.1.2   Low Reynolds Number Case (Re=10^5)

Similar to high Reynolds number case, results of the section s/H=2 have been given firstly to prove that velocity profiles used as boundary conditions were implemented correctly. At low Reynolds number case, inlet velocity profile is not quite symmetric and this situation remains at s/H=2 region. As can be

seen from Figure 4.9 all turbulence models accurately predicted the velocity distribution before the flow becomes complex.
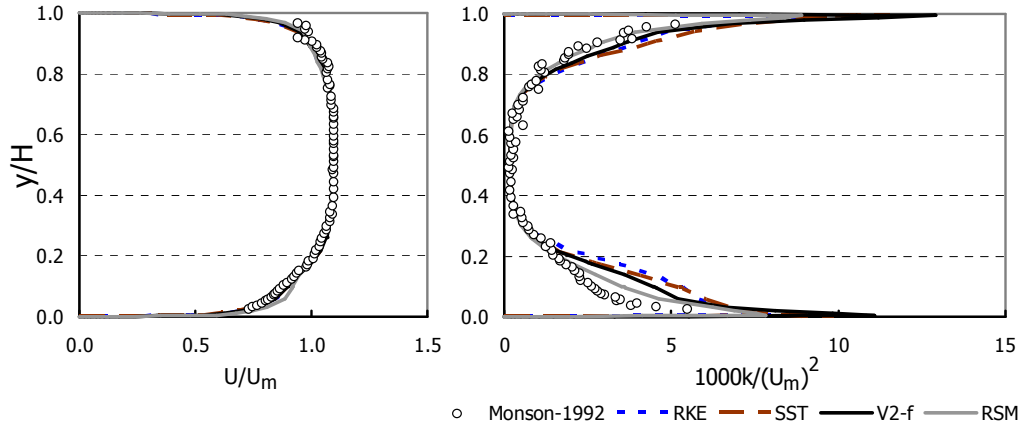
Figure 4.9. Normalized velocity and turbulent kinetic energy profiles at s/H=2

All turbulence models have accurately predicted the turbulent kinetic energy at the core region moreover; RSM has the best turbulent kinetic energy predictions close to inner wall and highly accurate results at the outer wall region.

At low Reynolds number, U-bend entrance results have been presented at Figure 4.10. Velocity profile is correctly resolved by all turbulence models at this region. The RSM has slightly the best predictions close to inner wall and slightly the worst predictions close to outer wall.
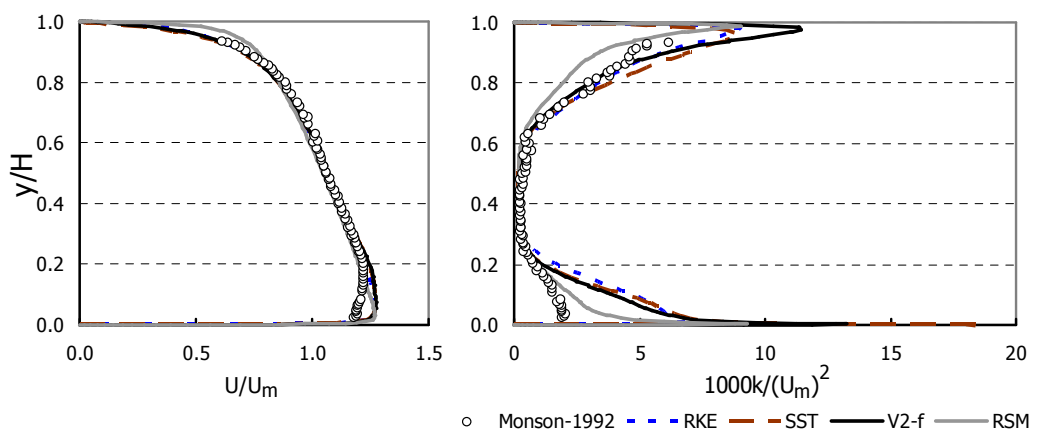
Figure 4.10. Normalized velocity and turbulent kinetic energy profiles at $\theta=0^o$

Turbulent kinetic energy predictions of the RSM were once again superior to other turbulence models at the inner wall region. Similar to velocity distribution, turbulent kinetic energy predictions of the other three turbulence models were slightly better at the outer wall region.

Results of the low Reynolds number case at the halfway of the bend are presented at Figure 4.11. All turbulence model accurately predicted the velocity at the core region of the duct and regions close to inner wall. Velocity profile at the outer wall region was accurately predicted only by RSM.
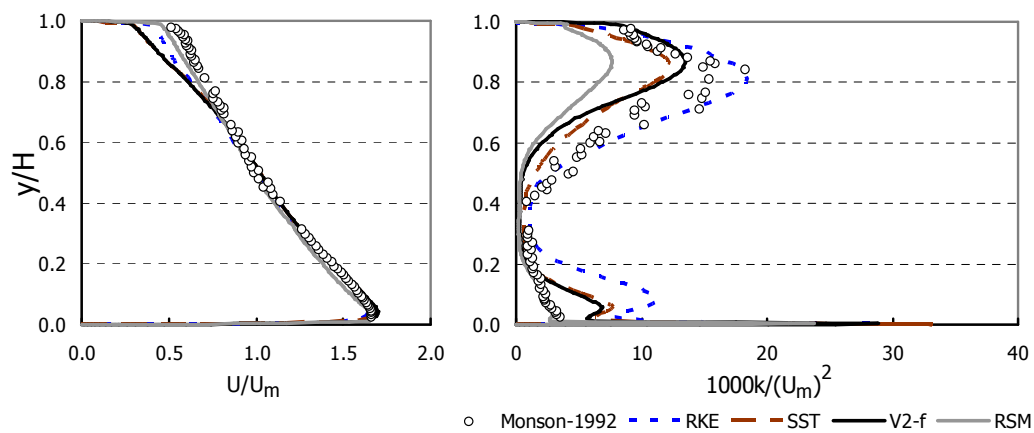
Figure 4.11. Normalized velocity and turbulent kinetic energy profiles at $\theta=90^{\circ}$

Although, RSM succeeded to resolve the velocity distribution throughout the duct, turbulent kinetic energy distribution was predicted accurately only at the inner wall region. Similar to high Reynolds case RKE came up with very accurate results at the outer wall region. Remaining turbulence models were not accurate but they followed the general trend.

At the bend exit, similar to the high Reynolds number case velocity distribution predictions were inaccurate. Moreover, unlike the high Reynolds number case velocity distribution at the core of the channel and height of the boundary layer were overpredicted. As can be seen from the Figure 4.12, magnitude of the negative velocity was accurately predicted by all turbulence models except RKE.
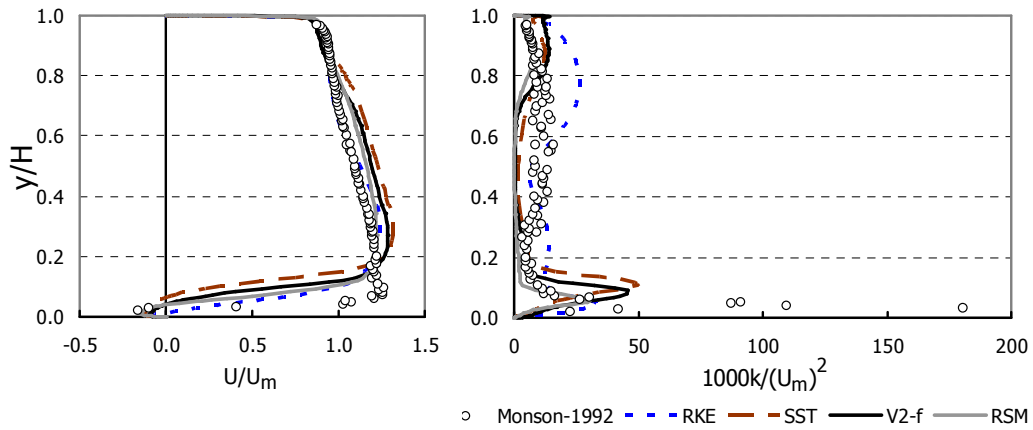
Figure 4.12. Normalized velocity and turbulent kinetic energy profiles at θ=180°

The turbulent kinetic energy distribution was not satisfactorily resolved by any of the turbulence models employed. All models failed to predict the turbulence occurring at the core of the channel and RKE predicted high turbulence near the outer wall which was not the true for low Reynolds number case. Moreover, RKE came up with a turbulent kinetic energy prediction which was very similar to the high Reynolds number case presented earlier. This similarity indicates that turbulence values predicted by RKE are not primarily flow dependent so they originate from the turbulence formulation itself.
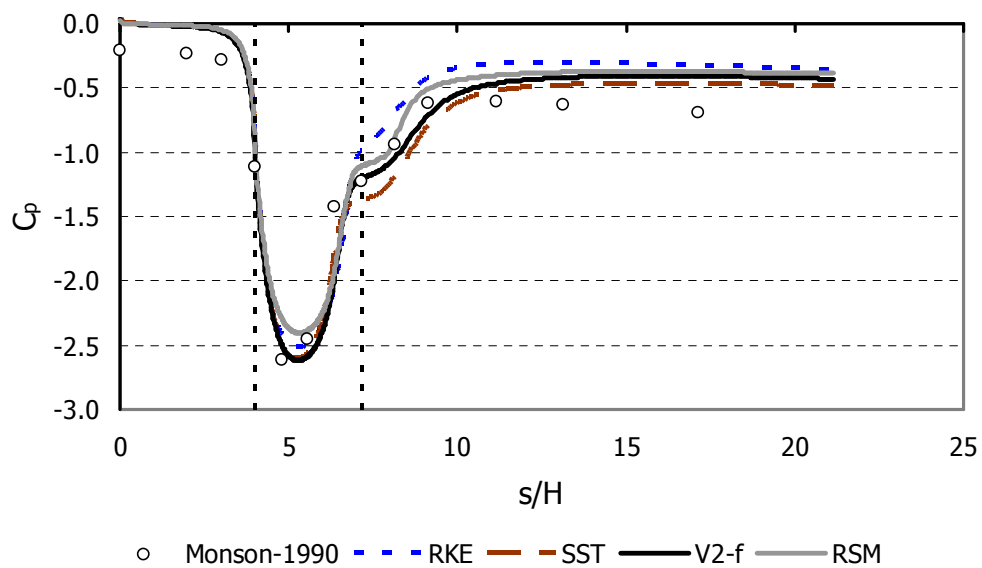
Figure 4.13. Pressure coefficient distribution on the inner wall

Figure 4.13 and 4.14 show predicted and measured pressure coefficient values for low Reynolds number case.
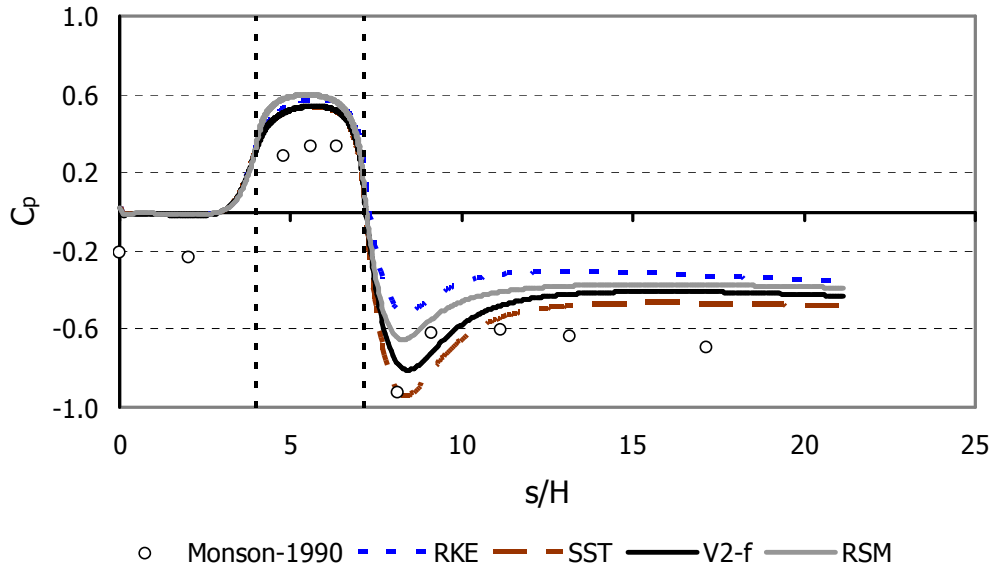
Figure 4.14. Pressure coefficient distribution on the outer wall

All of the turbulence models captured the general trend of the pressure coefficient along the inner and outer walls. However, reference pressure is not well defined at the experiments. In the evaluation of pressure coefficient, inlet static pressure is used as the reference pressure. This method worked well in the high Reynolds number case however, it also created an offset between the experimental data and the predictions at low Reynolds number case. When the inlet values were matched V2-f seems to provide the best predictions.

In Figure 4.15 and 4.16 measured and predicted pressure coefficient values for low Reynolds number case have been presented. Along both walls V2-f model is in good agreement with the experimental results. However, this model once more creates unexpected friction coefficients once again. Contrary to high Reynolds number case these values occurred on the outer wall in the bend region. This non-physical behaviour of the V2-f model should be fixed to have reliable predictions and the first suggestion of the Davidson et al. [70] seems the most prospective solution to this problem.
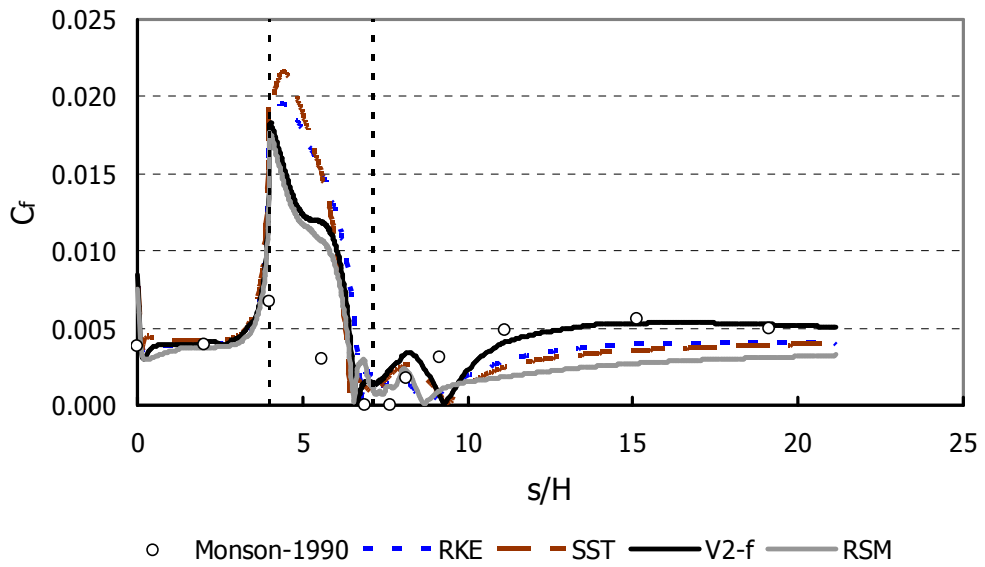
Figure 4.15. Friction coefficient distribution on the inner wall
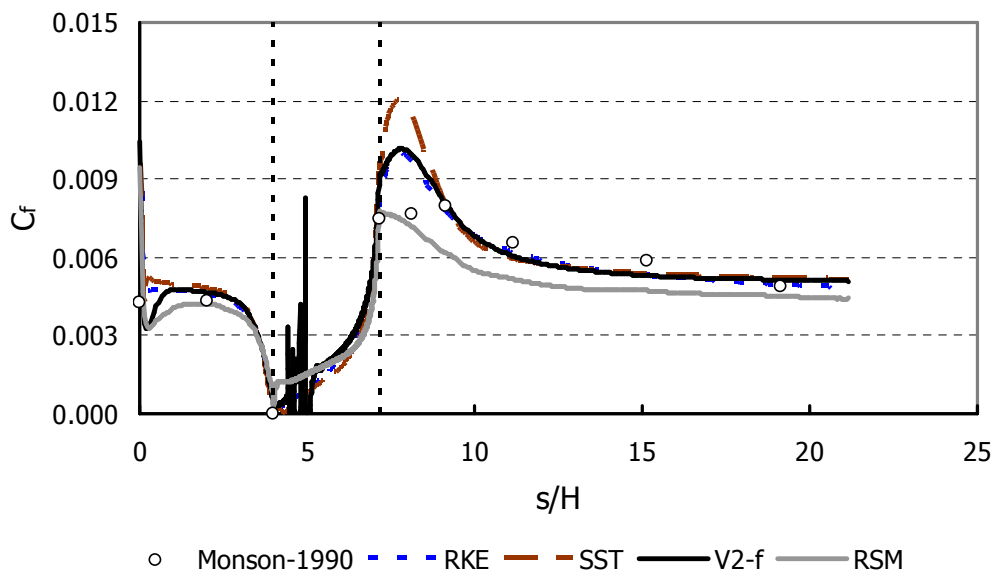
Figure 4.16. Friction coefficient distribution on the outer wall

According to the literature survey, experimental studies of the Monson et al. [13] has not been investigated at this extend before. The results obtained were in well accordance with the findings of Rumsey et al. [41], Luo et al. [56], York [49] and Cokljat et al. [81].

4.2   Casarsa's Test Case

Results of the Casarsa's test case have been presented at three different planes entitled as 1xy, 2xy and 3xy. Plane 1xy is the symmetry plane located at the center of the channel. Planes 2xy and 3xy were located 20mm and 5mm from the lateral wall respectively.
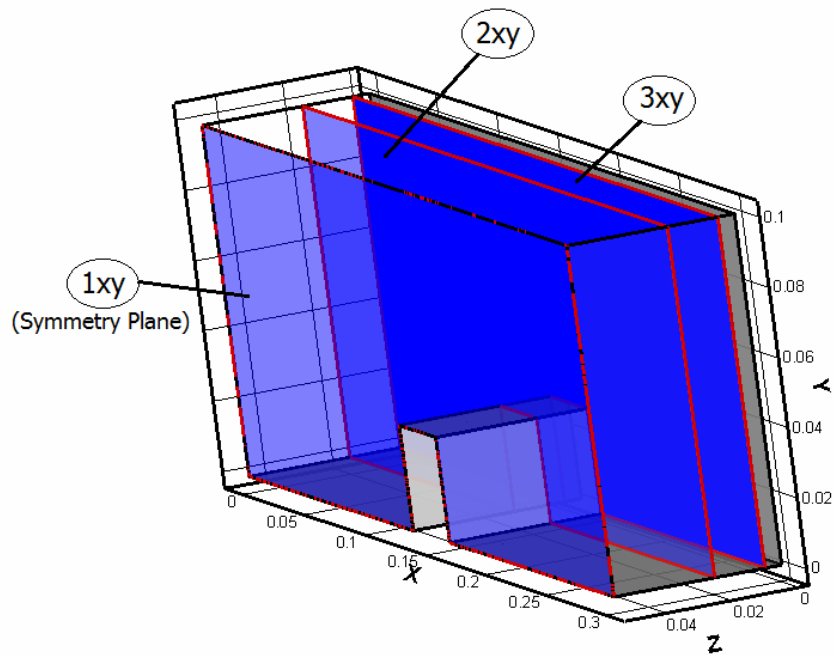
Figure 4.17. Location of the data extraction planes

Streamwise velocity component of the flow has been normalized with U_m and plotted from lower wall (rib turbulated wall) to upper wall direction. Predictions provided from employed turbulence models are compared with the experimental data obtained from PIV measurements. Findings are presented at seven different locations (x/H=-2, 0, 1, 2, 3, 4 and 5) on plane 1xy and two different locations (x/H=0 and 5) on planes 2xy and 3xy.

Predictions related with the symmetry plane are divided into two figures (Figure 4.18 and 4.19) to compare the results clearly. In Figure 4.18 even and in Figure 4.19 odd numbered locations are presented.
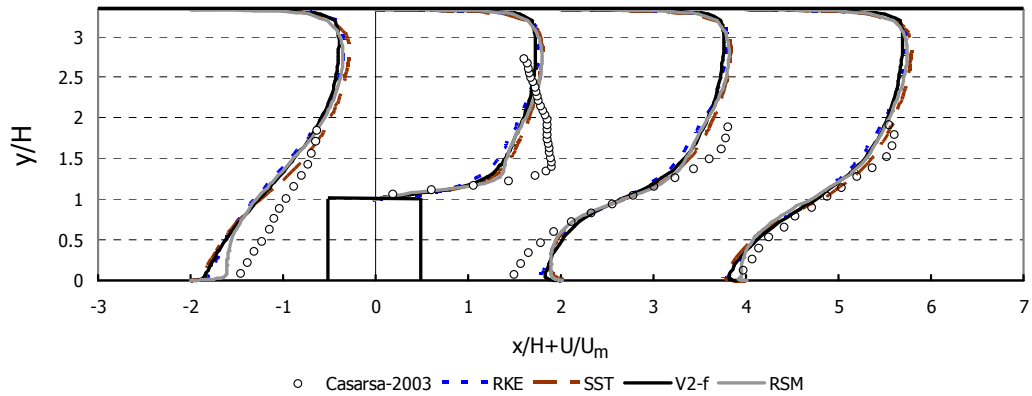
Figure 4.18. Normalized velocity profiles at 1xy plane (x/H=-2, 0, 2 and 4)
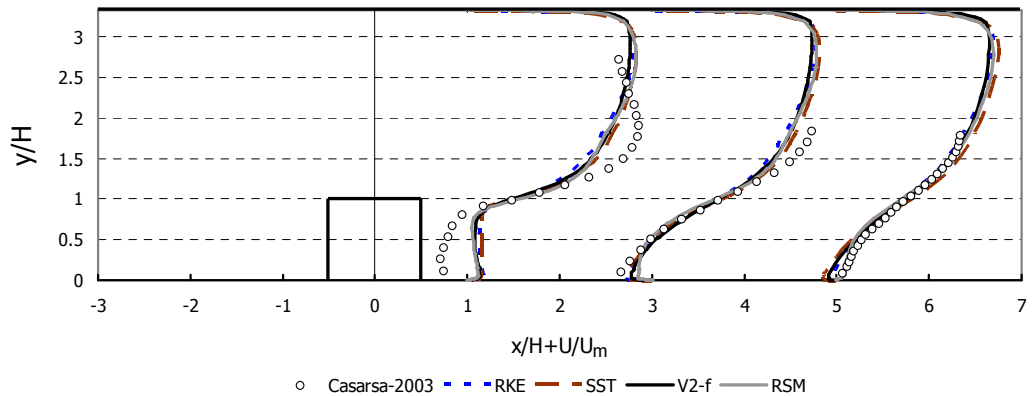
Figure 4.19. Normalized velocity profiles at 1xy plane (x/H=1, 3 and 5)

All turbulence models provided similar results at the symmetry plane and failed to resolve velocity distribution close to rib and on the rib turbulator. The flow velocity is increasing on the rib turbulator due to narrowing of the channel and having a maximum value at the middle region. Then, similar to famous backward facing step flow, separation occurs as flow passes the rib turbulator. None of the flow features described have been resolved by the turbulence models employed. There are significant differences between the predictions and the experimental data at locations x/H equal to 0, 1, 2 and -2. The location of the separation bubble just after the rib turbulator has been predicted with an hydraulic diameter offset from its actual location by all turbulence models. Velocity distribution has been predicted accurately by all turbulence models at the regions which are relatively away from rib turbulator and walls. This has been

caused from the increasing turbulence isotropy, which is basic assumption of turbulence models except RSM, close to the channel center. It should be noted that although RSM is an anisotropic turbulence model, it presented a slightly higher accuracy over other turbulence models.

Results of the 2xy and 3xy planes are given in Figure 4.20 and 4.21 respectively. The increasing effect lateral wall boundary layer can be seen in these figures. In 2xy plane, streamwise flow is nearly 15% slower than 1xy plane and increasing anisotropic turbulence effect of the lateral wall is felt.
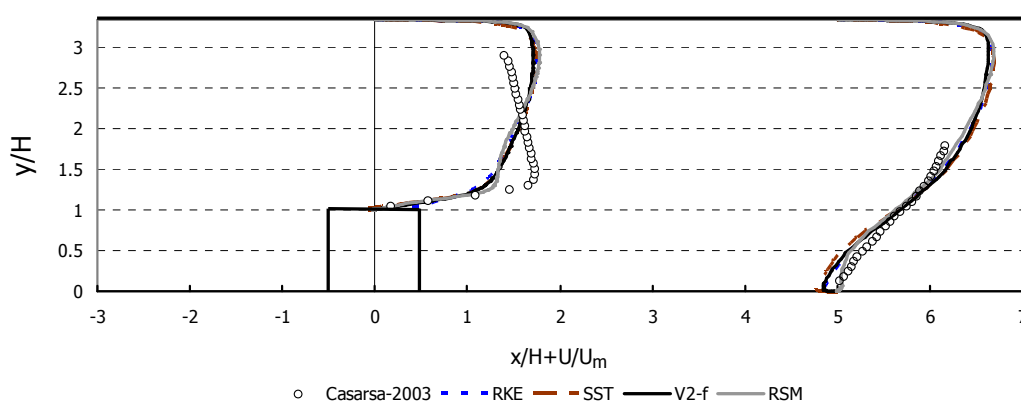
Figure 4.20. Normalized velocity profiles at 2xy plane (x/H=0 and 5)
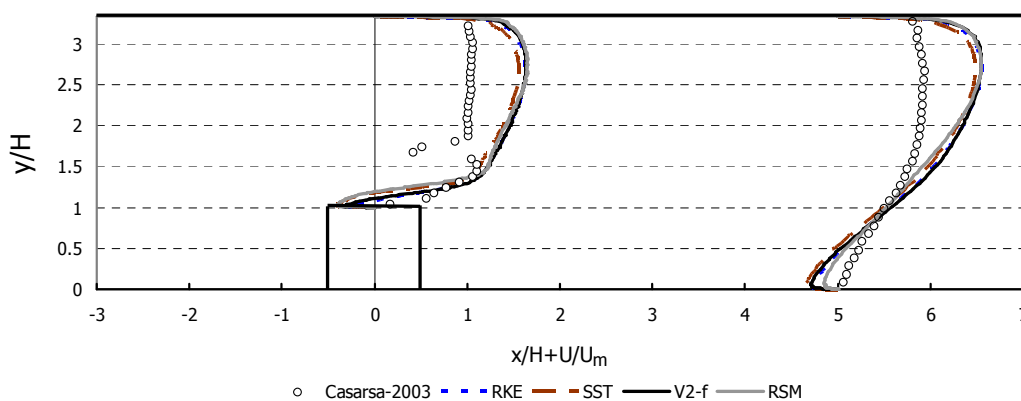
Figure 4.21. Normalized velocity profiles at 3xy plane (x/H=1 and 5)

At 3xy plane, even the x/H region predictions become highly inaccurate because of the disturbances caused from lateral wall which leads to the formation of turbulent structures. Streamwise flow is nearly 50% slower than 1xy

plane because of the highly increased effect of the lateral wall boundary layer. On the rib turbulator, PIV measurements represent some strange behaviour close to y/H=1.6 region. Casarsa [4] specified this as some background noise caused from the damages on the glass walls.

It should be noted that 30% blockage ratio is a highly extreme case for turbine internal cooling applications. Blockage ratios generally range from 6% to 15% in real turbine cooling applications and RANS based turbulence models perform much better this ratio interval. It should also be noted that obtained results were in accordance with Fransen et al. [84] and Vass [85].

4.3   Lee's Test Case

The two-pass trapezoidal smooth channel is the first test case including heat transfer in this thesis. The sensitivity of the turbulence models to the cross-section changes has been investigated in this test case. In Figure 4.22 segmental are averaged heat transfer distribution of low Reynolds number case that flow enters from smaller cross-section has been presented.
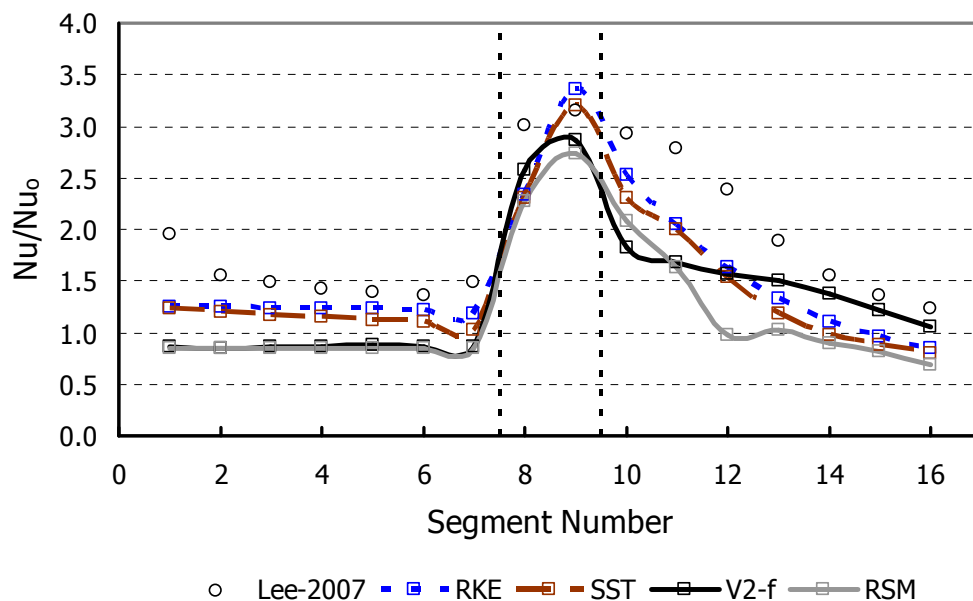
Figure 4.22. Segmental heat transfer distribution; flow entrance from smaller channel inlet, Re=16800

The experiments for air flow entering from smaller cross-section show that mean flow impinge on the endwall and secondary flow impinges on the downstream outer wall of the turn region [21]. Thus, heat transfer is high on the segments 8 and 9 which belong to turn region. All the turbulence models simulated this flow behaviour correctly but they underpredicted the heat transfer rate. Two-equation turbulence models performed much better in this flow case. Trends of V2f and RSM results were not compatible with the experiments, especially at the second pass. Maximum heat transfer location and magnitude have been accurately predicted by both RKE and SST besides the worst predictions were provided by RSM.

As the flow enters to the two-pass channel from larger cross-section, experiments showed that impingement regions move to the downstream of the turn. This is due to the higher velocity values occurring as flow enters to the smaller cross-section after turn. Thus highest heat transfer values in the two-pass channel occur in the small cross-sectioned pass, in other words on segments 9 and 10. In Figure 4.23 heat transfer distribution of low Reynolds number case that flow enters from larger cross-section has been presented.
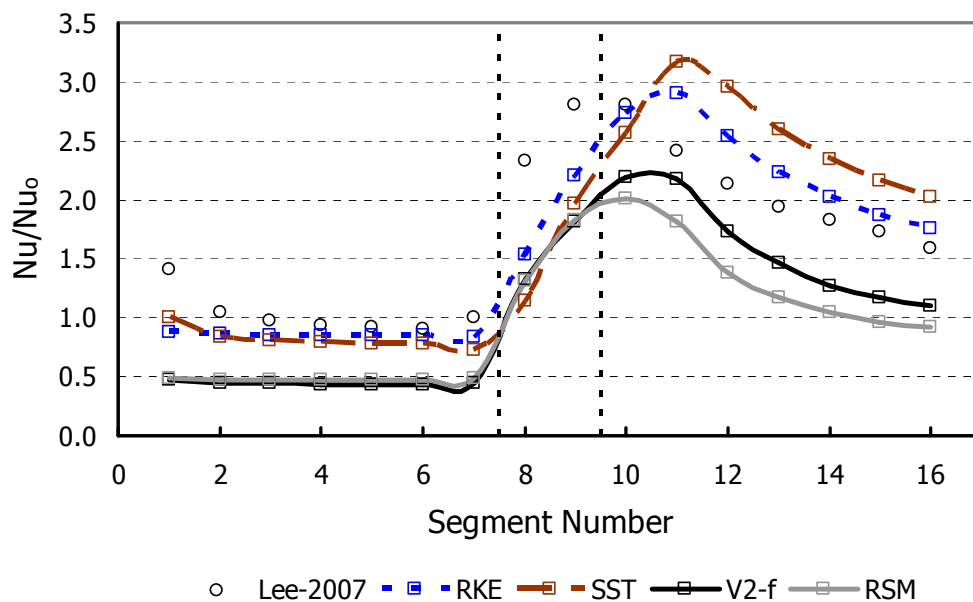
Figure 4.23. Segmental heat transfer distribution; flow entrance from larger channel inlet, Re=16800

All turbulence models sensed the cross-section difference between two channels and best predictions have been provided by RKE. However, this model slightly underpredicted the heat transfer at the large cross-sectioned (inlet) pass and highly overpredicted the same quantity at the small cross-sectioned (exit) pass. The maximum heat transfer rate prediction provided by RKE was satisfactory but it was located at segment 11 instead of 10. All turbulence models more or less provided similar shapes for heat transfer distribution and worst predictions were provided by RSM which underpredicts the heat transfer rate throughout the channel.

Finally, flow entrance from large cross-section is simulated for a large Reynolds number value and presented in Figure 4.24. Predicted Nusselt number ratios have been decreased with the increasing Reynolds number as expected. Accuracy of the results provided by the employed turbulence models was same with the previous flow case for the first pass of the channel. At the turn region and the second pass, which has a smaller cross-section, V2-f model came up with the most accurate heat transfer distribution and maximum heat transfer location predictions.
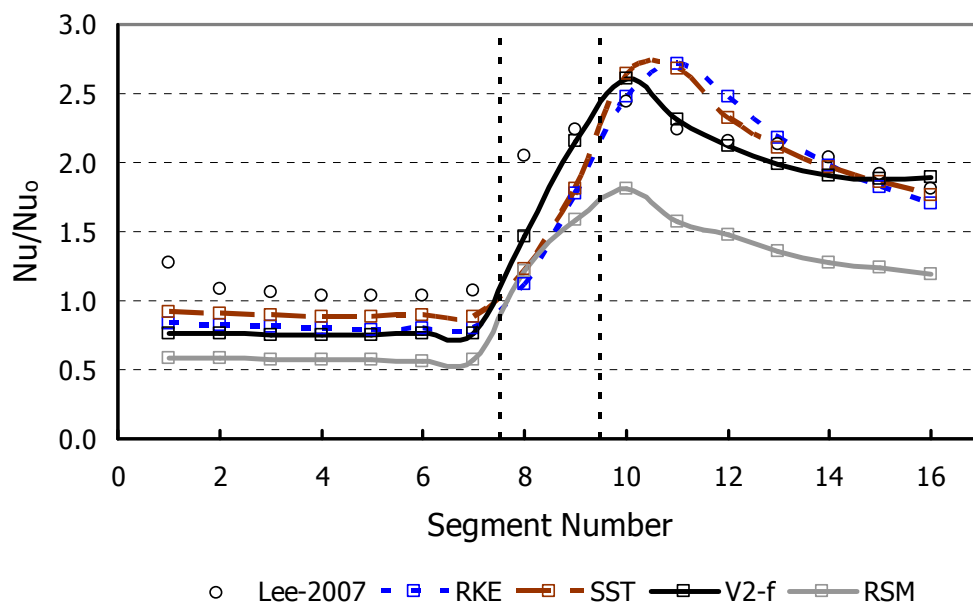
Figure 4.24. Segmental heat transfer distribution; flow entrance from larger channel inlet, Re=57200

Similar to previous flow case, RKE and SST predicted the maximum heat transfer location at segment 11 and RSM underpredicted the heat transfer rate throughout the channel and provided the worst results.

In this test case RKE and SST provided the best predictions except the last flow case. Reason of this can be defined as follows. The fully turbulent flow assumpsions used at the derivation of RKE and SST turbulence models create advantage over V2-f model and RSM. The RKE and SST turbulence models are assuming that they are always dealing with fully turbulent flows thus even at low Reynolds number simulations they predict higher heat transfer rates than other two models. This feature seems like an advantage for RKE and SST when dealing with fully turbulent wall bounded flows however it also causes poor transition prediction which will be mentioned at the last test case solved.

It should be noted that Siddique [86] obtained similar results for lower Reynolds number flow cases.

4.4   Chen's Test Case

Rib roughened channel flow has been simulated because of its being a typical configuration in modern turbine cooling applications. This test case was a combination of first three case in numerical sense. Similar to Monson's test case, geometry is strongly curved and transverse rib turbulators are included as in the Casarsa's test case. However, in this test case rib height-to-hydraulic diameter is 0.1 instead of 0.3. Finally Chen's test case is includes heat transfer similar to the Lee's test case.

Predicted segmental area averaged heat transfer distribution obtained from employed turbulence models is compared with the experimental data in Figure 4.25. All turbulence models generally captured trend of the heat transfer distribution. RKE model has the best predictions in the first pass and turn region which are highly accurate. At the second pass, RKE underpredicts the heat transfer rate and at this region of the duct, SST comes up with very accurate

results. It should be noted that at the first pass and turn regions, SST overpredicted the heat transfer rate.
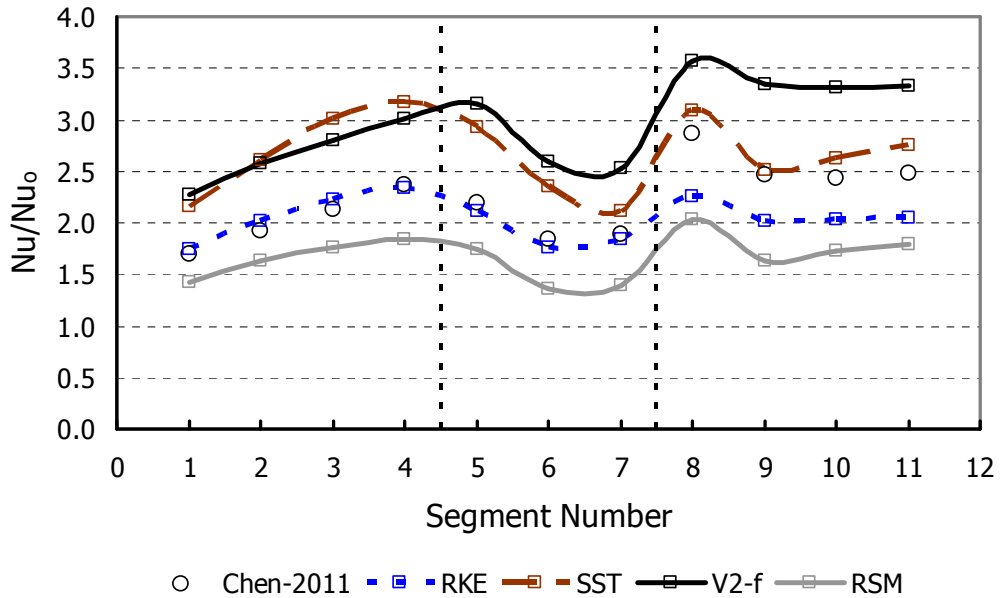
Figure 4.25. Segmental heat transfer distribution

Similar to previous test case RSM underpredicted the heat transfer throughout the channel and unlike RSM V2-f overpredicted the heat transfer at the whole flow region.

It should be noted that Chen et al. [17] also obtained very similar results for the same geometry with a different Reynolds number value, especially with SST model.

4.5   Hylton's Test Case

Conjugate heat transfer simulations have been carried out with the boundary conditions listed in Table 3.1 and 3.2. Results have been presented in terms of normalized pressure distribution, normalized surface convective heat transfer coefficient, surface friction coefficient and non-dimensional surface temperature distribution. As mentioned before two different flow cases, which

will be referred as Case 1 and Case 2, have been investigated. In both cases, convective heat transfer coefficient has been defined as follows;

$$h = \frac{q}{T_o - T_w} \tag{4.1}$$

and normalized with h_o=1135 W/m²K value. The non-dimensional temperature distribution and friction coefficient has been defined as follows;

$$\theta = \frac{T_w - T_c}{T_o - T_w} \quad \text{and} \quad C_f = \frac{F_{friction}}{1/2\,\rho U_m^2} \tag{4.2}$$

Pressure distribution has been normalized with inlet total pressure (P_o) of each flow case. All aforementioned quantities have been presented in the axial coordinates normalized with the axial chord length of 78.1558 mm.

4.5.2   Case 1 (Run 149)

Mid-span normalized pressure distribution along pressure and suction surfaces has been given in Figure 4.26.
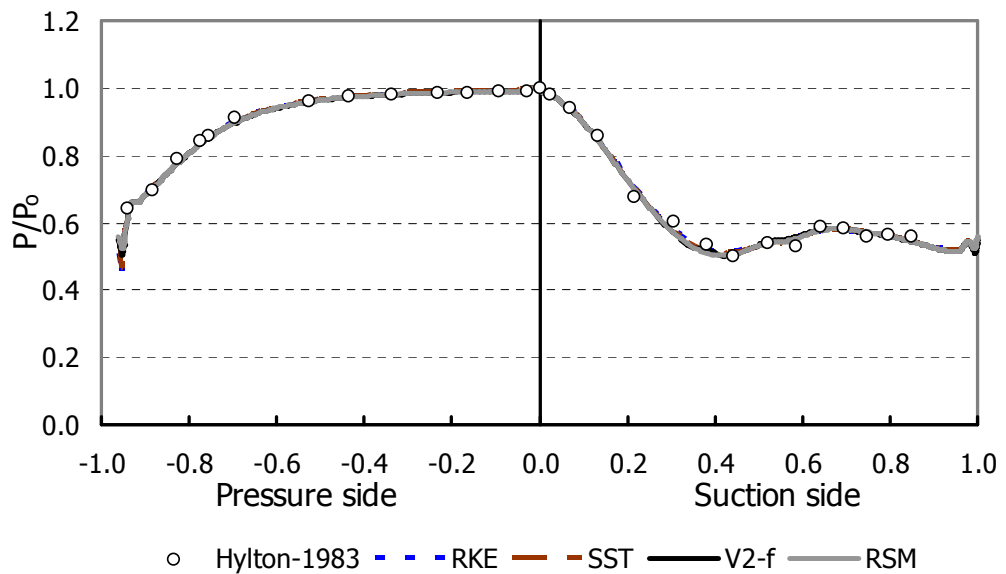
Figure 4.26. Normalized pressure distribution as function of axial chord length

According to the experiments, flow shows a sudden acceleration on the suction side and reaches to its maximum speed around 0.45 of the axial chord length. Between 0.45 and 0.7 of axial chord length, flow slightly decelerates and at the remaining portion of the suction side slightly accelerates again. All of the employed turbulence models exhibit excellent agreement with the experimental data and validated aerodynamic portion of the problem.

Normalized convective heat transfer coefficient distribution along pressure and suction surfaces has been plotted in Figure 4.27. This figure brings out very interesting clues about the capabilities of turbulence models.
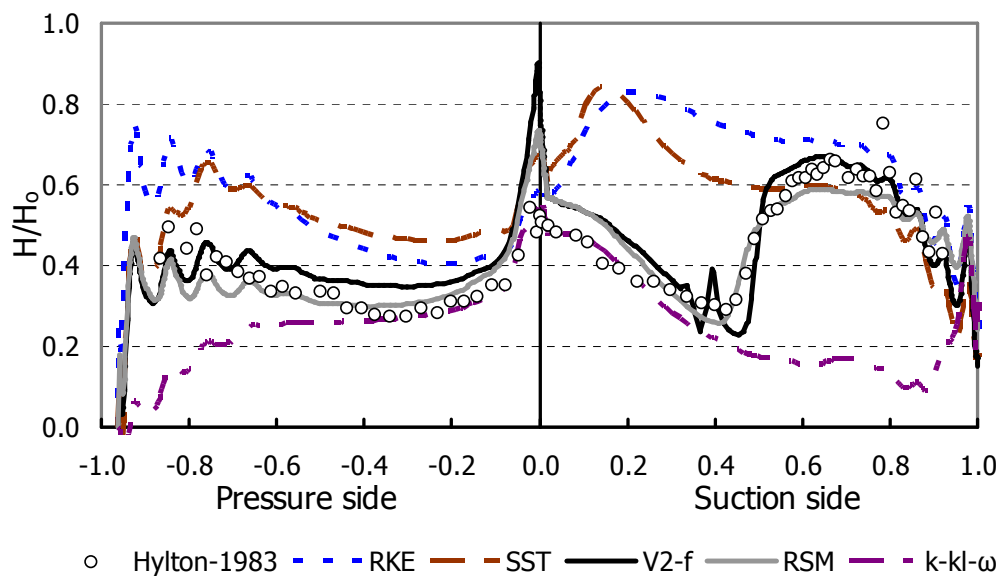
Figure 4.27. Normalized convective heat transfer coefficient distribution as function of axial chord length

As mentioned before, because of the fully turbulent flow assumptions, RKE and SST turbulence models do not recognize the laminar character of the flow close to leading edge. Therefore, RKE and SST turbulence models highly overpredicted the heat transfer coefficient until the mid region of the suction side. At the second half of the suction side flow gained its turbulent character and predictions of the RKE and SST became more accurate. On the pressure side, both turbulence models followed the trend of the experimental data with an increasing overprediction until trailing edge which indicates that these turbulence models simulating the flow further turbulent than it is in reality. Contrary to RKE

and SST, V2-f successfully resolved the boundary layer laminar-to-turbulent transition and fully turbulent region on the both sides. There was an unexpected behavior of V2-f model at the suction side, during the sudden transition of flow from laminar-to-turbulence. Similar to the Monson's test case, a non-physical turbulence, which is caused from the formulation of turbulent viscosity, has been produced. RSM provided the best heat transfer coefficient results, and accurately predicted the laminar-to-turbulent transition on both sides of the NASA C3X vane. The anisotropic characteristics of this turbulence model helped to accurately resolve both flow transition and turbulence characteristics. Predicting heat transfer coefficient on leading edge is a very important event to accurately find the possible maximum temperature values on the blade surface. As can be seen from Figure 4.27, RKE provided the most accurate leading edge heat transfer coefficient values proving that realizibility constraints, which evaluate C_μ as a flow dependent term, works perfectly.

To simulate Case 1 of Hylton's test case, three equation k-kl-ω turbulence models has also been used in addition to regular turbulence models employed. The purpose of this was examining the performance of a turbulence model which is specially designed for transition modeling. Theory of k-kl-ω turbulence model and its difference from standard k-ω turbulence model basically depends on dividing kinetic energy into turbulent and laminar kinetic energies and modeling them with separate transport equations. Leading edge heat transfer coefficient has been predicted very accurately by k-kl-ω turbulence model even better than RKE. The reason for this can be explained as follows; the k-kl-ω turbulence model also employs a flow dependent C_μ similar to RKE therefore, formation of non-physical turbulent viscosities are prevented in this model too. Obtained results were very promising in terms of modeling laminar flow regions. Especially until the 0.4 of axial chord, predictions of the k-kl-ω were even more accurate than RSM. However, transition onset has not been sensed on pressure side and until the 0.9 of axial chord on suction side. It is clear that this model would provide very accurate results after employing required tunings.

The friction coefficient distribution has been given in Figure 4.28. There is no experimental data related with friction coefficient distribution on the vane

surface however, comparison between the turbulence models would give an idea about predicted turbulence level of the flow.
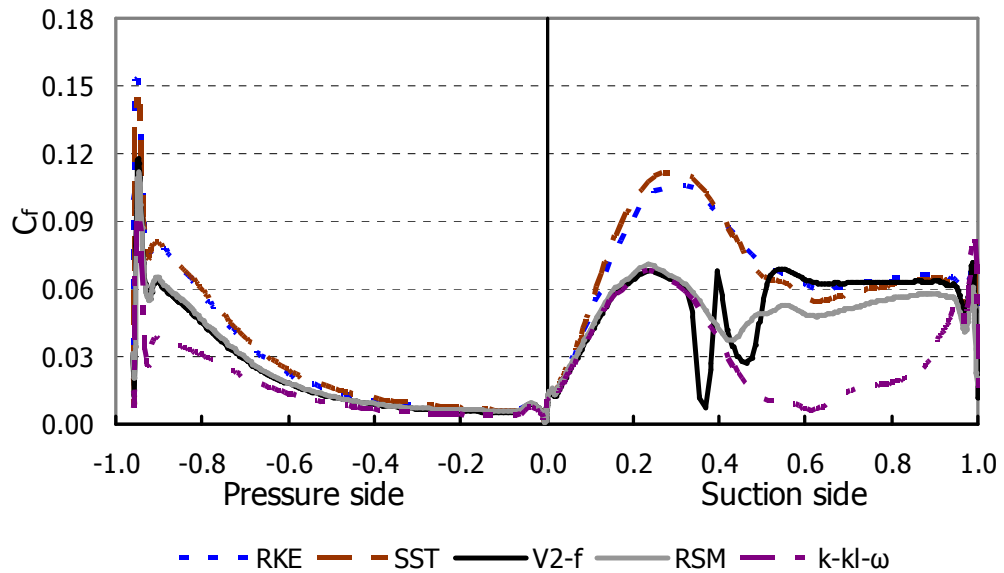
Figure 4.28. Friction coefficient distribution as function of axial chord length

Compared friction coefficient distributions are somewhat a reflection of the heat transfer coefficient distributions. Similar to Figure 4.27, RKE and SST predicted higher turbulence levels thus; friction coefficients provided by them was higher with respect to friction coefficients provided by V2-f and RSM. On the other hand, k-kl-ω turbulence model did not exhibit any turbulence so predicted the lowest friction coefficients on both sides. The insensitivity of RKE and SST to the laminar flow zone on suction side is obvious in this figure. It should be noted that the non-physical behavior of V2-f model has also been monitored at the same location of the suction side.

Mid-span non-dimensional temperature distribution has been given in Figure 4.29. Although, non-dimensional temperature is used for presentation of the results, values presented in this figure are affected from imposing same total temperature value to all cooling channel inlets. Therefore, in Figure 4.29 trends of the results provided by turbulence models are more important than the exact values predicted by them. All of the turbulence models successfully followed the experimental data at the pressure side but on the suction side only V2-f came up with predictions consistent with the experimental data.
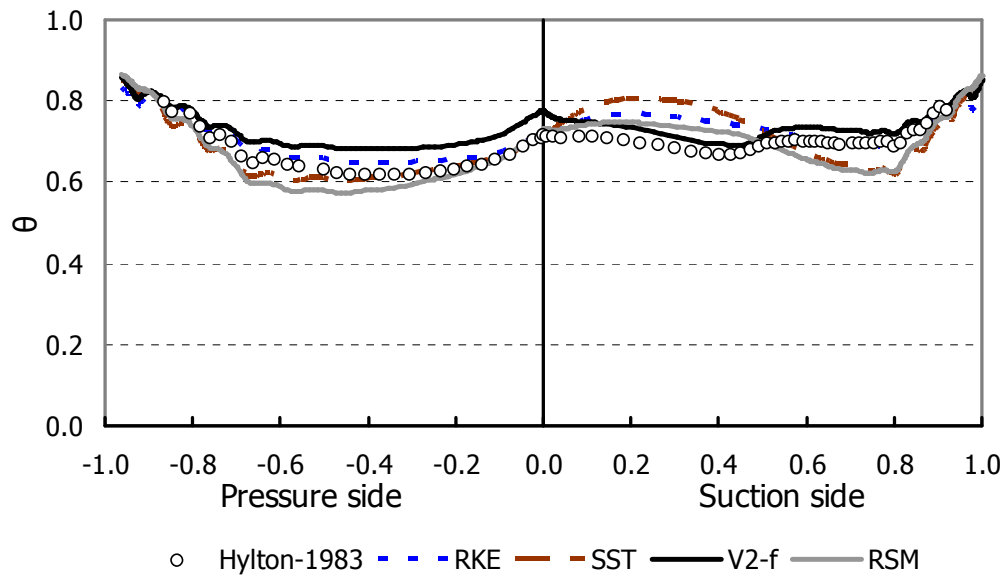
Figure 4.29. Non-dimensional temperature distribution as function of axial chord length

RKE missed the transition at the first half of the suction side as expected yet provided the most accurate predictions at the turbulent portion. SST also missed the transition with a much higher error with respect to RKE moreover; results of the fully turbulent flow were also inaccurate. RSM followed a very similar trend with SST throughout the suction side but its predictions on the transition region exhibit much less error than both SST and RKE. V2-f provided the best estimations on the suction side of the blade by flawlessly following the trend of the experimental data.

4.5.3   Case 2 (Run 155)

As mentioned before, two distinct flow conditions have been chosen for conjugate heat transfer simulations to clearly evaluate the success of the employed turbulence models. The normalized pressure distribution along pressure and suction surfaces has been given in Figure 4.30. Experiments show that flow is experiencing very similar velocity changes along the cascade passage where only difference is the shock formation occurring on the suction side of the

NASA C3X vane around 0.6 of the axial chord. Because of the shock formation flow experiences a sudden deceleration at this region.
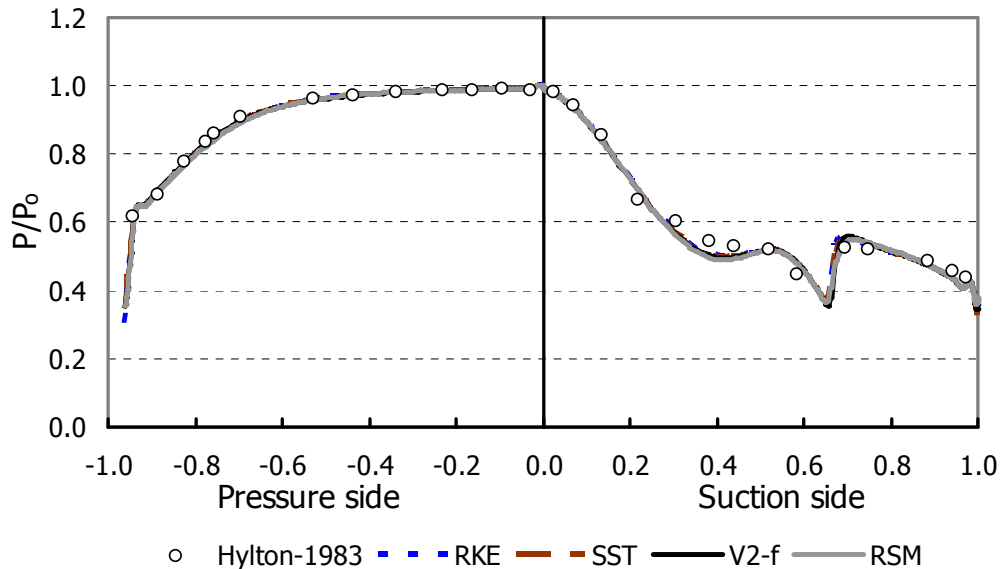
Figure 4.30. Normalized pressure distribution as function of axial chord length

All of the employed turbulence models provided excellent agreement with the experimental pressure distribution and location of the shock wave.

Normalized convective heat transfer coefficient distribution along pressure and suction surfaces has been plotted in Figure 4.31. Values are elevated on all regions with respect to the previous case and trend in the pressure side remained similar in two cases. However, distribution on suction side has some differences at Case 2 because this side of the NASA C3X vane is experiencing a shock wave and a much slower boundary layer laminar-to-turbulent transition. Similar to Case 1 RKE and SST overestimated the heat transfer coefficients on pressure side but their trends are in accordance with the experimental data. V2-f provided better results at this region and RSM came up with the best predictions. On suction side, level of accuracy decreased for all turbulence models. RKE and SST once again missed the laminar region between leading edge to 0.3 of the axial chord length but provided better predictions at the remaining portion of the suction side. RSM resolved the boundary layer laminar-to-turbulent transition better than RKE and SST but there was an offset between the predicted and

measured values along the vane. Best predictions are provided by V2-f at the laminar and turbulent regions.
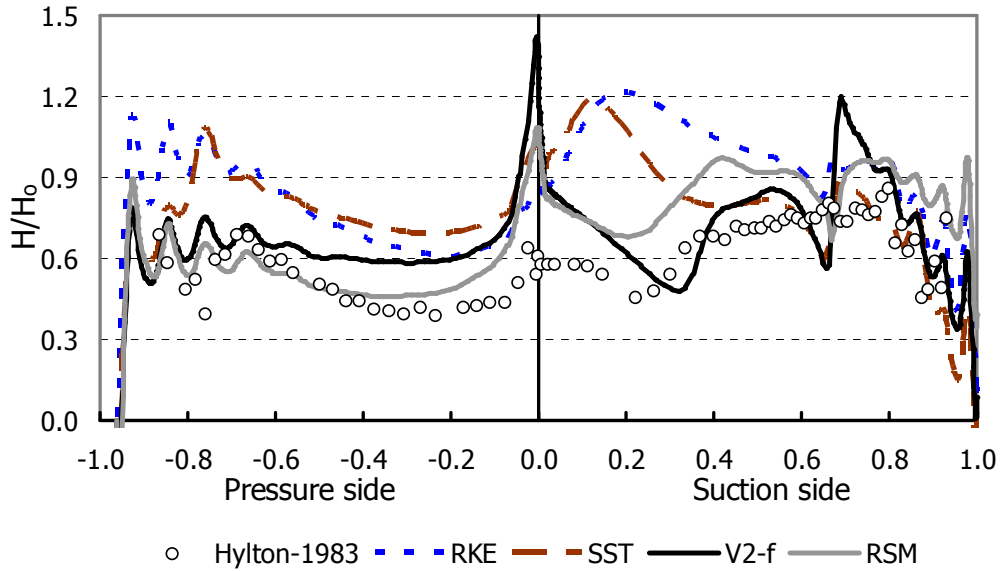
Figure 4.31. Normalized convective heat transfer coefficient distribution as function of axial chord length

In the experimental heat transfer coefficient data, there was no evidence of the shock wave. However, V2-f and SST overreacted to the shock formation. RSM and RKE also showed decrease of heat transfer coefficient at this region. Once more RKE came up with the best leading edge heat transfer coefficient estimations.

Convective heat transfer coefficient distribution has ripples close to the trailing edge at both cases. These ripples also exist in the experimental data and to understand the cause of this phenomenon one should examine heat transfer coefficient equation. The heat transfer coefficient in a conjugate analysis can be calculated by equating the convective and conductive heat transfer. The equation of heat transfer on the vane surface in one dimension can be given as;

$$- \kappa \frac{\partial}{\partial y} (T - T_w) \big|_{y=0} = h (T_w - T_\infty) \qquad (4.3)$$

Towards the trailing edge NASA C3X vane naturally becomes thinner and so cooling holes become very close to the vane surface at this region. As a result

of this, effect of the cooling holes is highly sensed on the blade surface causing sudden variations in thermal boundary layer gradients and wall temperatures. Variations in these two terms, which are employed in equation 4.3, are the reason of the ripples observed at convective heat transfer coefficient distribution of both cases solved.

Friction coefficient distribution of Case 2 has been given in Figure 4.28. Results plotted in this figure confirm the heat transfer coefficient findings.
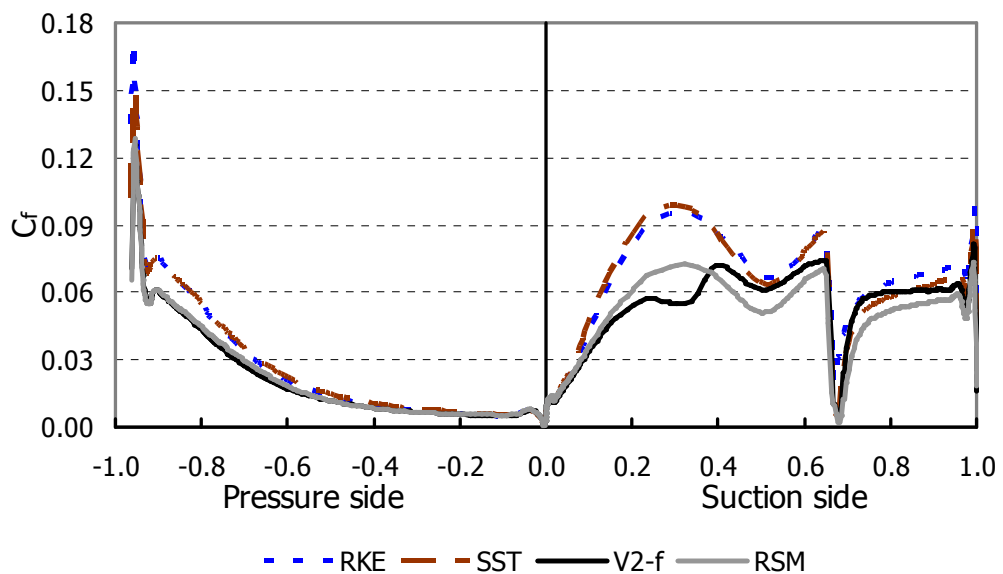
Figure 4.32. Friction coefficient distribution as function of axial chord length

RKE and SST once again predicted higher turbulence levels than V2-f and RSM on pressure side until the trailing edge. On the suction side laminar flow zone is missed by RKE and SST one more time but unlike first case, V2-f did not show any non-physical turbulence production. This should be caused from the slow laminar-to-turbulence flow transition experienced in Case2. It should be also noted that all of the turbulence models gave very similar predictions at the shock wave location.

Non-dimensional temperature distribution has been given in Figure 4.33. It is reminded that for comparison of this quantity, trends of the results provided by turbulence models are more important than the exact values predicted by them. As can be seen from Figure 4.33, all of the turbulence models were in

accordance with the experimental data on pressure side. RKE provided the best predictions on this side of NASA C3X vane.
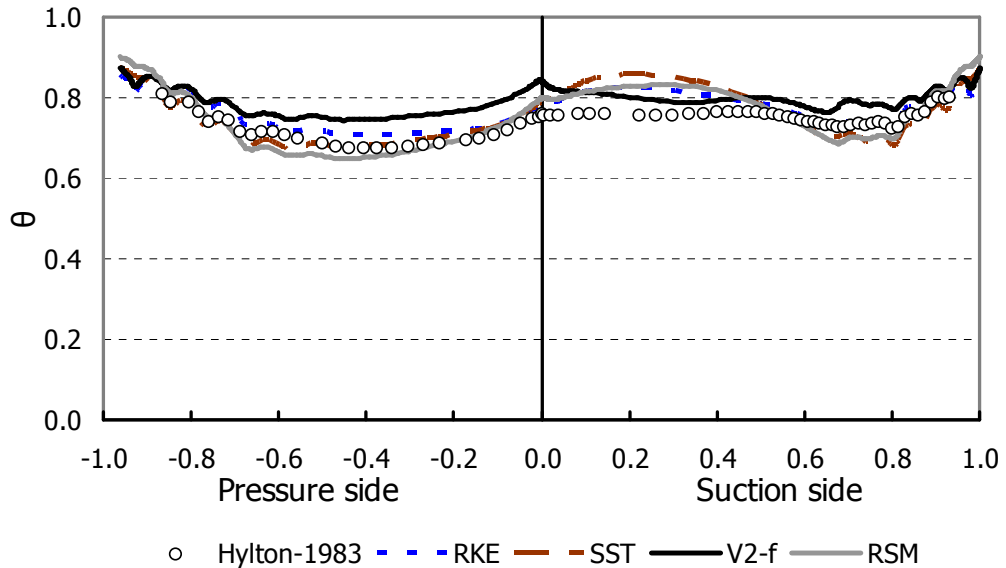
Figure 4.33. Non-dimensional temperature distribution as function of axial chord length

On suction side all turbulence models provided better accuracy with respect to previous flow case solved. Similar to the first case, RKE missed the laminar-to-turbulence transition at the first half of the suction side and then provided most accurate predictions on the remaining portion. SST also missed the boundary layer transition with a higher error with respect to RKE but predictions provided at the turbulent portion improved with respect to the previous case. RSM has overpredicted the transition with similar error level with RKE and then provided almost same results with SST at the turbulent region. Only V2-f captured boundary layer laminar-to-turbulence transition occurring on the suction side of the NASA C3X vane and nicely followed the trend of the experimental data at the remaining portion.

It was interesting that even though V2-f and RSM provided the best overall prediction performance, the worst leading edge estimations are also provided by these two turbulence models in both conjugate heat transfer problems solved.

It should be noted that aforementioned studies of York [49], Facchini et al. [50], Ledezma et al. [52], Peigang et al. [53] and Luo et al. [54] obtained very similar turbulence model performances for different boundary conditions.

CHAPTER 5

CONCLUSIONS

5.1   General Conclusions

The main objective of this thesis is to present the predictive capabilities of the RANS based turbulence models on flow problems related with different internal turbine cooling strategies. Presenting the theory and different versions of V2-f model and comparing its applicability to various flow types is also aimed. In this extent five test cases have been examined

Strongly curved flow in a U-duct has been investigated first, because modern cooling schemes frequently make use of this geometry. Conducted simulations showed that none of the turbulence models were superior to each other at both Reynolds number values. V2-f revealed non-physical results at some flow conditions as mentioned at the theory of the model.

Rib roughened channel flow has been investigated in the second place, because rib turbulators are also very important instruments for the internal cooling strategies. This test case also did not reveal any superiority between turbulence models employed. In fact predictions of all turbulence models were very similar to each other so that at close regions to the rib turbulator all of them were unsuccessful at the same level and as farther regions were examined accuracy was increasing.

Smooth trapezoidal two-pass cooling channel has been studied in third place because realistic cooling schemes generally have this channel shape.

Generally RKE and SST exhibited better agreements with the experimental data on both flow directions and Reynolds number values.

Two-pass cooling channel with angled rib turbulators has been simulated to see the success of the turbulence models against the combination of previously studied three cases. RKE came up with the best predictions at first pass and turn region and SST came up with the best predictions at second pass. It is suggested that the success of the two-equation turbulence models at last two geometries is strongly related with their fully turbulent assumptions.

The last case was the conjugate heat transfer analysis of a turbine vane internally cooled with radial channels. Most distinguishing results between employed turbulence models have been obtained from this test case. Conducted simulations revealed that V2-f model was superior to two-equation turbulence models in predicting thermal quantities and comparable with RSM. However, non-physical predictions of V2-f were encountered in this test case too. Results also showed that k-kl-ω transition model would be a very effective tool in predicting thermal quantities if the required modifications done and RKE has very effective realizibility constraints.

The overall observation the study indicates that the success of two-equation turbulence models on different turbine cooling test cases were unpredictable. However, except a few unreasonable predictions, V2-f showed a standard performance in all test cases. Even if the best agreement with the experiments was not provided by V2-f in all test cases, its predictions were satisfactory and useful at least for a reliable first guess.

The performance of the turbulence models should also be investigated in terms of convergent character. The conducted simulations revealed a well known fact one more time that RKE has the best convergent character among all turbulence models employed. V2-f has also has a very strong convergent character. Although it operates with four equations, the simplicity of the model makes its convergent character comparable with SST. Among all turbulence models employed RSM and k-kl-ω have the worst convergent character. RSM has a very strong coupling between momentum equations and Reynolds stresses so in all simulations conducted, turbulence quantities have been kept at first order

discretization level. Especially at the batch run applications, RSM was unpredictable and even divergent. These experiences indicate that V2-f is a very good choice for conjugate heat transfer simulations.

5.2   Recommendations for Future Work

In this thesis, only the stationary geometries have been studied with steady-state RANS based turbulence models. The recommendations for the future works of this study can be listed as follows.

- Single type of unstructured grid formed by tetrahedral and prism cells has been used in this thesis. Effect of the mesh types to the solution can be investigated.

- As mentioned in the theory of the V2-f model, new solutions have been proposed to improve the model. The capabilities of the V2-f can be improved by applying these suggestions.

- Turbulence models like V2-f and k-kl-ω can be tuned for improving their conjugate heat transfer simulation capabilities.

- This study revealed that steady-state simulations have limited success for strongly curved and rib turbulated channel flow. The unsteady analysis opportunities like DES and LES can be studied for this kind of flows.

- External cooling is a very important tool for modern turbine cooling applications so addition and optimization of external cooling strategies to the so far conducted internal cooling studies can be investigated.

REFERENCES

1. **Han, J.C., Dutta, S. and Ekkad, S.V.** *Gas Turbine Heat Transfer and Cooling Technology*, Taylor & Francis Group, New York, 2000.

2. **Iacovides, H. and Launder, B.E.** *Internal Blade Cooling: The Cinderella of Computational and Experimantal Fluid Dynamics Research in Gas Turbines*, Proceedings of the Institution of Mechanical Engineers, Part A: Journal of Power and Energy, vol. 221, pp. 265-290, 2007.

3. **Tanda, G. and Cavallero, D.** *Heat Transfer Coefficient Measurements in Ribbed Channels Using Liquid Crystal Thermography*, The 10th International Symposium on Flow Visualization, Kyoto, Japan, 2002.

4. **Casarsa, L.** *Aerodynamic Performance Investigation of a Fixed Rib-Roughened Internal Cooling Passage*, Doctoral Dissertation, Dipartimento di Energetica e Macchine, Universita degli Studi di Udine, 2003.

5. **Liu, H.** *An Experimental Investigation of the Wall Surface Averaged Heat Transfer Coefficient in a Square Channel Roughened with 45° Staggered Round Corner Ribs*, M.S. Thesis, The Department of Mechanical, Industrial and Manufacturing Engineering, Northeastern University, 2002.

6. **Liu, Y.H.** *Heat Transfer in Leading and Trailing Edge Cooling Channels of the Turbine Blade Under High Rotation*, Doctoral Dissertation, Department of Mechanical Engineering, Texas A&M University, 2008.

7. **Schueren, S., Hoefler, F., von Wolfersdorf, J. and Naik, S.** *Heat Transfer in an Oblique Jet Impingement Configuration with VaryingJet Geometries*, ASME Paper No. GT2011-45169, 2011.

8. **Wang, L., Sunden, B., Borg, A. and Abrahamsson, H.** *Heat Transfer in a Channel Under Effects of a Shallow-Angle Jet Impingement and a Rib*, ASME Paper No. GT2011-46333, 2011.

9. **Gao, L.** *Effect of Jet Hole Arrays Arrengement on Impingement Heat Transfer*, M.S. Thesis, The Department of Mechanical Engineering, Louisiana State University, 2003.

10. **Jordan, C.N. and Wright, L.M.** *Heat Transfer Enhancement in a Rectangular (AR=3:1) Channel with V-Shaped Dimples*, ASME Paper No. GT2011-46128, 2011.

11. **Tran, L.V., et al.** *PIV Study on the Dimple Mid-Plane of a Narrow Rectengular Channel with Dimples Applied to One Wall*, ASME Paper No. GT2011-46132, 2011.

12. **Zhou, F.** *Studies on the Heat/Mass Transfer Characteristics and Fluid Structure in a Square Internal Cooling Channel With Dimpled Surfaces*, M.S. Thesis, The Department of Mechanical Engineering, Louisiana State University, 2007.

13. **Monson, D.J. and Seegmiller, H.L.** *An Experimental Investigation of Subsonic Flow in a Two-Dimensional U-Duct*, NASA-TM-103931, 1992.

14. **Liou, T.M., Chen, C.C., Tzeng, Y.Y. and Tsai, T.W.** *Non-Intrusive Measurements of Near-Wall Fluid Flow and Surface Heat Transfer in a Serpentine Passage*, International Journal of Heat and Mass Transfer, vol. 43, pp. 3233-3244, 2000.

15. **Iacovides, H., et al.** *Experiments on Local Heat Transfer in a Rotating Square-Ended U-Bend*, International Journal of Heat and Fluid Flow, vol. 20, pp. 302-310, 1999.

16. **Liou, T.M., Chen, C.C. and Chen, M.Y.** *TLCT and LDV Measurements of Heat Transfer and Fluid Flow in a Rotating Sharp turning Duct*, International Journal of Heat and Mass Transfer, vol. 44, pp. 1777-1787, 2001.

17. **Chen, W., Ren, J. and Jiang, H.** *Effect of Turning Vane Configurations on Heat Transfer and Pressure Drop in a Ribbed Internal Cooling System*, Journal of Turbomachinery, vol. 133, 041012, 2011.

18. **Mochizuki, S., Murata, A., Shibata, R. and Yang, W.-J.** *Detailed Measurements of Local Heat Transfer Coefficients in Turbulent Flow Through Smooth and Rib-Roughened Serpentine Passages with a 180^{0} Sharp Bend*, International Journal of Heat and Mass Transfer, vol. 42, pp. 1925-1934, 1999.

19. **Han, J.C., Chandra, P.R. and Lau, S.C.** *Local Heat/Mass Transfer Distributions Around Sharp 180 Deg Turns in Two-Pass Smooth and Rib-Roughened Channels*, Journal of Heat Transfer, vol. 110, pp. 91-98, 1988.

20. **Ekkad, S.V. and Han, J.C.** *Detailed Heat Transfer Distributions in Two-Pass Square Channels with Rib Turbulators*, Int. J. Heat Mass Transfer, vol. 40, no. 11, pp. 2525-2537, 1997.

21. **Lee, S.W.** *Heat Transfer Characteristics of a Two-Pass Trapezoidal Channel and a Novel Heat Pipe*, Doctoral Dissertation, Department of Mechanical Engineering, Texas A&M University, 2007.

22. **Liou, T.M., Chen, M.Y. and Tsai, M.H.** *Fluid Flow and Heat Transfer in a Rotating Two-Pass Square Ductwith In-Line 90-Deg Ribs*, Journal of Turbomachinery, vol. 124, pp. 260-268, 2002.

23. **Liou, T.M. and Dai, G.Y.** *Pressure and flow Characteristics in a Rotating Two-PassSquare Duct with 45-Deg Angled*, Journal of Turbomachinery, vol. 126, pp. 212-219, 2004.

24. **Agarwal, P.** *Heat/Mass Transfer in Smooth and Ribbed Rectangular Serpentine Passages of Different Aspect Ratio's and Orientation*, M.S. Thesis, The Department of Mechanical Engineering, Louisiana State University, 2004.

25. **Huh, M.** *Heat Transfer in Smooth and Ribbed Rectangular Two-Pass Channels with a Developing Flow Entrance at High Rotation Numbers*, Doctoral Dissertation, Department of Mechanical Engineering, Texas A&M University, 2009.

26. **Fu, W.L.** *Aspect Ratio Effect on Heat Transfer in Rotating Two-Pass Rectangular Channels with Smooth Walls and Ribbed Walls*, Doctoral Dissertation, Department of Mechanical Engineering, Texas A&M University, 2005.

27. **Liu, Y.H.** *Effect of Rib Spacing on Heat Transfer and Friction in a Rotating Two-Pass Rectangular (AR=1:2) Channel*, M.S. Thesis, Department of Mechanical Engineering, Texas A&M University, 2005.

28. **Hylton, L.D., et al.** *Analytical and Experimental Evaluation of the Heat Transfer Distribution Over the Surface of Turbine Vanes*, NASA-CR-168015, 1983.

29. **Dees, J.E.** *Experimental Measurements of Conjugate Heat transfer on a Scaled up Gas Turbine Airfoil with Realistic Cooling Configuration*, Doctoral Dissertation, Department of Mechanical Engineering, The University of Texas at Austin, 2010.

30. **Davidson, F.T., Dees, J.E. and Bogard, D.G.** *An Experimental Study of Thermal Barrier Coatings and Film Cooling on an Internally Cooled Simulated Turbine Vane*, ASME Paper No. GT2011-46604, 2011.

31. **Patil, S. and Tafti, D.** *Large-Eddy Simulation with Zonal Near Wall Treatment of Flow and Heat Transfer in a Ribbed Duct for the Internal Cooling of Turbine Blades*, ASME Paper No. GT2011-45749, 2011.

32. **Tafti, D.K.** *Large-Eddy Simulations of Heat Transfer in a Ribbed Channel for Internal Cooling of Turbine Blades*, ASME Paper No. GT2003-38122, 2003.

33. **Abdel-Wahab, S.** *Large Eddy Simulations of Flow and Heat Transfer in a Staggered 45° Ribbed Duct and a Rotating 90° Ribbed Duct*, M.S. Thesis, Department of Mechanical Engineering, Virginia Polytechnic Institute and State University, 2003.

34. **Sewall, E.A. and Tafti, D.K.** *Large Eddy Simulation of the Developing Region of a Staionary Ribbed Internal Turbine Blade Cooling Channel*, ASME Paper No. GT2004-53832, 2004.

35. **Sewall, E.A. and Tafti, D.K.** *Large Eddy Simulation of Flow and Heat Transfer in the 180° Bend Region of a Staionary Ribbed Gas Turbine Internal Cooling Duct*, ASME Paper No. GT2005-68518, 2005.

36. **Viswanathan, A.K.** *Detached Eddy Simulation of Turbulent Flow and Heat Transfer in Turbine Blade Internal Cooling Ducts*, Doctoral Dissertation, Department of Mechanical Engineering, Virginia Polytechnic Institute and State University, 2006.

37. **Saha, A.K. and Acharya, S.** *Flow and Heat Transfer in an Internally Ribbed Duct with Rotation: An Assessment of LES and URANS*, ASME Paper No. GT2003-38619, 2003.

38. **Jang, Y.J., Chen, H.C. and Han, J.C.** *Computation of Flow and Heat Transfer in Two-Pass Channels with 60 Deg Ribs*, Journal of Heat Transfer, vol. 123, pp. 563-575, 2001.

39. **Al-Qahtani, M., Chen, H.C. and Han, J.C.** *A Numerical Study of Flow and Heat Transfer in Rotating Rectangular Channels (AR=4) with 45° Rib Turbulators by Reynolds Stress Turbulence Model*, ASME Paper No. GT2002-30216, 2002.

40. **Rokni, M. and Gatski, T.B.** *Predicting Turbulent Convective Heat Transfer in Three-Dimensional Duct Flows*, NASA/TM-1999-209843, 1999.

41. **Rumsey, L.C., Gatski, T.B. and Morrison, J.H.** *Turbulence Model Predictions of Extra-Strain Rate Effects in Strongly-Curved Flowsredicting Turbulent Convective Heat Transfer in Three-Dimensional Duct Flows*, AIAA 99-0157, 1999.

42. **Sleiti, A.K.** *Effect of Coriolis and Centrifugal Forces on Turbulence and Transport at High Rotation and Buoyancy Numbers*, Doctoral Dissertation, Department of Mechanical, Materials and Aerospace Engineering, University of Central Florida, 2004.

43. **Su, G.** *Numerical Simulation of Flow and Heat Transfer of Internal Cooling Passage in Gas Turbine Blade*, Doctoral Dissertation, Department of Mechanical Engineering, Texas A&M University, 2005.

44. **York, W.D., Holloway, D.S. and Leylek, J.H.** *Prediction of Heat Transfer in a Ribbed Channel: Evaluation of Unsteady RANS Methodology*, ASME Paper No. GT2005-68821, 2005.

45. **Saha, A.K. and Acharya, S.** *Unsteady RANS Simulation of Turbulent Flow and Heat Transfer in Ribbed Coolant Pssages of Different Aspect Ratios*, ASME Paper No. GT2004-53986, 2004.

46. **Bohn, D.E. and Tümmers, C.** *Numerical 3-D Conjugate Flow and Heat Transfer Investigation of a Transonic Convection-Cooled Thermal Brrier Coated Turbine Guide Vane with Reduced Cooling Fluid Mass Flow*, ASME Paper No. GT2003-38431, 2003.

47. **Rahman, F.** *Numerical Modeling of Heat Transfer and Thermal Stresses in Gas Turbine Guide Vanes*, M.E. Thesis, Department of Mechanical and Aeronautical Engineering, University of Pretoria, 2003.

48. **Mangesh, A.K.** *Study of Gas Turbine Blade Conjugate Heat Transfer to Determine Blade Temperatures*, M.E. Thesis, Department of Mechanical Engineering, Pennsylvania State University, 2009.

49. **York, W.D.** *A Robust Conjugate Heat Transfer Methodology with Novel Turbulence Modeling Applied to Internally-Cooled Gas Turbine Airfoils*, Doctoral Dissertation, Department of Mechanical Engineering, Clemson University, 2006.

50. **Facchini, B., Magi, A. and Scotti Del Greco, A.** *Conjugate Heat Transfer Simulation of a Radially Cooled Gas Turbine Vane*, ASME Paper No. GT2004-54213, 2004.

51. **Findlay, J.P.** *3-D Conjugate Heat Transfer Analysis of a Cooled Transonic Turbine Blade Using Non-Reflecting Boundary Conditions*, M.E. Thesis, Department of Mechanical Engineering, McGill University, 2005.

52. **Ledezma, G.A., Laskowski, G.M. and Tolpadi, A.K.** *Turbulence Model Assessment for Conjugate Heat Transfer in a High Pressure Turbine Vane Model*, ASME Paper No. GT2008-50498, 2008.

53. **Peigang, Y., Zhenfeng, W. and Wanjin, H.** *Conjugate Heat Transfer Numerical Validation and PSE Analysis of Transonic Internally-Cooled Turbine Cascade*, ASME Paper No. GT2010-23251, 2010.

54. **Luo, J. and Razinsky, E.H.** *Conjugate Heat Transfer Analysis of a Cooled Turbine Vane Using the V2F Turbulence Model*, Journal of Turbomachinery, vol. 129, pp. 773-781, 2007.

55. **Mangani, L., Cerutti, M., Maritano, M. and Spel, M.** *Conjugate Heat Transfer Analysis of NASA C3X Film Cooled Vane with an Object-Oriented CFD Code*, ASME Paper No. GT2010-23458, 2010.

56. **Luo, J. and Razinsky, E.H.** *Analysis of Turbulent Flow in 180 Deg Turning Ducts with and without Guide Vanes*, Journal of Turbomachinery, vol. 131, 021011, 2009.

57. **Luo, J. and Razinsky, E.H.** *Prediction of Heat Transfer and Flow Transition on Transonic Turbine Airfoils Under High Freestream Turbulence*, ASME Paper No. GT2008-50868, 2008.

58. **Takahashi, T., et al.** *Assessment of URANS and DES for Prediction of Leading Edge Film Cooling*, Journal of Turbomachinery, vol. 134, 031008, 2012.

59. **Blazek, J.** *Computational Fluid Dynamics: Principles and Applications*, Elsevier, Amsterdam, 2001.

60. **Hoffmann, K.A. and Chiang, S.J.** *Computational Fluid Dynamics Volume I*, 4th Edition, Engineering Education System, Kansas, 2000.

61. **Hoffmann, K.A. and Chiang, S.J.** *Computational Fluid Dynamics Volume II*, 4th Edition, Engineering Education System, Kansas, 2000.

62. **Hoffmann, K.A. and Chiang, S.J.** *Computational Fluid Dynamics Volume III*, 4th Edition, Engineering Education System, Kansas, 2000.

63. *ANSYS FLUENT 13.0 Theory Guide*, ANSYS Inc., 2010.

64. *ANSYS FLUENT 12.0 V^2-f Turbulence Model Manual*, ANSYS Inc., 2009.

65. **Durbin, P.A.** *Near-Wall Turbulence Closure Modeling without 'Damping Functions'*, Theoretical and Computational Fluid Dynamics, vol. 3, pp. 1-13, 1991.

66. **Durbin, P.A.** *Separated Flow Computations with the k-ε-$\overline{v^2}$ Model*, AIAA Journal, vol. 33, pp. 659-664, 1995.

67. **Durbin, P.A.** *On the k-ε Stagnation Point Anomaly*, International Journal of Heat and Fluid Flow, vol. 17, pp. 89-90, 1996.

68. **Lien, F.-S. and Kalitzin, G.** *Computations of Transonic Flow with the $\overline{v^2}$-f Turbulence Model*, International Journal of Heat and Fluid Flow, vol. 22, pp. 53-61, 2001.

69. **Parneix, S. and Durbin, P.A.** *Numerical Simulation of 3D Turbulent Boundary Layers Using the V2F Model*, Annual Research Briefs, Center for Turbulence Research, NASA Ames/Stanford University, pp. 135-148, 1997.

70. **Davidson, L., Nielsen, P.V. and Sveningsson, A.** *Modifications of the $\overline{v^2}$-f Model for Computing the Flow in a 3D Wall Jet*, Proceedings of the 4th International Symposium on Turbulence, Heat and Mass Transfer, pp. 577-584, 2003.

71. **Sveningsson, A.** *Analysis of the Performance of Different $\overline{v^2}$-f Turbulence Models in a Stator Vane Passage Flow*, Licentiate Thesis, Department of Thermo and Fluid Dynamics, Chalmers University of Technology, 2003.

72. **Iaccarino, G.** *Predictions of a Turbulent Separated Flow Using Commercial CFD Codes*, Journal of Fluids Engineering, vol. 123, pp. 819-828, 2001.

73. **El-Behery, S. and Hamed, M.H.** *A Comparative Study of Turbulence Models Performance for Turbulent Flow in a Planar Asymmetric Diffuser*, Proceedings of World Academy of Science, Engineering and Technology, vol. 53, pp. 769-780, 2009.

74. **Tieszen, S., Ooi, A., Durbin, P.A. and Behnia, M.** *Modeling of Natural Convection Heat*, Proceedings of the Summer Program, Center for Turbulence Research, NASA Ames/Stanford University, pp. 287-302, 1998.

75. **Choi, S.-K., Kim, E.-K. and Kim, S.-O.** *Computation of Turbulent Natural Convection in a Rectangular Cavity with the k-ε-$\overline{v^2}$-f Model*, Numerical Heat Transfer, Part B: Fundementals, vol. 45, pp. 159-179, 2004.

76. **Spall, R.E., Richards, A. and McEligot, D.M.** *An Assessment of k-ω and $\overline{v^2}$-f Turbulence Models for Strongly Heated Internal Gas Flows*, Numerical Heat Transfer, Part A: Applications, vol. 46, pp. 831-849, 2004.

77. **Simirnov, P.E.** *Testing of the $\overline{v^2}$-f Model of Turbulence in Calculating the Flow and Heat Transfer in an Abruptly Expanding Duct*, Journal of Engineering Physics and Thermophysics, vol. 79, pp. 666-672, 2006.

78. **Kalitzin, G.** *An Implementation of the $\overline{v^2}$-f Model with Application to Transonic Flows*, Annual Research Briefs, Center for Turbulence Research, NASA Ames/Stanford University, pp. 171-184, 1998.

79. **Kalitzin, G.** *Application of the $\overline{v^2}$-f Model to Aerospace Configurations*, Annual Research Briefs, Center for Turbulence Research, NASA Ames/Stanford University, pp. 289-300, 1999.

80. **Kalitzin, G.** *Towards a Robust and Efficient $\overline{v^2}$-f Implementation with Application to Transsonic Bump Flow*, Annual Research Briefs, Center for Turbulence Research, NASA Ames/Stanford University, pp. 291-299, 2000.

81. **Cokljat, D., Kim, S.E., Iaccarino, G. and Durbin, P.A.** *A Comparative Assessment of the V2F Model for Recirculating Flows*, AIAA 2003-765, 2003.

82. **Zhang, Z., Zhai, J.Z. and Chen, Q.** *Evaluation of Various CFD Models in Predicting Room Airflow and Turbulence*, Proceedings of Roomvent, 10th International Conference on Air Distributions in Rooms, 2007.

83. *ANSYS FLUENT 13.0 User's Guide*, ANSYS Inc., 2010.

84. **Fransen, R., Gourdain, N. and Gicquel, L.Y.M.** *Steady and Unsteady Modeling for Heat Transfer Predictions of High Pressure Turbine Blade Internal Cooling*, ASME Paper No. GT2012-69482, 20012.

85. **Vass, P.** *Large Eddy Simulation of a Ribbed Duct Flow with FLUENT: Effect of Rib Inclination*, VKI Diploma Course Report, 2005.

86. **Siddique, W., Shevchuk., I.V., El-Gabry, L.A. and Fransson, T.H.** *Validation and Analysis of Numerical Results for a Two-Pass Trapezoidal Channel with Different Cooling Configurations of Trailing Edge*, ASME Paper No. GT2011-46266, 2011.

87. **Kadoya, K., Matsunaga, N. and Nagashima, A.** *Viscosity and Thermal Conductivity of Dry Air in the Gaseous Phase*, Journal of Physical and Chemical Reference Data, vol. 14, pp. 947-970, 1985.

88. **Stephan, K. and Laesecke, A.** *The Thermal Conductivity of Fluid Air*, Journal of Physical and Chemical Reference Data, vol. 14, pp. 227-234, 1985.

89. **Park, Y., and Sontag, R.E.** *Thermodynamic Properties of Ideal Gas Air*, International Journal of Energy Research, vol. 20, pp. 771-785, 1996.

90. **Goldsmith, A., Waterman, T.E. and Hirschhorn, H.J.** *Handbook of Thermophysical Properties of Solid Materials, Revised Edition, Volume II: Alloys*, The Macmillan Company, New York, 1961.